Structural characterization of II-VI and III-V compound semiconductor heterostructures and superlattices

by

Lu Ouyang

A Dissertation Presented in Partial Fulfillment
of the Requirements for the Degree
Doctor of Philosophy

Approved April 2012 by the
Graduate Supervisory Committee:

David Smith, Chair
Ralph Chamberlin
Martha McCartney
Jose Menendez
Fernando Ponce

ARIZONA STATE UNIVERSITY

May 2012

ABSTRACT

The research described in this dissertation has involved the use of transmission electron microcopy (TEM) to characterize the structural properties of II-VI and III-V compound semiconductor heterostructures and superlattices.

The microstructure of thick ZnTe epilayers (~2.4 μm) grown by molecular beam epitaxy (MBE) under virtually identical conditions on GaSb, InAs, InP and GaAs (100) substrates were compared using TEM. High-resolution electron micrographs revealed a highly coherent interface for the ZnTe/GaSb sample, and showed extensive areas with well-separated interfacial misfit dislocations for the ZnTe/InAs sample. Lomer edge dislocations and 60^{o} dislocations were commonly observed at the interfaces of the ZnTe/InP and ZnTe/GaAs samples. The amount of residual strain at the interfaces was estimated to be 0.01% for the ZnTe/InP sample and -0.09% for the ZnTe/GaAs sample. Strong PL spectra for all ZnTe samples were observed from 80 to 300 K.

High quality GaSb grown by MBE on ZnTe/GaSb (001) virtual substrates with a temperature ramp at the beginning of the GaSb growth has been demonstrated. High-resolution X-ray diffraction (XRD) showed clear Pendellösung thickness fringes from both GaSb and ZnTe epilayers. Cross-section TEM images showed excellent crystallinity and smooth morphology for both ZnTe/GaSb and GaSb/ZnTe interfaces. Plan-view TEM image revealed the presence of Lomer dislocations at the interfaces and threading dislocations in the top GaSb layer. The defect density was estimated to be ~1 $x10^{7}/cm^{2}$. The PL

spectra showed improved optical properties when using the GaSb transition layer grown on ZnTe with a temperature ramp.

The structural properties of strain-balanced InAs/$InAs_{1-x}Sb_x$ SLs grown on GaSb (001) substrates by metalorganic chemical vapor deposition (MOCVD) and MBE, have been studied using XRD and TEM. Excellent structural quality of the InAs/$InAs_{1-x}Sb_x$ SLs grown by MOCVD has been demonstrated. Well-defined ordered–alloy structures within individual $InAs_{1-x}Sb_x$ layers were observed for samples grown by modulated MBE. However, the ordering disappeared when defects propagating through the SL layers appeared during growth. For samples grown by conventional MBE, high-resolution images revealed that interfaces for $InAs_{1-x}Sb_x$ grown on InAs layers were sharper than for InAs grown on $InAs_{1-x}Sb_x$ layers, most likely due to a Sb surfactant segregation effect.

To

My parents and my husband

ACKNOWLEDGMENTS

First of all, I would like to express my deepest gratitude to my advisor, Regents' Professor David J. Smith, for his continued support and guidance throughout my Ph.D. study. His enthusiasm to work and patience with students has greatly impressed me. His expertise in electron microscopy has helped me go through tough times and prepared me for future challenges. His technical and editorial advice was essential to the completion of this dissertation. I am also deeply grateful to Professor Martha R. McCartney for her support and encouragement. It has been a great honor for me to study in their group.

I would like to thank Professors Ralph Chamberlin, Jose Menendez, and Fernando Ponce for serving on my dissertation committee. I am grateful for the use of facilities in the John M. Cowley Center for High Resolution Electron Microscopy, and I thank Karl Weiss and Dr. Zhenquan Liu for their technical support and assistance throughout my research.

I would like to extend my deep appreciation to Prof. Yong-Hang Zhang and colleagues, especially Jin Fan and Elizabeth H. Steenbergen, at Arizona State University, Prof. Jacek Furdyna and Dr. Xinyu Liu at Notre Dame University, Prof. R. D. Dupuis and colleagues at Georgia Institute of Technology, Prof. and Prof. Diana Huffaker and colleagues at University of California, Los Angeles, and Dr. Amy W. K. Liu at IQE, Inc., for their collaboration and providing the samples used for investigation in this dissertation.

Particular thanks to our research group members for their help during my stay. I want to thank Dr. Luying Li as the best office-mate; Dr. Lin Zhou for the

training on electron microscopy and sample preparation; Allison Boley for her help on sample preparation by FIB; and Dr. Suk Chung, Dr. David Cullen, Dr. Kai He and Dr. Wenfeng Zhao for their discussion, assistance and friendship. My best wishes to Michael, Jae-Jin, Dinghao, Zhaofeng, Desai, Allison, Xiaomeng, Jing and Ajit for success in their degree programs.

Many friends have helped me throughout these years. Their support and encouragement helped me overcome setbacks and stay sane during my graduate study. I greatly value their friendship and I deeply appreciate their belief in me.

Last, but not least, I would like to thank my husband Ziyue for his understanding, trust and confidence in me during the past few years; and my parents for their unconditional love and support throughout my life. I would not have completed my Ph.D. study at Arizona State University without their encouragement.

TABLE OF CONTENTS

Page

LIST OF TABLES x

LIST OF FIGURES xi

CHAPTER

1 INTRODUCTION 1

1.1 Introduction to semiconductors 1

1.2 Semiconductor heterostructures 4

1.2.1 Introduction to semiconductor heterostructures 4

1.2.2 Lattice mismatch in semiconductor heterostructures 6

1.2.3 Photovoltaic solar cell applications 8

1.3 Semiconductor superlattices 12

1.3.1 Classification of semiconductor superlattices 12

1.3.2 T2SL-based infrared detectors 16

1.3.3 Antimonide T2SLs for LWIR detectors 21

1.4 Outline of dissertation 23

References 25

2 EXPERIMENTAL DETAILS 29

2.1 Material growth 29

2.1.1 MOCVD growth of InAs/$InAs_{1-x}Sb_x$ type-II superlattices 29

2.1.2 MBE growth 30

2.1.3 MBE growth of InAs/$InAs_{1-x}Sb_x$ T2SLs 33

CHAPTER Page

2.1.4 MBE growth of ZnTe and GaSb materials 34

2.2 X-ray diffraction 35

2.3 Photoluminescence 35

2.4 Transmission Electron Microscopy 37

2.4.1 High resolution electron microscopy 37

2.4.2 Scanning transmission electron microscopy 38

2.5 TEM sample preparation 41

2.5.1 Cross-sectional sample preparation 41

2.5.2 Plan-view sample preparation 41

2.5.3 Focused ion beam 42

References 44

3 MICROSTRUCTURAL CHARACTERIZATION OF THICK ZnTe EPILAYERS GROWN ON LATTICE-MATCHED AND LATTICE–MISMATCHED III-V SUBSTRATES 46

3.1 Introduction 46

3.2 Experimental details 49

3.3 Results and discussion 50

3.3.1 Microstructural characterization 51

3.3.2 Distribution of interfacial misfit dislocations 58

3.3.3 PL measurements 65

3.4 Conclusions 67

References 68

CHAPTER Page

4 STRUCTURAL CHARACTERIZATION OF GaSb EPILAYERS GROWN ON ZnTe VIRTUAL SUBSTRATES WITH A TEMPERATURE RAMP DURING GROWTH 70

4.1 Introduction 70

4.2 Experimental details 72

4.3 Results and discussion 74

4.3.1 XRD measurements 74

4.3.2 TEM characterization 76

4.3.3 PL measurements 82

4.4 Summary 84

References 86

5 STRUCTURAL CHARACTERIZATION OF InAs/$InAs_{1-x}Sb_x$ TYPE-II SUPERLATTICES 87

5.1 Introduction 87

5.2 Experimental details 89

5.3 Results and discussion 92

5.3.1 Characterization of MOCVD-grown samples 92

5.3.2 Characterization of MBE-grown samples 96

5.4 Summary 104

References 107

6 SUMMARY AND FUTURE WORK 109

6.1 Summary 109

CHAPTER Page

6.2 Future work 111

6.2.1 Minimization of ion-milling damage 111

6.2.2 Atomic arrangements around the core of dislocations 111

6.2.3 Interfacial intermixing in InAs/InAsSb T2SLs..... 112

References 115

APPENDIX

A REFERENCES 116

B TABLE OF ACRONYM 123

LIST OF TABLES

Table		Page
1.1	List of some common semiconductors	2
1.2	Lattice mismatch for some semiconductor heterostructures at room temperature	8
1.3	List of some advantages and disadvantages of photovoltaics	10
3.1	Growth information for ZnTe on various III-V substrates	49
3.2	Relevant substrate parameters for growth of ZnTe.	51
4.1	Summary of growth parameters for the growth of GaSb epilayer on ZnTe virtual substrates	73
5.1	Summary of InAs/ $InAs_{1-x}Sb_x$ SL samples grown by MOCVD	92
5.2	Summary of InAs/ $InAs_{1-x}Sb_x$ SL samples grown by MBE	97

LIST OF FIGURES

Figure Page

1.1 Schematic of energy bands for an intrinsic semiconductor. 3

1.2 The energy band diagram of a heterostructure constructed from two semiconductor materials with bandgap E_g^1 and E_g^2.. 5

1.3 Schematic illustration of a simple semiconductor photovoltaic device 9

1.4 Electron energy in the valence and conduction bands of semiconductors as a function of distance in the direction of the SL for: (a) alternation of donor and acceptor impurities; and (b) periodic variation of alloy composition. 13

1.5 Discontinuities of the band-edge energies at different types of heterointerfaces: band offset (left), band bending and carrier confinement (middle), and SL alignment (right). 15

1.6 Bandgaps, cutoffs wavelength and lattice constants of some III-V, II-VI and IV semiconductor materials at room temperature 18

1.7 (a) Band structure of unstrained direct-gap tetrahedral semiconductor, where the LH and HH bands are degenerate at the Brillouin zone center Γ, and the lowest conduction band (CB) is separated by the band-gap energy (Eg) from the valence bands; (b) the shifted band structure under biaxial tension; and (c) under biaxial compression. 19

Figure Page

1.8 Schematic illustration of the effects of strain in a strained-layer T2SL. The full lines represent the quantum well potentials and barriers, while the dashed lines represent the resulting energy levels and the arrows represent band-to-band transitions. 20

2.1 Schematic illustration of a basic MBE growth chamber 31

2.2 Schematic illustration of In, As and Sb shutter sequences during the modulated MBE growth of InAsSb alloy layers and InAs layers. 33

2.3 The mechanism of PL of a semiconductor excited by photons with energy no less than the bandgap: (I) photon absorption; II) CB-to-VB radiative transition; (III) excitonic PL process; and (IV) non-radiative transition. 37

2.4 Schematic diagram showing the essential components of the STEM. 40

2.5 (a) Scanning electron micrograph showing the Pt protection layer; (b) XTEM image of the InAs/InAsSb SL sample prepared using FIB technique 43

3.1 Lattice constants and bandgaps for some III-V, II-VI and IV semiconductor materials at room temperature 48

3.2 (a) Cross-sectional electron micrograph of ZnTe/GaSb sample showing highly-separated misfit dislocations at the interface; (b)

Figure Page

HREM image establishing highly coherent nature of the ZnTe/GaSb interface (arrowed). 52

3.3 (a) Low magnification image of ZnTe/InAs sample showing rapid falloff in defect density upon moving away from the interface region; (b) HREM image showing enlarged view of the ZnTe/InAs interface (arrowed) region without any defects 53

3.4 (a) Low-magnification diffraction contrast image of ZnTe/InP heterostructure showing typical cross-section of the entire ZnTe epilayer; (b) SAED pattern from interface region of the ZnTe/InP sample showing well-defined and distinct ZnTe and InP diffraction patterns 54

3.5 (a) HREM image in {011}-type projection showing the ZnTe/InP interface; (b) (c) Enlarged views of the interface, with Burgers circuit analysis identifying 60^{o} partial dislocation and Lomer edge dislocation. ***S*** and ***F*** stand for ***Start*** and ***Finish***, respectively..... 55

3.6 (a) Low magnification image showing the entire ZnTe epilayer grown on GaAs (001) substrate; (b) SAED pattern taken from ZnTe/GaAs interface region 56

3.7 (a) HREM image showing the region of ZnTe/GaAs interface with periodic Lomer edge dislocations. (b) Enlarged view of the interface region, with Burgers circuit analysis identifying Lomer edge dislocation 57

Figure Page

3.8 (a) Part of the digitized lattice image of the ZnTe/GaAs interface, with a Lomer dislocation at left and a 60º dislocation at right (both arrowed); (b) FFT pattern of image (a); (c) Inverse FFT image obtained by selecting {111} diffraction spots marked by circles; (d) Inverse FFT image obtained by selecting {111} diffraction spots marked by squares 59

3.9 (a) (b) Inverse FFT images for ZnTe/InP sample showing specific {111} crystalline planes; (c) Corresponding high-resolution image identifying dislocation type, where ***LO*** and ***60^o*** stand for Lomer edge dislocation and 60^o dislocation, respectively..... 61

3.10 (a) (b) Inverse FFT images for ZnTe/GaAs sample showing specific {111} crystalline planes; (c) Corresponding high-resolution image identifying dislocation type, where ***LO*** and ***60^o*** stand for Lomer edge dislocation and 60^o dislocation, respectively... 62

3.11 Distribution of separations of dislocations with equal edge components for: (a) ZnTe/InP sample; and (b) ZnTe/GaAs sample.. 64

3.12 (a) PL spectra of ZnTe epilayer grown on various III-V substrates; (b) Temperature-dependent PL spectra of ZnTe/GaAs sample. 66

4.1 Schematic illustration of the epitaxial layer structure for: (a) Sample A; (b) Samples B and C; and (c) Sample D..... 73

Figure Page

4.2 XRD ω-2θ curves measured in the vicinity of the (004) diffraction peak of GaSb substrate for: (a) Sample A and (b) Sample B 75

4.3 Low-magnification XTEM images showing interfaces for: (a) Sample A; (b) Sample B; and (c) Sample C 77

4.4 (a) Plan-view TEM image of Sample C showing the presence of threading defects (circled) in the top GaSb layer; (b) Enlarged view of the threading defects 78

4.5 Plan-view TEM image of Sample C showing the presence of well-separated Lomer edge dislocations at the ZnTe/GaSb interface 79

4.6 (a) Cross-section electron micrograph showing the interfaces of Sample D; (b) Enlarged view showing misfit dislocations (arrowed) present at the GaSb/ZnTe interface 81

4.7 PL spectra measured at 13 K for: (a) Sample A; (b) Sample B; and (c) Sample C. 83

5.1 Schematic illustration of the sample structures for: (a) MOCVD grown SLs; (b) modulated MBE grown SLs; and (c) conventional MBE grown SLs 90

5.2 High-resolution (004) XRD patterns and simulations (offset below each measurement) for Samples A and B 93

5.3 Cross-sectional electron micrograph of Sample A demonstrating the excellent crytallinity of the In InAs/$InAs_{0.78}Sb_{0.22}$ SL 94

Figure Page

5.4 Low magnification TEM images showing the whole InAs/InAsSb SL structure with a large density of defects for: (a) Sample B; and (b) Sample C 95

5.5 High-resolution XRD (004) ω-2θ profiles and corresponding simulations (offset below each measurement) for Samples D and E..... 98

5.6 (a) Cross-sectional electron micrograph showing entire SL structure of Sample D, confirming very low defect density; (b) Higher-magnification image clearly showing well-ordered In(As)Sb/InAs(Sb) MQW structure within the individual $InAs_{1-x}Sb_x$ layers of Sample D..... 99

5.7 Z-contrast images for Sample D acquired using HAADF-STEM . 101

5.8 (a) Low magnification TEM image of Sample E showing typical defective region; (b) Higher-magnification image showing the presence of the In(As)Sb/InAs(Sb) MQW structure apparently only within the first $InAs_{1-x}Sb_x$ layer. 101

5.9 Low magnification image of Sample F showing the entire structure..... 103

5.10 Cross-sectional electron micrograph of Sample G demonstrating the well-defined and defect-free InAs/$InAs_{0.71}Sb_{0.29}$ SL region 103

5.11 (a) High-resolution lattice image showing individual InAs and $InAs_{0.71}Sb_{0.29}$ layers for sample D; (b) Filtered image revealing

different interface abruptness between layers, which is attributed to segregation of the Sb surfactant during growth; (c) Line profile average across both InAs-on-InAsSb and InAsSb-on-InAs interfaces, as indicated by blue dashed area boxed above, showing the differences in interface abruptness 106

6.1 (a) HAADF image of an isolated AlAs-on-GaAs interface at a specimen thickness of ~50 nm; (b) Example of a column ratio of the AlAs/GaAs SL at a pecimen thickness of ~30 nm; (c)(d) Column ratio profiles averaged over the entire column ratio map in (b). 114

Chapter 1

INTRODUCTION

1.1 Introduction to semiconductors

Semiconductors are a class of materials with electrical conductivity that is intermediate in magnitude between that of conductors and insulators. Their conductivity values are typically in the range of 10^{3} to 10^{-8} siemens per centimeter, and are strongly dependent on temperature. There are essentially two types of semiconductors: elemental semiconductors, which are composed of a single species of group-IV element, and compound semiconductors, many of which are formed from combinations of group-III and group-V elements, but also from combinations of group-II and group-VI elements and other elements. Table 1.1 lists a few of the more common elemental and binary semiconductors. Three-element, or ternary, compound semiconductors, such as $Al_xGa_{1-x}As$, and even more complex compound semiconductors, can also be formed, providing more options and flexibility in electronic engineering.[1,2]

A pure semiconductor is often called an intrinsic semiconductor, with an energy-band structure shown schematically in Fig. 1.1. The conductivity at 0 K is effectively zero since all states in the valence band (VB) are nearly filled with electrons and all states in the conduction band (CB) are vacant. However, electrons are easily excited thermally from the VB to the empty CB as temperature is increased, leaving holes in the VB. Both electrons in the CB and holes in the VB can contribute to the electrical conductivity. The ease with which

electrons can be excited from the VB to the CB depends on the band-gap energy, as shown in Fig. 1.1. Each semiconductor has a characteristic energy band structure and thus different band gaps. Table 1.1 lists the band gaps of some common elemental and binary semiconductors at room temperature. The band gaps of ternary, or more complex, compound semiconductors can be changed by controlling the composition, which is usually called band-gap engineering. Moreover, the electronic properties, especially the conductivity, of a semiconductor can be dramatically changed but in a controlled manner by introducing very small quantities of other elements, usually called dopants, to the material, thereby changing an intrinsic semiconductor into an extrinsic semiconductor. [3]

Table 1.1 List of some common semiconductors.

Elemental semiconductors		**Band gap** (eV)	**Compound semiconductors**		**Band gap** (eV)
Si	Silicon	1.11	**InP**	Indium phosphide	1.35
Ge	Germanium	0.67	**GaAs**	Gallium arsenide	1.43
Sn	Tin	-	**CdTe**	Cadmium telluride	1.49
			AlAs	Aluminum arsenide	2.16
			ZnTe	Zinc telluride	2.26
			SiC	Silicon carbide	2.86
			GaN	Gallium nitride	3.40

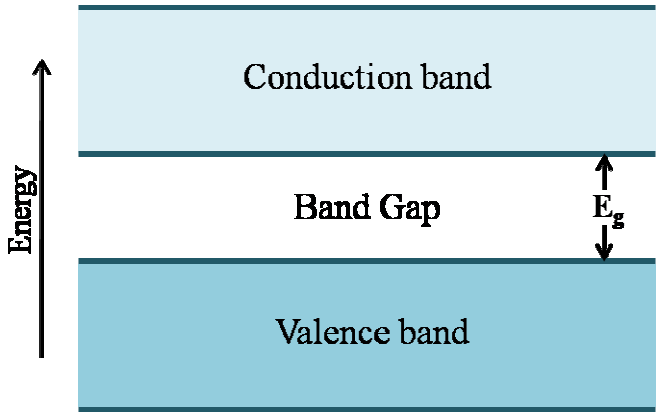

Fig. 1.1. Schematic of energy bands for an intrinsic semiconductor.

The development of semiconductor materials has had a long history dating back to the 19th Century. A big breakthrough came in 1947 when the very first transistor was fabricated using polycrystalline germanium by William Shockley, John Bardeen, and Walter Brattain at Bell Telephone Laboratories.[4] Transistor properties were soon also demonstrated in silicon, and were thereafter improved greatly through the use of either single crystal germanium or silicon. The first integrated circuit (IC) was fabricated using germanium by Jack Kilby at Texas Instruments in 1958,[5] and the first silicon IC chip made later by Robert Noyce at Fairchild Camera solved several practical problems of Kilby's circuits.[6] The development of transistors and ICs has lead to the remarkable range of capabilities of semiconductors, which have become the foundation of modern electronic devices, such as solar cells, light-emitting-diodes, digital and analog ICs. Silicon has been studied most extensively, and is by far the most common semiconductor used for commercial electronic products. Gallium arsenide, which

exhibits superior electron transport properties and good optical properties, has also been intensively investigated, and it has been employed in a significant number of electronic device applications in recent years.[2]

1.2 Semiconductor heterostructures

1.2.1 Introduction to semiconductor heterostructures

Junctions between two dissimilar materials are usually referred to as heterojunctions in contrast to homojunctions where only one material is involved. Semiconductor heterostructures are composed of two or more semiconductor materials which are likely to have different band gaps, electron affinities, and indexes of refraction. The properties of devices based on semiconductor heterostructures strongly depend on the characteristics of the interface, where the mismatch in band gaps has to be accommodated by discontinuities of the band edges. The CB and VB discontinuities, ΔE_C and ΔE_V, are the most important factors in determining the behavior and performance of heterostructure devices, as illustrated in Fig. 1.2. These discontinuities may form barriers for charge carriers crossing the interface and thus influence the operation of heterostructure devices. Another characteristic feature is the presence of interface states, such as defects, which can also influence device behavior by acting as charge traps or recombination centers. Finally, the position of the Fermi level, E_F, determines the barrier height on the two sides of the interface. V_D^1 and V_D^2, illustrated in Fig. 1.2, represent the band bending that is present on the two sides of the junction, which keeps the Fermi level constant everywhere in the system.[3,5]

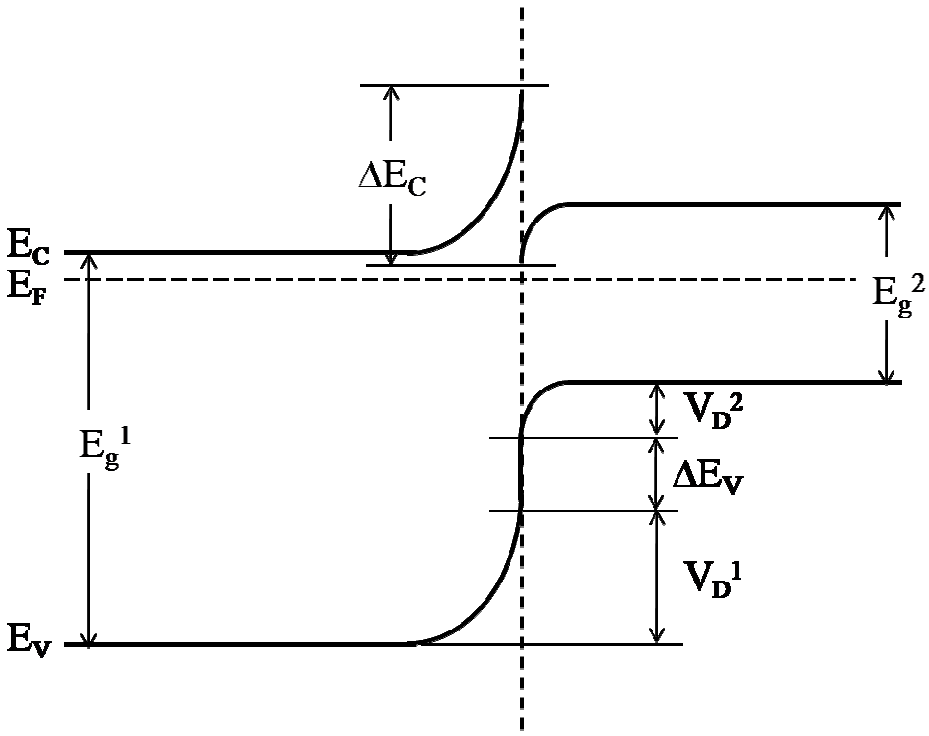

Fig. 1.2. The energy band diagram of a heterostructure constructed from two semiconductor materials with band gap E_g^1 and E_g^2. E_C and E_V are the CB and VB edges, and E_F is the Fermi level.

Theoretical analysis of the current-voltage characteristics of heterojunctions was initially carried out by Gubarov in the early 1950s.[9,10] Shockley and Kroemer pointed out potential applications of heterojunctions and the advantages of heterojunction devices over homojunction.[11,12] In 1962, Anderson proposed an idealized model for heterojunctions,[13] which explained the basic parameters of the junction in terms of the two component materials, although ignoring the quantum effect, defect states and other perturbations that may result in imperfect matches of the materials. According to Anderson, the CB and VB discontinuities, ΔE_C and ΔE_V, can be formulated by the following:

$$\Delta E_C + \Delta E_V = E_g^1 - E_g^2$$

$$\Delta E_C = \chi^2 - \chi^1$$

where χ^1 and χ^2 are the electron affinities of the two semiconductors.

The next big step was taken in 1963, when lasers based on double heterostructures were proposed to dramatically improve the operation of conventional semiconductor lasers.[14,15] In a double heterostructure, constructed from a pair of heterojunctions, non-equilibrium charge carriers are confined in the narrow-band-gap semiconductor, which lies between two wide-band-gap semiconductors. The first ideal heterostructures of AlGaAs, which is a lattice-compatible system for GaAs, were fabricated by the liquid-phase-epitaxy method in 1967.[16,17] With further investigation of semiconductor heterostructures, the concepts of quantum wells, quantum dots, quantum wires and superlattices (SLs) were proposed, and additional important devices were fabricated. Semiconductor heterostructures are nowadays key elements in the semiconductor industry, and they determine the development of novel types of semiconductor devices.[18]

1.2.2 Lattice mismatch in semiconductor heterostructures

In a heterostructure that is composed of two semiconductors featuring different lattice spacings, there is a lattice mismatch, which can be represented by the simple expression:

$$f = (a_2 - a_1) / a_1 ,$$

where a_1 and a_2 are the strain-free lattice constants of the two materials.

The lattice mismatch between the two semiconductors can usually be accommodated either by elastic strain within the layers or by generating an array of misfit dislocations at the interface.[19] During epitaxial growth, the deposited material is pseudomorphic with the other material when the thickness is less than the so-called critical thickness.[20] The deposited layers initially have biaxial lateral strain with a magnitude that brings the epitaxial layer structure into perfect lattice match with the crystal structure of the other material. As the layer thickness grows to more than some critical value, the strain will start to be released by the formation of misfit dislocations at the interface. Thus, the lattice mismatch effectively prevents the growth of defect-free heterostructures unless the layer thickness is less than this value. The concept of critical thickness, which depends on the lattice mismatch between the two materials, was first proposed by Frank and van der Merwe in 1949.[20] When the lattice mismatch is sufficiently small, the critical thickness could effectively become infinite, whereas large lattice mismatch would result in the generation of large quantities of misfit dislocations. In practice, the amount of lattice mismatch might be anticipated to impact the nature of the interfacial misfit dislocations. Moreover, it has been reported that experimental measurements of critical thickness for lattice-mismatched II-VI semiconductors tend to be larger than calculated values.[21]

Lattice-matched heterostrucures have attracted much attention, since interfacial defects strongly affect the performance of devices based on semiconductor heterostructures. These defects represent effective scattering and recombination centers for the charge carriers. Table 1.2 lists the lattice mismatch

Table 1.2. Lattice mismatch for some semiconductor heterostructures at room temperature.

A_1B_1/A_2B_2	a_1 (Å)	a_2 (Å)	f
ZnTe/InP	6.1037	5.8686	3.85%
ZnTe/GaSb	6.1037	6.0959	0.13%
CdSe/InAs	6.0500	6.0584	-0.14%
CdTe/InSb	6.4820	6.4794	0.04%
AlSb/GaAs	6.1355	5.6533	7.86%
AlAs/InP	5.6605	5.8686	-3.68%
ZnS/GaP	5.4200	5.4512	-0.58%

for some heterostuctures based on the combinations of binary semiconductors. For heterostrucures consisting of one binary semiconductor and one ternary semiconductor, the lattice mismatch problem may be more easily solved by controlling the composition. For example, $In_{0.53}Ga_{0.47}As$ is lattice-matched to InP, and $In_{0.49}Ga_{0.51}P$ is lattice-matched to GaAs.[22] For heterostructures of two ternary semiconductors, lattice matching can be achieved within a broad range of compositions.

1.2.3 Photovoltaic solar cell applications

Photovoltaics is the technology of generating direct current electric power by converting light energy into a flow of electrons. A solar cell is simply an individual photovoltaic element that has been designed and constructed to absorb and convert solar energy into electrical energy. Semiconductors have the

capability to absorb photons with energy greater than the semiconductor band gap and then excite electrons from the VB to the CB. In a photovoltaic device, there is usually some built-in spatial asymmetry which can drive the excited electrons within the conduction band and holes in the valence band through an external circuit to do electrical work and thus generate electrical power, as illustrated in Fig. 1.3. In principle, the generated electric power is the number of free electrons times their potential, while the potential of the electrons is less than the band gap of the semiconductor. For example, in a semiconductor with band gap of 1 eV, an electron excited by a photon with 2 eV or higher energy will deliver energy of just

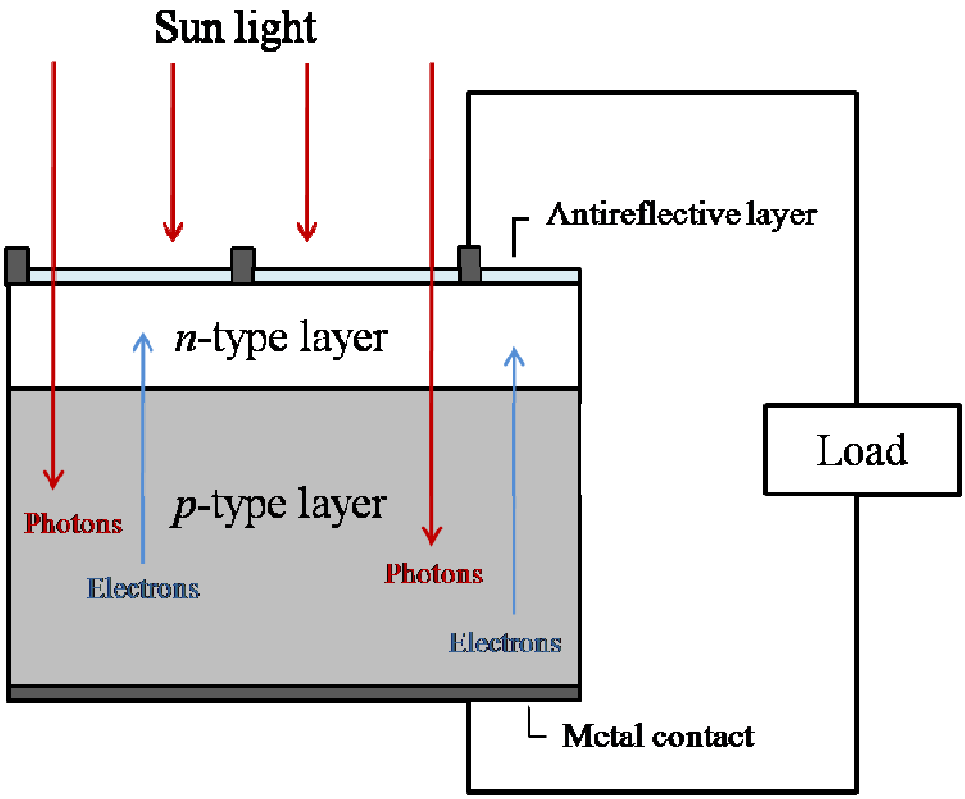

Fig. 1.3. Schematic illustration of a simple semiconductor photovoltaic device.[23]

Table 1.3. List of some advantages and disadvantages of photovoltaics.[24]

Advantages of photovoltaics	**Disadvantages of photovoltaics**
Fuel source is vast and essentially infinite	Fuel source is diffuse (sunlight is a relatively low-density energy)
No emission or radioactive fuel for disposal	
Low operating costs	High installation costs
No moving parts	
Ambient temperature operation	
High reliability in modules	Poorer reliability of auxiliary elements including storage
Modular	
Quick installation	
Daily output peak may match local demand	Lack of economical efficient energy storage
Excellent safety record	

less than 1 eV to the external world. It should be obvious that the band gap of the semiconductor determines how well the solar cell is coupled to the solar spectrum and thus the cell efficiency. The advantages and disadvantages of using photovoltaics are almost completely opposite to conventional fossil-fuel power plants, as listed in Table 1.3.

The photovoltaic effect was first reported by Bequerel in 1839, when he observed an electric current produced by the action of light on a sliver-coated platinum electrode immersed in an electrolyte.[25] The first large solar cell was

produced by Charles Fritts in 1894, with a layer of selenium between gold and another metal.[23] In early photovoltaic devices, a semi-transparent layer of metal deposited on top of the semiconductor provided both asymmetry of the electronic junction and access to the junction for incident light. In the 1950s, the development of silicon electronics followed on from the discovery of a way to manufacture *p-n* junctions in silicon. The first silicon solar cell was reported by Chapin, Fuller, and Pearson in 1954, with an energy conversion efficiency of ~ 6%.[26] Silicon solar cells were widely developed for applications in space in the 1950s and 60s. In the following years, theoretical studies of *p-n* junction photovoltaic devices indicated that higher efficiency could be achieved using III-V semiconductor heterostructures.[27] To further increase solar cell efficiency, multi-junction solar cells have been proposed, with energy conversion efficiency in excess of 30%.[28] An efficiency of 27.3% in $Ga_{0.5}In_{0.5}P$/GaAs tandem solar cell was reported in 1989,[29] and an efficiency of 43.5% at greater than 400 suns has been achieved by Solar Junction, a multi-junction cell developer, on a GaInP/GaAs/GaInNAs multi-junction cell in 2011.[30]

The major improvement of multijunction solar cells compared to single-junction solar cells is that efficiency can potentially be increased by taking advantage of a greater portion of the solar energy spectrum using semiconductors with several different band gaps. A practical multijunction design based on the monolithic integration of II-VI (MgZnCd) (SeTe) and III-V (AlGaIn)(AsSb) materials, for example, consisting of two III-V subcells (GaSb and AlGaAsSb) and two II-VI subcells (CdSeTe and ZnTe), has been proposed, with band-gap

energies spanning a broad range of the solar spectrum.[31] The II-VI (MgZnCd)(SeTe) materials can be grown lattice-matched on the so-called 6.1-Å III-V substrates, such as GaSb or InAs, with very low densities of misfit dislocations.[32] Moreover, some of the lattic-matched II-VI and III-V heterojunction interfaces, such as CdSe/ZnTe and InAs/GaSb, have type-II band alignment, which is desirable for tunnel junctions between each individual subcell of tandem structures. ZnTe is nearly lattice-matched to GaSb with only 0.13% lattice mismatch, and the thermal expansion coefficient of ZnTe is very close to that of GaSb. Thus, ZnTe is considered to be an essential constituent material in novel II-VI/III-V multijunction solar cell structures.

1.3 Semiconductor superlattices

1.3.1 Classification of semiconductor superlattices

The semiconductor superlattice (SL) concept, first presented by Esaki and Tsu in 1970,[33] defined a new group of semiconductor materials having a one-dimensional periodic arrangement of alternating thin layers (normally several nanometers in thickness). The amplitude and period of the SL potential can be varied over a range of values, which is different from that of bulk materials. Two types of SLs can be defined, based on the method used to form the SL structure. The doping SL is fabricated using a periodic variation of donor or acceptor impurities in a single semiconductor; and the compositional SL is accomplished by periodic variation of the alloy composition. Figure 1.4 shows the energy diagrams for these two types of SLs, where the solid and dashed lines represent

sinusoidal and periodic square-well potentials, respectively. The E_g are the magnitudes of the energy gap of the semiconductors, and V_1 is the amplitude of the periodic SL potential. For doping SLs, the amplitude of the periodic potential can, in principle, be chosen to be any value up to that of the energy gap, whereas this value would be limited for compositional SLs to about half of the difference

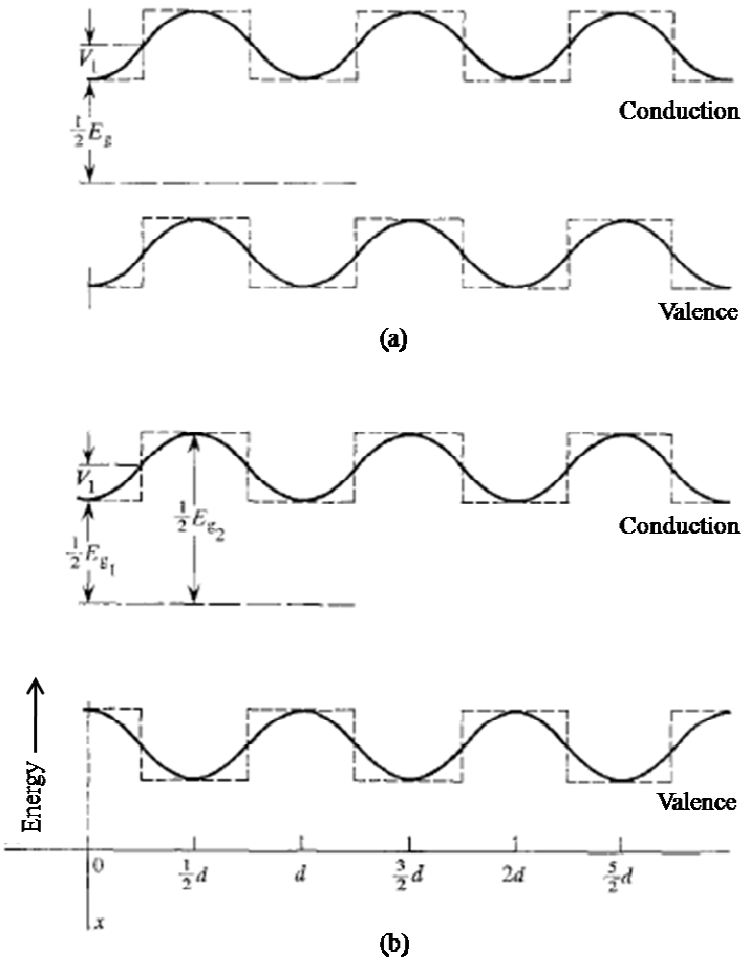

Fig. 1.4. Electron energy in the valence and conduction bands of semiconductors as a function of distance in the direction of the SL for: (a) alternation of donor and acceptor impurities; and (b) periodic variation of alloy composition.[33]

between the energy gaps of the two alternating semiconductor materials.[33] Both methods can be introduced simultaneously during the epitaxial growth of semiconductor SLs, but it is more desirable to form compositional SLs since thermal diffusion of impurities in doping SLs is hard to control during growth, and sophisticated epitaxial growth techniques have been developed to grow sufficiently thin layers with high quality heterointerfaces. The most common growth methods are molecular beam epitaxy (MBE) and metalorganic chemical vapor deposition (MOCVD), although other growth techniques, such as metalorganic MBE, low pressure MOCVD, chemical beam epitaxy, hot wall epitaxy and atomic layer epitaxy, have also been explored.

Semiconductor SL structures have been epitaxially grown using III-V, II-VI, and IV-IV compound and elemental semiconductors, as well as amorphous materials. Semiconductor heterointerfaces exhibit abrupt discontinuities in their local band structure, usually associated with gradual band bending in the neighborhood, which reflects space-charge effects. According to the band alignment, the SL structures can be classified into three different types, called type-I, type-II (T2) and type-III, as illustrated in Fig. 1.5. For type-I SLs, such as the GaAs/GaAlAs and GaSb/AlSb systems, the bottom of the conduction subband and the top of the valence subband are formed in the same semiconductor layer, with an energy gap difference $\Delta E_g = \Delta E_c + \Delta E_v$. Thus, electrons and holes are confined in the smaller-band-gap semiconductor material. Among T2SLs, such as the InP/AlInAs and InAs/GaSb systems, the bottom of the conduction subband is formed in one layer and the top of the valence subband is formed in the other

layer, with $\Delta E_g = |\Delta E_c - \Delta E_v|$. Thus, electrons and holes are confined in different semiconductors. In particular, there is a T2 misaligned SL structure, different from the T2 staggered structure, where the top of valence subband is located above the bottom of the conduction subband, as shown in Fig. 1.5.[34] The all-binary GaAs/AlAs SLs are also interesting, since both type-I and T2 staggered structures can be achieved in the same set of materials by changing the SL layer thickness. Type-III SLs, such as HgTe/CdTe SLs, involve semimetal materials.

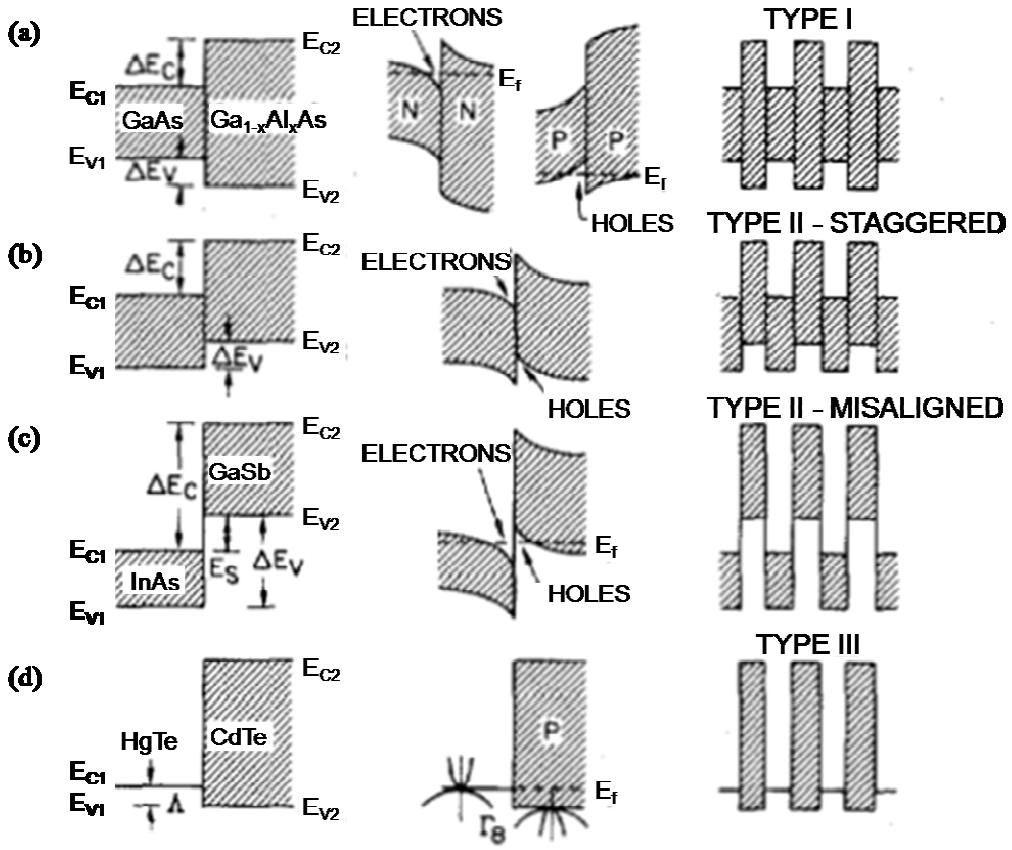

Fig. 1.5. Discontinuities of the band-edge energies at different types of heterointerfaces: band offset (left), band bending and carrier confinement (middle), and SL alignment (right).[34]

Although the bottom of the conduction subband and the top of the valence subband are formed in the same semiconductor layer, which is similar to type-I SLs, the band gap of the type-III SL can be continuously adjusted from a semiconductor to a zero-band-gap material or even to a semimetal with negative band gap.[35]

1.3.2 T2SL-based infrared detectors

The theory of electronic subband structure of T2SLs was first presented by Sai-Halasz *et al.* in 1977,[36] with an experimental demonstration for InAs/GaSb SLs by Sakaki *et al.* in 1978.[37] It turns out that this type of SL structure has a novel and important feature: the band gap of the SL can be smaller than that of either semiconductor bulk material forming the T2SL. Moreover, the electron-hole wave-function overlap is small in T2SLs and decreases exponentially with increasing layer thickness of the semiconductors involved. Thus, the band gap of T2SLs depends on the length of the periodic variation of the different semiconductors. In principle, interaction of these bands vanishes for large separations so that the band gap tends to zero, resulting in metallic SLs. This property forms the basis for the utilization of T2SLs for infrared (IR) photodetectors.

The range of electromagnetic energy that covers the wavelength region from ~1 μm to 1000 μm is called infrared (IR) radiation, and is usually divided into near-IR (0.75 ~ 1.4 μm), short-wavelength IR (1.4 ~ 3 μm), mid-wavelength IR (3 ~ 8 μm), long-wavelength (LW) IR (8 ~ 15 μm) and very-long-wavelength

IR (15 ~ 1000 μm) regions. The two main types of IR detectors are thermal and photonic detectors. For thermal devices, the absorption of incident IR radiation raises the temperature of the device, causing some temperature-dependent phenomena, such as changes in electrical conductivity that bolometers and microbolometers are based on. Thermocouples and thermopiles use the thermoelectric effect; while Golay cell detectors rely on thermal expansion. For photodetectors, the absorption of IR radiation results directly in specific quantum events, such as electronic interband transitions, or photoelectric emission of electrons from the surface. Photodetectors operated in the LWIR region usually need to be cooled down to temperatures of less than 80 K to reduce thermal background noise. However, response time is faster and the sensitivity is much greater for photodetectors than for thermal detectors.

The materials used for IR photodetectors are semiconductors with relatively narrow band gaps. Figure 1.6 illustrates the band gaps, cutoff wavelengths and lattice constants of some common III-V, II-VI and IV semiconductors. Most III-V compounds shown in Fig. 1.6 radiate in the IR region, but only InSb has a cutoff wavelength approaching the LWIR region. Therefore, it is very difficult to achieve band-to-band transitions in the LWIR region from any of these III-V bulk semiconductors. The InAsSb alloy system has the longest cutoff wavelength among all conventional III-V bulk semiconductors, which is just 9 μm for $InAs_{0.39}Sb_{0.61}$ at 77K.[38] In the II-VI material system, combinations of CdTe and HgTe can span a wide range of wavelengths, allowing flexible band gap engineering throughout much of the whole IR region. However, it is both

expensive and difficult to grow Hg-based materials with precisely controlled Hg composition. Extrinsic Si has also been used as the material for IR detectors.[39] A major disadvantage of Si-doped detectors is that cooling to temperatures of ~20 K is essential for satisfactory noise performance.

In principle, III-V semiconductor SLs represent viable alternatives for IR detectors, with important advantages over HgCdTe, which has long been the dominant semiconductor material for IR photon detection technology. These advantages include: i) better control of alloy composition, resulting in more uniform material and cutoff wavelength, which are of major concerns for detector arrays; ii) stronger bonds and structural stability; iii) less expensive, closely lattice-matched substrates, such as GaSb; iv) mature III-V growth and processing

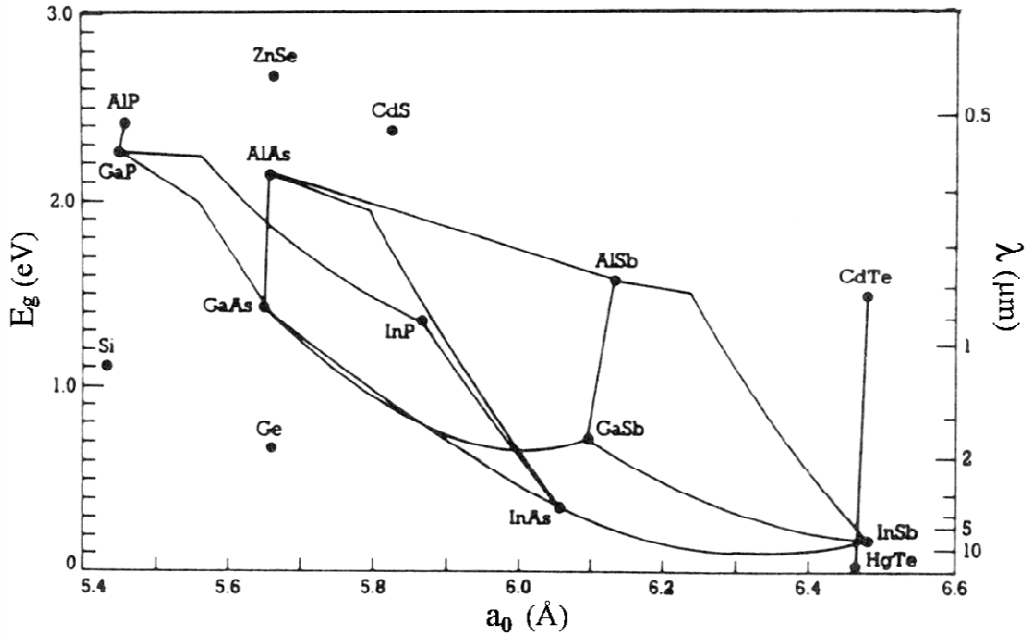

Fig. 1.6. Band gaps, cutoffs wavelength and lattice constants of some III-V, II-VI and IV semiconductor materials at room temperature.[40]

technology; v) lower band-to-band tunneling due to larger electron effective mass; vi) lower Auger recombination rates due to substantial splitting of the light- and heavy-hole bands; and vii) larger cross section for photon absorption.

In the design of III-V semiconductor SL structures for IR detector applications, the strain of heterostructures constructed from lattice-mismatched semiconductor materials is an additional factor that can affect the band alignment,[41] in addition to the SL thicknesses and the semiconductors involved. SLs consist of alternating thin layers that can allow complete elastic strain accommodation due to lattice mismatch. The SL layers with smaller bulk lattice constants are under biaxial tension, and exhibit reduction of the CB minimum energy and splitting of the light-hole (LH) and heavy-hole (HH) bands, as

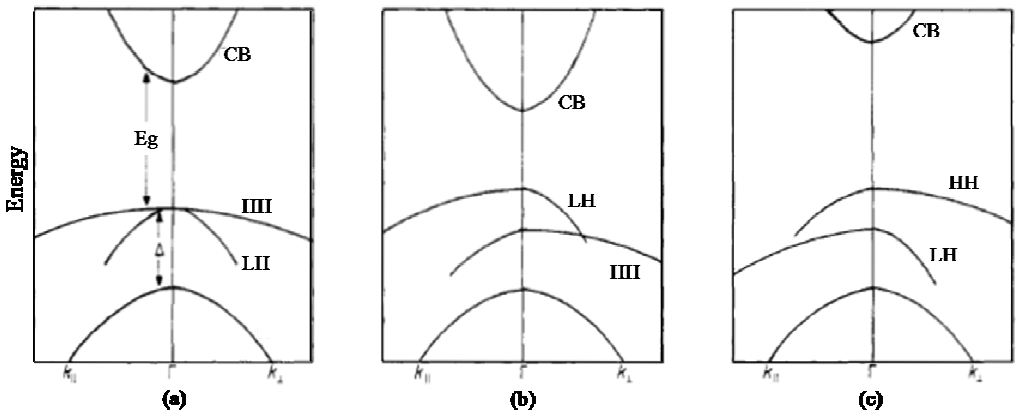

Fig. 1.7. (a) Band structure of unstrained direct-gap tetrahedral semiconductor, where the LH and HH bands are degenerate at the Brillouin zone center Γ, and the lowest conduction band (CB) is separated by the band-gap energy (Eg) from the valence bands; (b) the shifted band structure under biaxial tension; and (c) under biaxial compression.[41]

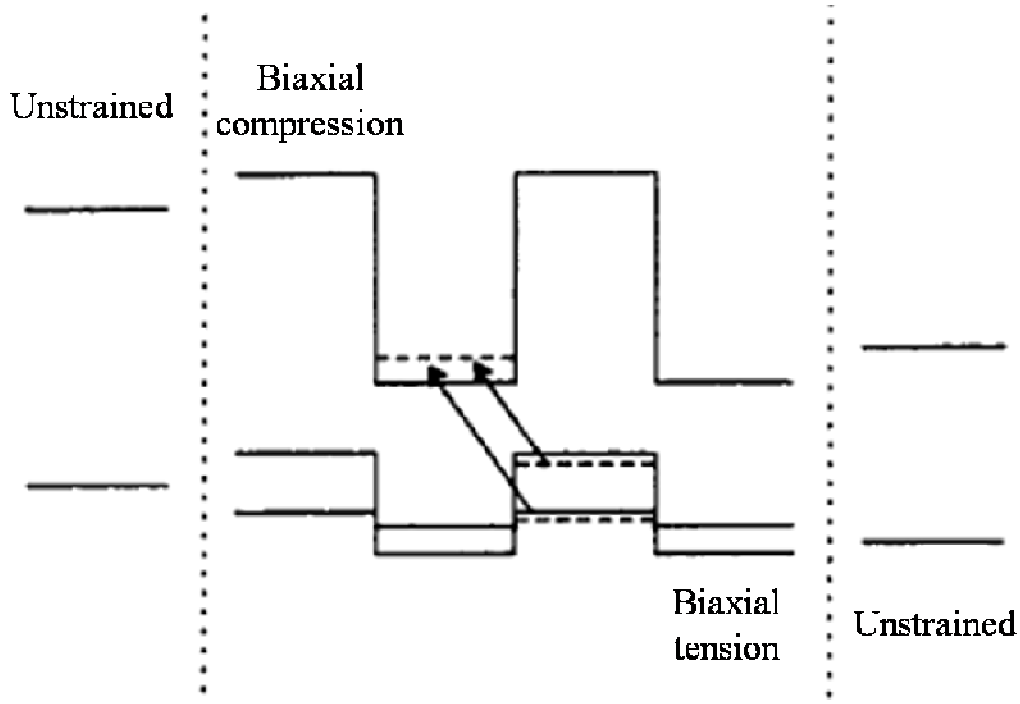

Fig. 1.8. Schematic illustration of the effects of strain in a strained-layer T2SL. The full lines represent the quantum well potentials and barriers, while the dashed lines represent the resulting energy levels and the arrows represent band-to-band transitions.[40]

illustrated in Fig. 1.7 (b). The SL layers with larger bulk lattice constants are under biaxial compression, and exhibit an increase in the CB minimum energy, and splitting of the LH and HH bands with reversed directions, as illustrated in Fig. 1.7 (c). In addition to VB splitting, strain introduces a strongly anisotropic valence band structure in both cases. The effects of strains on the band alignment of strained-layer T2SLs are illustrated in Fig. 1.8, where the band gap of the SL structure decreases with respect to the unstrained case.

1.3.3 Antimonide T2SLs for LWIR detectors

Antimonide-based T2SLs show great promise for low-cost LWIR detector applications, and have attracted much attention for investigations of structural properties.[36,37,40,42-47] The ability of the InAs/GaSb SL system to achieve small IR energy gaps was first realized when the T2SL concept was first presented.[36,37] The InAs/GaSb SLs have T2-misaligned bands, as illustrated in Fig. 1.5. (c), with the InAs CB lower than the GaSb VB. Electrons are confined within the InAs layer; whereas holes are confined within the GaSb layers. Consequently, the electron-hole wavefunction overlap, which determines the optical matrix element for IR absorption, decreases rapidly as the InAs and GaSb layer thicknesses are increased. Therefore, this system does not provide useful optical absorption coefficients with increasing layer thicknesses to reach LW cutoff wavelength, and is thus not suitable for LWIR detector applications.[40,42]

The InAs/GaInSb SL system has been proposed as an alternate III-V candidate for LWIR detectors, since it is possible to simultaneously achieve LW cutoffs and large optical absorption coefficients.[43,44] This system has similar band structure to the InAs/GaSb system, but differs in the use of strain due to small lattice mismatch between the InAs and GaInSb layers. The thin InAs and GaInSb layers are grown alternately in biaxial tension and compression, which lead to reduced band gap for the SL structure, as illustrated in Fig. 1.8. As a result, the SL layer thicknesses required to reach LW cutoff wavelength are reduced, and thus large optical absorption coefficients can be achieved at the same time. Significant success with LWIR focal plane arrays using InAs/GaInSb SLs has been

achieved.[45] The performance of InAs/GaInSb T2SLs is approaching that of HgCdTe, but the minority carrier lifetimes of InAs/GaInSb T2SLs is limited by Shockley-Read-Hall (SRH) recombination.[46] The life time remains in the tens of nanoseconds range compared to microseconds for HgCdTe. This short minority carrier lifetime is detrimental to both the device dark current and the quantum efficiency.[47]

T2SLs based on InAs/InAsSb represent an alternative to InAs/GaInSb T2SLs for IR detector applications. The InAsSb strained-layer SL system was first proposed as a novel III-V semiconductor system for potential LWIR detector applications in 1984.[38] Theoretical study showed that certain InAsSb SLs with intentional layer strain could achieve wavelengths beyond 12 µm at 77K. Photoluminescence of near 10 µm has been reported for InAs/$InAs_{0.61}Sb_{0.39}$ SL grown by MBE,[48] and 11.1 µm for InAs/ $InAs_{0.71}Sb_{0.29}$ SL grown by MBE was recently reported.[49] It has been proposed that the absence of gallium in the InAs/InAsSb SL system can simplify the SL interfaces and hence the growth process,[50] and therefore result in longer carrier lifetimes.[46] The stabilized Fermi level due to intrinsic point defects in bulk InAs is expected to be above the CB edge, rendering any mid-gap defect states inactive for SRH processes. In comparison, the stabilized Fermi level for bulk GaSb is expected to be in the band gap near the VB edge, leaving the mid-gap states available for SRH recombination.[51] A minority carrier lifetime of ~ 412 nanoseconds at 77 K under low excitation for a LWIR InAs/$InAs_{0.72}Sb_{0.28}$ SL grown by MBE has been

reported,[52] thus demonstrating the possibility of Ga-free InAs/InAsSb SLs achieving longer carrier lifetimes.

1.4 Outline of dissertation

The research described in this dissertation has involved the use of transmission electron microcopy (TEM) techniques to characterize the microstructure properties of II-VI and III-V compound semiconductor heterostructures and superlattices. The materials investigated have included thick ZnTe epilayers (~2.4 μm) grown on various III-V substrates, GaSb grown on ZnTe virtual substrate with a temperature ramp during growth, and strain-balanced InAs/$InAs_{1-x}Sb_x$ T2SLs.

In chapter 2, essential information about material growth methods, including MOCVD and MBE, are provided. X-ray diffraction (XRD), photoluminescence (PL) and TEM techniques are briefly introduced. The sample preparation methods for TEM observation involved in this research are also described.

In chapter 3, the microstructure of thick ZnTe epilayers grown by MBE under virtually identical conditions on GaSb, InAs, InP and GaAs (100) substrates were compared using TEM. Digital image processing was used to analyze the distribution of misfit dislocations at the interfaces of the ZnTe/InP and ZnTe/GaAs samples. The amount of residual strain at the interfaces was estimated, and was compared to the XRD results. PL measurements of the four samples were also presented.

In chapter 4, GaSb layers grown on ZnTe virtual substrates with a temperature ramp at the beginning of the GaSb growth were investigated. The temperature ramp used differs in ramp rate or starting temperature. High-resolution XRD measurements and cross-section TEM images were used to study the material quality and interface morphology. Defect density was estimated from plan-view TEM images. Improved optical properties were demonstrated by PL measurements.

In chapter 5, the structural properties of strain-balanced InAs/$InAs_{1-x}Sb_x$ T2SLs for possible long-wavelength infrared applications grown on GaSb (001) substrates, by MOCVD and MBE, were investigated. High-resolution XRD measurements were used to determine the SL period and the Sb compositions. Microstructural properties, such as interface sharpness and ordered alloy structure, were characterized using TEM and STEM.

In chapter 6, the important results and achievements of this dissertation research are summarized, and possible studies that could be carried out in the future are described.

REFERENCES

[1]Robert F. Pierret, Semiconductor Device Fundamentals, Addison-Wesley (1996).

[2]Donald A. Neamen, Semiconductor Physics and Devices: Basic Principles, 3rd edition, McGraw-Hill (2003).

[3]C. Kittel, Introduction to Solid State Physics, John Wiley& Sons, Inc., New Jersey (2005).

[4]"This Month in Physics History, November 17 - December 23, 1947: Invention of the First Transistor", American Physical Society News (2000). http://www.aps.org/publications/apsnews/200011/history.cfm

[5]"Jack S. Kilby-Nobel Lecture". Nobelprize.org. http://www.nobelprize.org/nobel_prizes/physics/laureates/2000/kilby-lecture.html

[6]"The History of the Integrated Circuit". Nobelprize.org. http://www.nobelprize.org/educational/physics/integrated_circuit/history/

[7]A. G. Milnes and D. L. Feucht, Heterojunctions and Metal-Semiconductor Junctions, Academic Press (1972).

[8]S. M. Sze, and Kwok K. Ng, Physics of Semiconductor devices, 3rd edition, John Wiley& Sons (2007).

[9]A. I. Gubanov, Zh. Tekh. Fiz. 20, 1287 (1950).

[10]A. I. Gubanov, Zh. Tekh. Fiz. 21, 304 (1951).

[11]W. Shockley, U.S. Patent 2,569,347 (1951).

[12]H. Kroemer, Proc. IRE **45**, 1535 (1957).

[13]R. L. Anderson, Solid-State Electron. **5**, 341 (1962).

[14]Zh. I. Alferov, and R. F. Kazarinov, Inventor's Certificate No. 181737 with priority from March 30, 1963 (in Russian).

[15]H. Kroemer, Proc. IEEE **51**, 1782 (1963).

[16]Zh. I. Alferov, V. M. Andreev, V. I. Korol'kov, D. N. Tret' yakov, and V. M. Tuchkevich, Fiz. Tekn. Poluprovodn. **1**, 1579 (1967).

[17]H. S. Rupprecht, J. M. Woodall, and G.D. Pettit, Appl. Phys. Lett. **11**, 81 (1967).

[18]Zh. I. Alferov, Semiconductors **32**, 1 (1998).

[19]J. W. Matthews, J. Vac. Sci. Technol. **12**, 126 (1975).

[20]F. C. Frank, and J. H. van der Merwe, Proc. Roy. Soc. A **189**, 2005 (1949).

[21]K. Pinardi, U. Jain, S. C. Jain, H. E. Maes, R. Van Overstraeten, and M. Willander, J. Appl. Phys. **83**, 4724 (1998).

[22]M. G. Mil'vidskii, Semiconductor Heterostructures, Chapter 5, MIR Publishers (1989).

[23]Jeffery L. Gray, Handbook of Photovoltaic Science and Engineering, Chapter 3, John Wiley & Sons (2003).

[24]Steven S. Hegedus, and Antonio Luque, Handbook of Photovoltaic Science and Engineering, Chapter 1, John Wiley & Sons (2003).

[25]E. Becquerel, Comptes Rendus **9**, 561 (1839).

[26]D. Chapin, C. Fuller, and G. Pearson, J. Appl. Phys. **25**, 676 (1954).

[27]J. M. Woodball, and H. J. Hovel, Appl. Phys. Lett. **30**, 492 (1977).

[28]J. C. C. Fan. B. Y. Tsaur, and B. J. Palm, Proceedings of the 16th IEEE Photovoltaic Specialists Conference, p. 692, 1982.

[29]J. M. Olson, R. K. Ahrekiel, D. J. Dunlavy, B. Keyes, and A. E. Kibbler, Appl. Phys. Lett. **55**, 1208 (1989).

[30]M. Wiemer, V. Sabnis, H. Yuen, Proc. SPIE **8108**, 810804 (2011);

[31]Y.-H. Zhang, S.-Q. Yu, S.R. Johnson, D. Ding, S.-N. Wu, Proceedings of the 33rd IEEE Photovoltaic, Energy Specialist Conference, p. 20, 2008.

[32]S. Wang, S.-N. Wu, D. Ding, X. Liu, X.-B. Zhang, D.J. Smith, S.-Q. Yu, S.R. Johnson, J.K. Furdyna, Y.-H. Zhang, J. Cryst. Growth **311**, 2116 (2009).

[33]L. Esaki, and R. Tsu, IBM J. Res. Develop. **14**, 61 (1970).

[34]L. Esaki, IEEE J. Quantum Electron. **22**, 1611 (1986).

[35]K. Fujiwara, Semiconductor Superlattices: Growth and Electronic Properties, Chapter 1, World Scientific (1995).

[36]G. A. Sai-Halasz, R. Tsu, and L. Esaki, Appl. Phys. Lett. **30**, 651 (1977).

[37]H. Sakaki, L. L. Chang, G. A. Sai-Halasz, C. A. Chang, and L. Esaki, Solid State Commun. **26**, 589 (1978).

[38]G. C. Osbourn, J. Vac. Sci. Technol. B **2**, 176 (1984).

[39]M. O. Manasreh, and G. J. Brown, Semiconductor Quantum Wells and Superlattices for Long-Wavelength Infrared Detectors, Charpt 1, Artech House (1993).

[40]G. C. Osbourn, Semicond. Sci. Technol. **5**, S5 (1990).

[41]E. P. O'Reilly, Semicond. Sci. Technol. **4**, 121 (1989).

[42]C. Mailhiot, Semiconductor Quantum Wells and Superlattices for Long-Wavelength Infrared Detectors, Chapter 4, Artech House (1993).

[43]C .Maihiot, and D. L. Smith, J. Vac. Sci. Technol. B **5**, 1269 (1987).

[44]D. L. Smith, and C. Maihiot, J. Appl. Phys. **62**, 2545 (1987).

[45]I. Vurgaftman, C. L. Canedy, E. M. Jackson, J. A. Nolde, C. A. Affouda, E. H. Aifer, J. R. Meyer, A. Hood, A. J. Evans, and W. T. Tennant, Opt. Eng. **50**, 061007 (2011).

[46]C. H. Grein, M. E. Flatte and H. Ehrenreich, in Proceedings on the Third International Symposium on Long Wavelength Infrared Detectors and Arrays: Physics and Applications III, p. 211, 1995.

[47]S. Bandara, P. Maloney, N. Baril, J. Pellegrino, and M. Tidrow, Infrared Phys. Technol. **54**, 263 (2011).

[48]Y. B. Li, D. J. Bain, L. Hart, M. Livingstone, C. M. Ciesla, M. J. Pullin, P. J. P. Tang, W. T. Yuen, I. Galbraith, C. C. Phillips, C. R. Pidgeon, and R. A. Stadling, Phys. Rev. B **55**, 4589 (1997).

[49]E. H. Steenbergen, K. Nunna, L. Ouyang, B. Ullrich, D. L. Huffaker, D. J. Smith, and Y.-H. Zhang, J. Vac. Sci. Technol. B **30**, 02B107 (2012).

[50]Y. Huang, J.-H. Ryou, R. D. Dupuis, V. R. D'Costa, E. H. Steenbergen, J. Fan, Y.-H. Zhang, A. Petschke, M. Mandl, and S.-L. Chuang, J. Cryst. Growth **314**, 92 (2011).

[51]W. Walukiewicz, Mat. Res. Soc. Symp. Proc.**148**, 137 (1989).

[52]E. H. Steenbergen, B. C. Connelly, G. D. Metcalfe, H. Shen, M. Wraback, D. Lubyshev, Y. Qiu, J. M. Fastenau, A. W. K. Liu, S. Elhamri, O. O. Cellek, and Y.-H. Zhang, Appl. Phys. Lett. **99**, 251110 (2011).

Chapter 2

EXPERIMENTAL DETAILS

This chapter provides essential background information about the methods of growth for the materials that have been studied in this dissertation, including metalorganic chemical vapor deposition (MOCVD) and molecular beam epitaxy (MBE). X-ray diffraction (XRD), photoluminescence (PL) and transmission electron microscopy (TEM) techniques, including high resolution electron microscopy (HREM) and scanning transmission electron microscopy (STEM), which are heavily used in the experimental studies, are also introduced. Finally, some details about sample preparation for TEM observation are provided.

2.1 Material growth

2.1.1 MOCVD growth of InAs/$InAs_{1-x}Sb_x$ type-II superlattices

The MOCVD technique has been used for the growth of many materials and high performance devices, including virtually all of the III-V, II-VI, and IV-IV semiconductors.[1] It lends itself to mass production, since several wafers can be accommodated in an MOCVD reactor at the same time. For the growth of III-V semiconductors, MOCVD relies on the pyrolysis of metal-organic compounds containing group III elements in an atmosphere of hydrides containing group V elements. The fractional atomic composition in ternary compound semiconductors can be well controlled by fixing the flow rates and thus the partial pressures of the various reactants, while complex multilayer epitaxial structures can be readily

grown by exchanging one gas composition with another. High-quality compound semiconductor heterostructures with abrupt interfaces grown by MOCVD have been demonstrated.[2]

MOCVD-grown samples of various InAs/$InAs_{1-x}Sb_x$ type-II superlattices (T2SLs) were provided for examination by Professor Russell D. Dupuis and colleagues at Georgia Institute of Technology. The epitaxial growth was carried out using 2-inch (001) *n*-type GaSb substrates in a Thomas Swan MOCVD reactor system equipped with a close-coupled showerhead growth chamber at a pressure of 100 Torr. Epi-Pure^{TM} trimethyIindium (TMIn, $In(CH_3)_3$) and trimethylgallium (TEGa, $Ga(C_2H_5)_3$) were used as column III precursors, and trimethylantimony (TMSb, $Sb(CH_3)_3$) and arsine (AsH_3) were used as column V precursors. Prior to growth, the substrates were cleaned in HCl to remove the native surface oxide and then rinsed in isopropyl alcohol followed by blow-drying in N_2. The growth was typically initiated by depositing a 100-nm-thick GaSb buffer layer at 600 ºC. The growth temperature was then ramped down to 500 ºC for all layers in the InAs/InAsSb T2SL structures, with a typical growth rate of ~0.1 nm/s.[3]

2.1.2 MBE growth

MBE, first applied to the growth of III-V compound semiconductors,[4,5] is suitable for growing epitaxial films of a wide range of materials. MBE provides several advantages over other growth techniques, such as precise control of the growth rate, atomically abrupt crystalline interfaces and rapid change in atomic

composition. Figure 2.1 shows a schematic of a basic MBE growth chamber. It primarily consists of an ultrahigh-vacuum (UHV) chamber, effusion cells for the source materials, a substrate heating holder and a cooling panel. In the MBE growth process, localized beams of atoms or molecules are incident upon the heated substrate, with a previously processed clean surface, in the UHV environment. The arriving constituent atoms then form an epitaxial film on the crystal surface. The UHV conditions avoid incorporation of unwanted impurities,

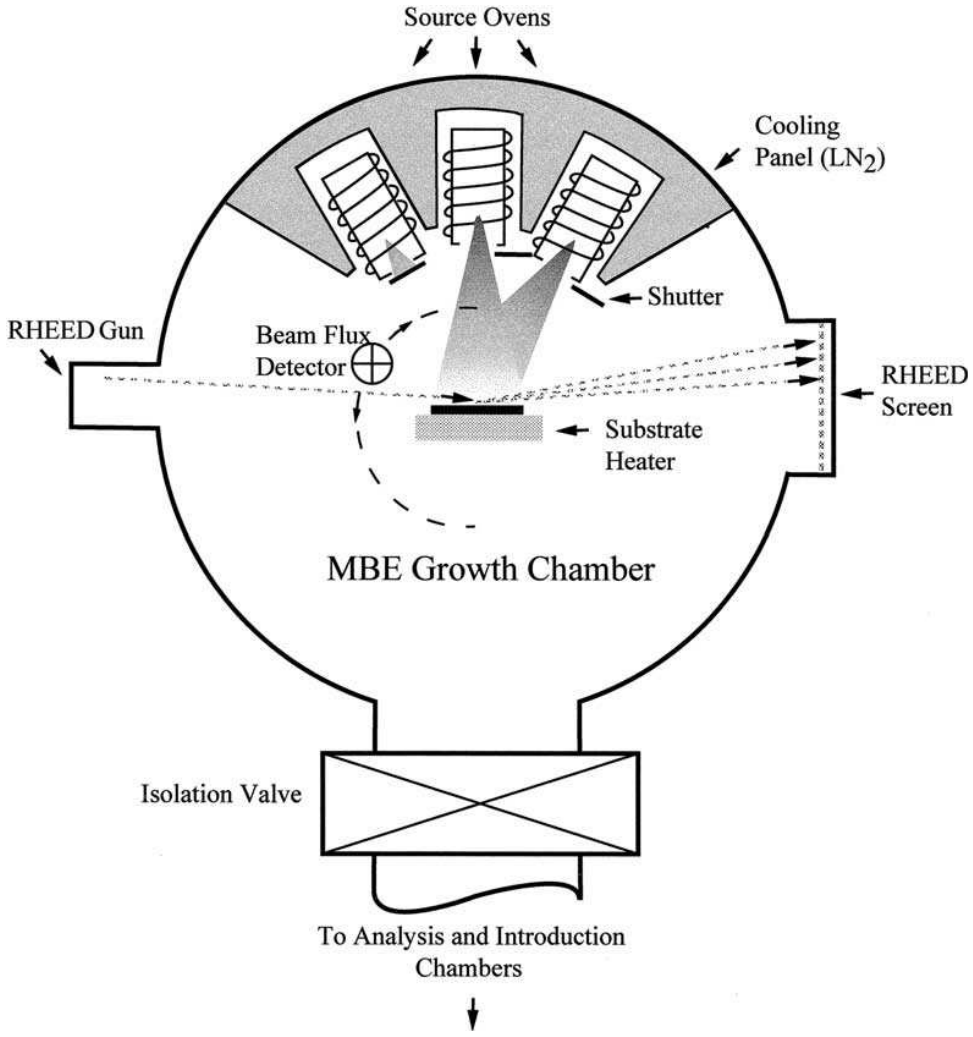

Fig. 2.1. Schematic illustration of a basic MBE growth chamber.[6]

and the cooling panel helps to avoid thermal interference and suppresses outgasing from the chamber wall. Mechanical shutters that are operated from outside the vacuum chamber are used to switch the beam fluxes on and off. Reflection-high-energy electron diffraction (RHEED) system is commonly used to monitor growth, and can also provide information about any ordering of the crystal surface during growth.

The control of composition in mixed-group-III alloys, such as $Ga_xIn_{1-x}As$, is relatively straightforward, and is achieved simply by changing the group-III beam flux ratios. This is because the sticking coefficients and growth parameters are similar for most group-III species. However, there are large differences in the incorporation coefficients for group-V species, such as As and Sb. Therefore, accurate control of compositions and reproducibility of mixed-group-V alloys becomes challenging. The modulated MBE technique was initially developed to provide more accurate control of As and Sb incorporation ratio in mixed-group-V alloys, such as $AlAs_xSb_{1-x}$, during solid-source MBE growth.[7,8] Modulated MBE growth uses timing of the shutter operation rather than changes in the incident flux ratios to control the group-V incorporation and composition. Fig. 2.2 shows a schematic time sequence for the As and Sb shutter positions during the modulated MBE growth of an $InAs_{1-x}Sb_x$ alloy, with x determined by the ratio of $Sb_{shutter-time}/(As_{shutter-time} + Sb_{shutter-time})$. This modulated MBE growth technique yields an ordered alloy structure, in effect building a short-period SL within the alloy, and has been demonstrated to produce improved crystalline quality and enhanced optical properties.[7,8]

2.1.3 MBE growth of InAs/$InAs_{1-x}Sb_x$ T2SLs

Samples of InAs/$InAs_{1-x}Sb_x$ T2SLs, with random and ordered $InAs_{1-x}Sb_x$ alloys, were grown by Professor Diana. L. Huffaker and her group at University of California, Los Angeles. The epitaxial growth was carried out in a solid-source MBE system, using both conventional and modulated MBE growth techniques. All samples nominally consisted of a 0.2-μm-thick GaSb buffer layer grown on an *n*-type GaSb (001) substrate at 500˚C, followed by deposition of 7-nm-thick $InAs_{1-x}Sb_x$ layers alternating with 18-nm-thick InAs layers for 20 periods, at a growth temperature of 435˚C. Finally, a 0.1-μm-thick GaSb capping layer was deposited at 480˚C. During the modulated MBE growth of these $InAs_{1-x}Sb_x$ layers, the In shutter was kept open throughout the entire growth period, while the As and Sb shutters were alternately opened and closed for very short periods.

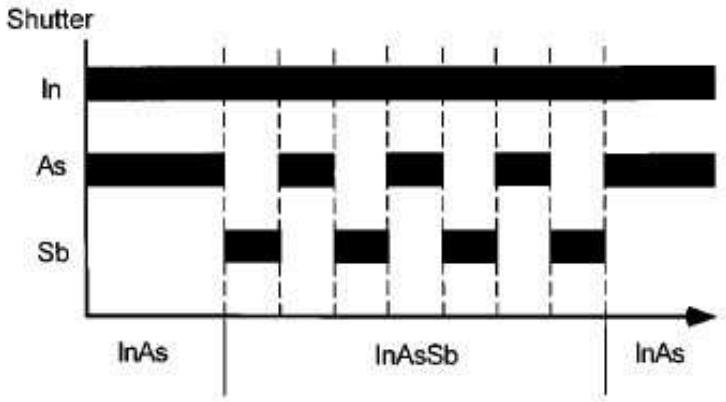

Fig. 2.2. Schematic illustration of In, As and Sb shutter sequences during the modulated MBE growth of InAsSb alloy layers and InAs layers. The filled bars represent intervals when the corresponding shutters are open.[9]

Samples of other MBE-grown InAs/$InAs_{1-x}Sb_x$ T2SLs studied in this thesis were grown by Dr. Amy. Liu and colleagues at IQE, Inc., and Professor Yong-Hang Zhang and colleagues at Arizona State University (ASU), respectively. The growth conditions used were similar; more details about these specific samples are included in Chapter 5.

2.1.4 MBE growth of ZnTe and GaSb materials

Samples of ZnTe epilayers grown on GaAs, InP, InAs and GaSb (001) substrates, and samples of GaSb epilayers grown on ZnTe virtual substrates were provided by Professor Jacek K. Furdyna and Dr. Xinyu Liu at University of Notre Dame. The epitaxial growth was carried out using a Riber 32 MBE system consisting of two separate III-V and II-VI growth chambers, which were connected via a UHV transfer module. The vacuum of this transfer chamber was typically about 5×10^{-9} Torr, which prevented any significant contamination during sample transfer. The substrate temperatures were measured with a thermocouple on the back of the substrate holder. During ZnTe growth, the substrate temperature was 330 ˚C and the flux ratios of Zn to Te (1.2:1) were adjusted to optimize the growth conditions by monitoring the surface reconstructions using RHEED. During the growth of GaSb on the ZnTe virtual substrate, a thin GaSb transition layer was deposited first under a temperature ramp, such as from 320˚C to 470˚C during a period of 200 seconds, and the remaining GaSb epilayer was then deposited at the normal growth temperature of 470˚C.

2.2 X-ray diffraction

When X-rays pass through materials, scattering occurs and some incident photons are deflected away from the original direction of travel. These elastically scattered X-rays do not lose energy, but they carry information about the atomic structure of the material. When the atoms are arranged in a periodic manner, such as in a crystalline material, the diffracted waves consist of sharp interference peaks that are directly related to the atomic separations. By measuring the diffraction pattern, the distribution of atoms in the material can be deduced.[10-12] High-resolution XRD can be used to characterize lattice mismatch, misorientation, thickness, alloy composition, dislocation, relaxation and strain in epitaxial films.[13]

The high-resolution XRD measurements reported in this thesis were performed using a PANalytical X'pert Pro MRD. Diffraction patterns from the multilayered heterostructures consisted of satellite peaks surrounding the primary diffraction peaks originating from the epitaxial film. The SL periods of InAs/InAsSb T2SLs and Sb compositions in $InAs_{1-x}Sb_x$ alloys were determined by comparing simulations with (004) high-resolution XRD measurements.

2.3 Photoluminescence

PL is a process that includes optical excitation and luminescence. PL spectroscopy is an important technique for studying the optical and electronic properties of semiconductors, because of its high-sensitivity, contactless and nondestructive character. During the PL process, photon absorption by

semiconductors, considered as the optical excitation, generates electron-hole pairs that are separated in the conduction band (CB) and valence band (VB). The electron-hole pairs could easily recombine in different ways that could possibly transform the energy to heat or light. The light energy can be dissipated as radiation, which results in luminescence emission by the semiconductor. The radiative energy of the emitted photon from one energy band to another energy band is determined by the band structure of the semiconductor. The mechanism of PL of semiconductors excited by photons with energy no less than the band gap is shown in Fig. 2.3. Transitions II and III are radiative, which can give rise to PL phenomena, while transition IV is non-radiative. The radiative transitions from the bottom of CB to the top of VB, such as transition II shown in Fig. 2.3, emit energy that is equal to the band-gap energy. There are other radiative transitions, such as donor to valence band, conduction band to acceptor band, and donor to acceptor, which generate excitonic PL signal. Those transitions involve energy levels lying within the semiconductor forbidden band that are attributed to impurity atoms, intrinsic defects or surface vacancies.[14,15]

The PL measurements reported in chapter 3 were performed using the 488-nm line of an Argon ion laser for excitation, and a high-resolution grating spectrometer equipped with a photomultiplier was used for detection. The PL measurements reported in chapter 4 were carried out using the 780-nm line of a laser diode for excitation, and a Fourier transform infrared spectrometer configured with a quartz beam splitter and liquid-nitrogen-cooled InSb detector was used for detection.

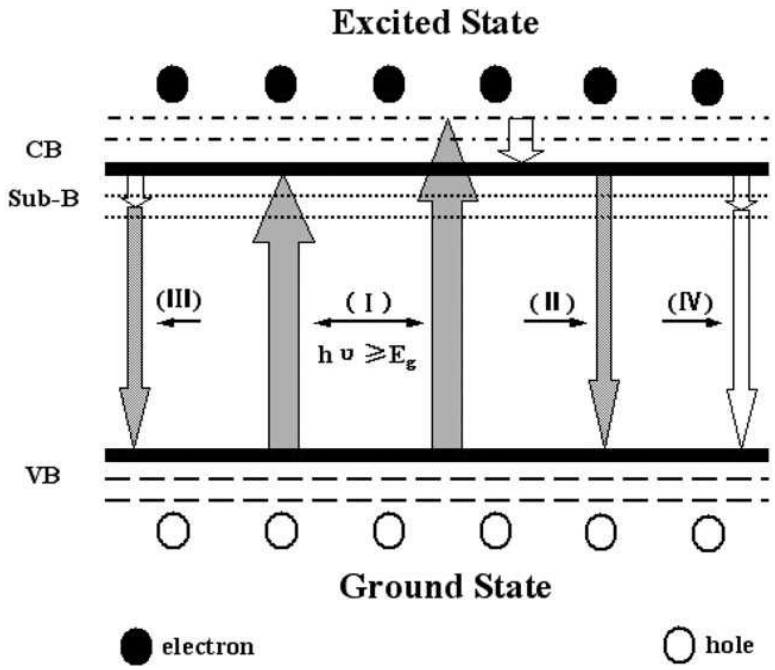

Fig. 2.3. The mechanism of PL of a semiconductor excited by photons with energy no less than the band gap: (I) photon absorption; II) CB-to-VB radiative transition; (III) excitonic PL process; and (IV) non-radiative transition.[15]

2.4 Transmission Electron Microscopy

2.4.1 High resolution electron microscopy

Conventional TEM uses amplitude contrast with a small objective aperture for image formation, whereas HREM imaging uses phase contrast resulting from the interference of several electron beams over a wider range of scattering angles. Phase contrast imaging is sensitive to many factors, including specimen thickness, specimen orientation and atomic scattering factors, and is also strongly affected by properties of the imaging system, such as variations in the focus and spherical aberration of the objective lens.[16] HREM allows imaging of the crystal structure

of thin specimens at the atomic scale, and thus individual atom columns can be resolved. The applications of HREM to diverse materials, such as semiconductors, metals, oxides and ceramics, and to the study of dislocations, interfaces and surfaces have been widely reported at many scientific conferences and in the scientific literature.[17]

Both phase-contrast and diffraction-contrast images reported in this dissertation were recorded using an JEOL JEM-4000EX high-resolution electron microscope operated at 400 kV. This microscope is equipped with a double-tilt, top-entry sample holder, which can provide high stability against sample drift, and it has a structural resolution of ~1.7 Å. The microscope was always corrected for objective-lens astigmatism and axial coma before images were taken. Digital image processing based on lattice-fringe images was performed using Gatan DigitalMicrograph software.

2.4.2 Scanning transmission electron microscopy

A schematic diagram of a STEM instrument is shown in Fig. 2.4. The image-forming lens focuses the electron beam to form an atomic-scale probe at the specimen, and two pairs of scan coils are used to raster the probe over the sample. The focused beam passes through the sample and is scattered in all directions, so that a wide range of possible signals is available. The transmitted electrons that leave the sample at relatively low angles (smaller than ~10 mrad) with respect to the optic axis are used to form bright-field images, while the electrons scattered at relatively high angles can be collected by an annular-dark-

field (ADF) detector. The technique of energy-dispersive X-ray spectroscopy (EDXS) makes use of X-ray generated by electronic excitations in the sample to provide information about elemental distribution. In addition, transmitted electrons that have lost measurable amounts of energy when passing through the sample are analyzed using the technique of electron-energy loss-spectroscopy (EELS) to extract further information about local variations in sample composition.[16,18]

High-angle annular-dark-field (HAADF) images are obtained from the collection of incoherently scattered electrons at relatively very high angles (larger than ~50 mrad) using the ADF detector, as initially developed by Crewe and colleagues.[17] The image contrast is strongly correlated to the thickness and atomic number Z of the specimen, and can provide direct identification of atomic structure at heterostructure interfaces, based on atomic number. HAADF imaging, often referred to as Z-contrast imaging, relies on Rutherford scattering, and diffraction-contrast effects are smoothed out.[16] In practice, the image intensity can be expressed in the form of $I \sim Z^{\upsilon}$, where υ is usually in the range between 1.6 and 1.9 depending on the inner and outer ADF detection angles.[20]

The HAADF images reported in this thesis were taken using an JOEL 2010F TEM operated at 200 kV. This microscope is equipped with a field-emission electron gun, double-tilt sample holder, charge-coupled-device (CCD) camera, ADF detector, EDX and EELS detectors. It has a structural resolution of 1.9 Å in TEM imaging mode and an instrumental resolution of 1.4 Å in ADF-STEM mode. The focused probe size can be as small as 0.2 nm for the STEM

imaging mode, and the camera length is reduced to 6cm for HAADF imaging using the ADF detector.

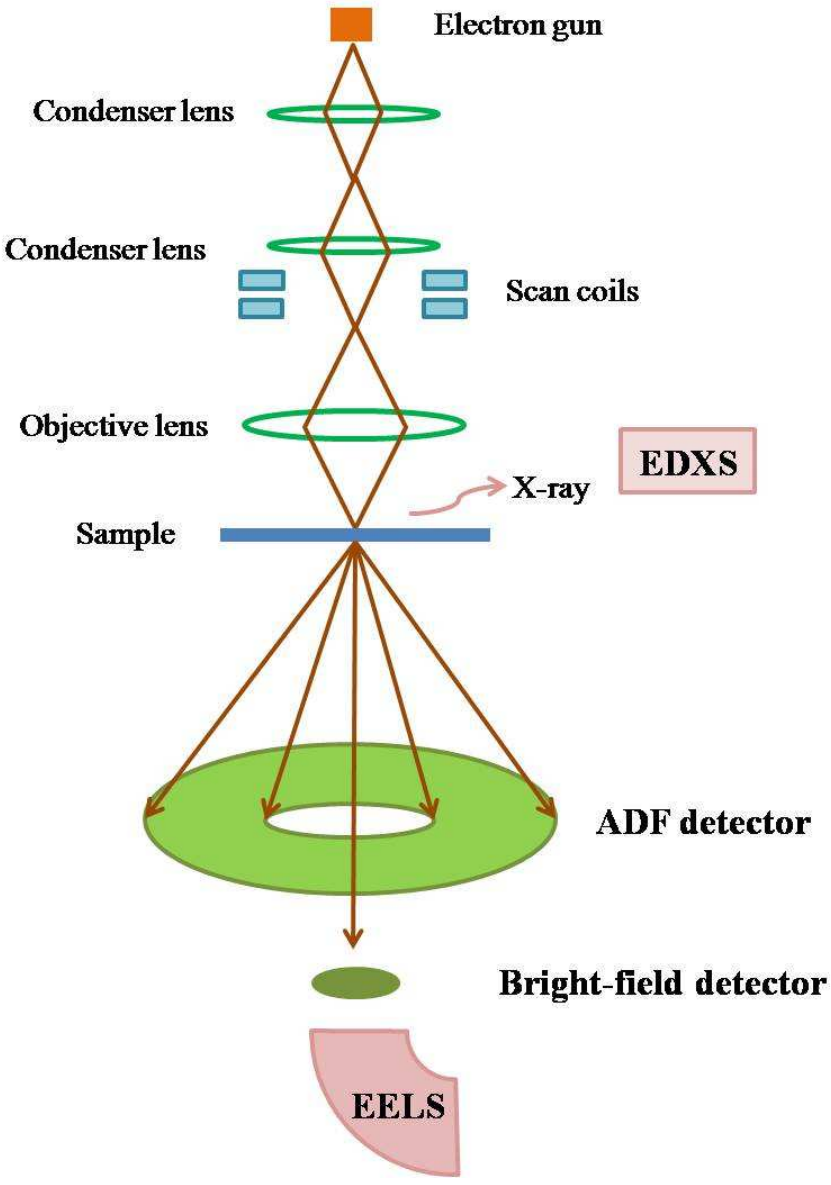

Fig. 2.4. Schematic diagram showing the essential components of the STEM.

2.5 TEM sample preparation

2.5.1 Cross-sectional sample preparation

For cross-sectional TEM observation, samples were cut into slabs with sizes of about 2.5 mm × 1.5 mm using a diamond wafer blade, and the two pieces were then glued together using M-bond, with face-to-face epitaxial film layers. Mechanical polishing successively using 30 µm, 9 µm, 3 µm, 1 µm and 0.1 µm diamond lapping films, followed by dimpling using a cloth wheel, typically reduced the sample thicknesses to ~10 µm. The samples were then glued to copper grids suitable for the TEM sample holder. Finally, the specimens were thinned by argon ion-milling at low energy (2.5~3 keV), using double-mode of the Gatan Model 691 precision ion polishing system (PIPS), until small holes were formed in the films. A liquid-nitrogen-temperature cooling stage was used during ion-milling for all specimens studied in this dissertation to minimize any thermal or ion-beam damage.[21] All cross-sectional samples were prepared for observation along {110}-type zone-axis projections so that the direction of the incident electron beam could be aligned perpendicular to the growth surface normal.

2.5.2 Plan-view sample preparation

For plan-view TEM observation, samples were cut into slabs with sizes of about 2.5 mm × 2.5 mm using the diamond wafer blade. Mechanical polishing using 30 µm, 9 µm, 3 µm, 1 µm and 0.1 µm diamond lapping films, and dimpling using copper and cloth wheels, were applied to thin specimens from the substrate

side only down to ~10-μm thickness. The specimens were glued to copper girds and finally thinned from the backside only using argon ion-milling at low energy (2.5~3 keV), off-mode of Gatan Mode 691 PIPS, until small holes appeared. The liquid-nitrogen-temperature cooling stage was again used during ion-milling to minimize any thermal or ion-beam damage. All plan-view samples were prepared for observation along the growth direction so that the direction of the electron beam would be aligned parallel to the crystal surface normal.

2.5.3 Focused ion beam

Focused ion beam (FIB) technique was also used for TEM cross-sectional sample preparation for InAs/InAsSb T2SLs. This technique has been widely used for preparing TEM specimens of various materials, including semiconductors, metal, ceramics, polymers, biological materials and tissues. Most instruments nowadays combine the scanning electron microscope (SEM) and FIB column, and the system is called "DualBeam", "CrossBeam" or "Multibeam", depending on the vendor. The FIB system uses a Ga^+ ion beam to raster over the surface of a sample in a similar way as the electron beam in an SEM. The generated secondary electrons (or ions) are collected to form an image of the sample surface. The major advantages of FIB over conventional TEM specimen preparation methods are that samples can be extracted from specific areas, and large uniform thin areas can be obtained. However, there are well known Ga^+ ion-beam-induced damage existing in FIB-prepared TEM specimens. Ga^+ ions are implanted into the

specimen, which will affect the local composition of the material. The implantation will also amorphize the specimen surface.[22]

TEM cross-sectional samples of InAs/InAsSb T2SLs were prepared using an FEI Nova 200 FIB system. To minimize FIB damage, a platinum protection layer was first deposited over the area of interest to protect the film, as illustrated in Fig. 2.5 (a). Low-energy low-current milling was also used during the final stage of milling to minimize ion damage. Figure 2.5 (b) shows an XTEM image of the InAs/InAsSb T2SL sample prepared by FIB. No major structural changes in the SL layers were caused by the FIB milling, but the mottled appearance of the SL layers suggested that some damage had occurred.

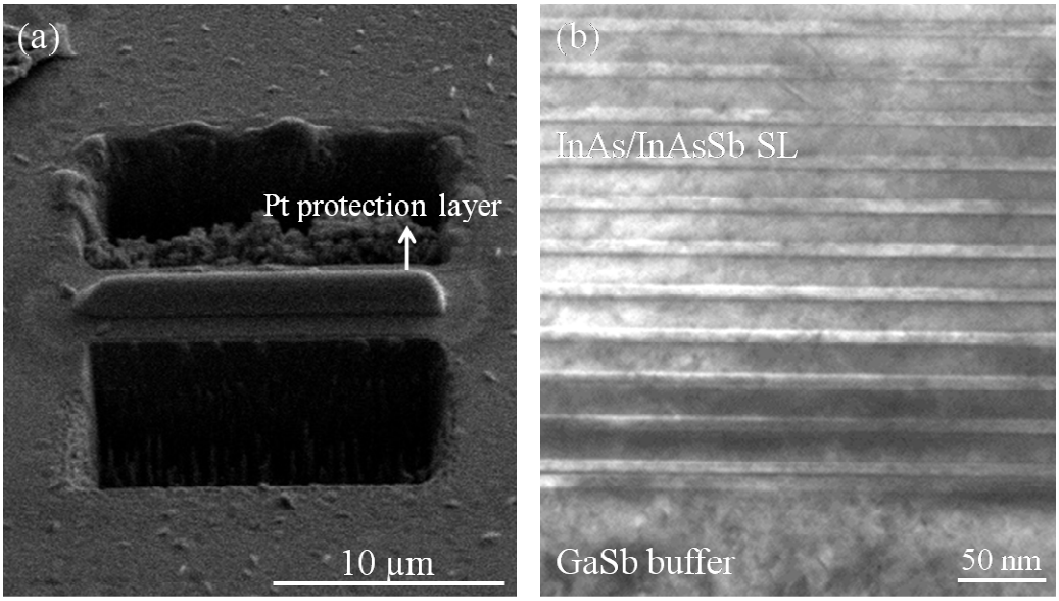

Fig. 2.5. (a) Scanning electron micrograph showing the Pt protection layer; (b) XTEM image of the InAs/InAsSb SL sample prepared using FIB technique.

REFERENCES

[1]P. D. Dapkus, Ann. Rev. Mater. Sci. **12**, 243 (1982).

[2]R. D. Dupuis, P. D. Dapkus, C. M. Garner, C. Y. Su, and W. E. Spicer, Appl. Phys. Lett. **34**, 335 (1979).

[3]Y. Huang, J.-H. Ryou, R. D. Dupuis, V. R. D'Costa, E. H. Steenbergen, J. Fan, Y.-H. Zhang, A. Petschke, M. Mandl, and S.-L. Chuang, J. Cryst. Growth **314**, 92 (2011).

[4]J. R. Arthur, J. Appl. Phys. **39**, 4032 (1968).

[5]A.Y. Cho, Surf. Sci. **17**, 494 (1969).

[6]J. R. Arthur, Surface Science **500**, 189 (2002).

[7]Y.-H. Zhang, and D. H. Chow, Appl. Phys. Lett. **65**, 3239 (1994).

[8]Y.-H. Zhang, J. Cryst. Growth **150**, 838 (1995).

[9]A. Y. Lew, E. T. Yu, and Y.-H. Zhang, J. Vac. Sci. Technol. B **14**, 2940 (1996).

[10]B. D. Cullity, and S. R. Stock, Elements of X-Ray Diffraction, 3rd Edition, Prentice Hall (1990).

[11]B. E. Warren, X-Ray Diffraction, Dover Publications (1990).

[12]J. Als-Nielsen, and Des McMorrow, Elements of Modern X-ray Physics, John Wiley & Sons (2001).

[13]D. K. Bowen, and B. K. Tanner, High Resolution X-ray Diffractometry and Topography, Taylor & Francis (1998).

[14]L. Peraldo Bicelli, Surface Technology **26**, 93 (1985).

[15]L. Jing, Y. Qu, B. Wang, S. Li, B. Jiang, L. Yang, W. Fu, H. Fu, and J. Sun, Solar Energy Materials & Solar Cells **90**, 1773 (2006).

[16]D. B. Williams, and C. B. Carter, Transmission Electron Microscopy, Springer (1996).

[17]D. J. Smith, Rep. Prog. Phys. **60**, 1513 (1997).

[18]P. D. Nellist, Scanning Transmission Electron Microscopy: Imaging and Analysis, Chapter 2, Springer (2011).

[19]A. V. Crewe, and J. Wall, J. Mol. Biol. **48**, 375 (1970).

[20]P. Hartel, H. Rose, and C. Dinges, Ultramicroscopy **63**, 93 (1996).

[21]C. Z. Wang, D.J. Smith, S. Tobin, T. Parodos, J. Zhao, Y. Chang, and S. Sivananthan, J. Vac. Sci. Technol. A **24**, 995 (2006).

[22]L. A. Giannuzzi, and F.A. Stevie, Micron **30**, 197 (1999).

Chapter 3

MICROSTRUCTURAL CHARACTERIZATION OF THICK ZnTe EPILAYERS GROWN ON LATTICE-MATCHED AND LATTICE–MISMATCHED III-V SUBSTRATES

This chapter describes a comprehensive investigation of thick ZnTe epilayers (~2.4 μm) grown under virtually identical conditions on GaSb, InAs, InP and GaAs (100) substrates using molecular beam epitaxy (MBE). This work was carried out in collaboration with Prof. Y.-H. Zhang and colleagues at Arizona State University, and Professor J. K. Furdyna and colleagues at University of Notre Dame. The samples were grown by Dr. Xinyu Liu at University of Notre Dame; and photoluminescence (PL) measurements were performed by Jin Fan at Arizona State University. My role in this work involved microstructural characterization using electron microscopy and analysis of the distribution of misfit dislocations at the heterointerfaces. The major results of this study have been published elsewhere.[1]

3.1 Introduction

There is much current interest in strategies to increase solar cell efficiency by taking advantage of a greater portion of the solar energy spectrum. One obvious approach is to use a multi-junction design based on semiconductor materials with band gaps that span a broad spectral range. The monolithic integration of II-VI (MgZnCd)(SeTe) and III-V (AlGaIn)(AsSb) alloys that are

lattice-matched to the so-called 6.1-Å substrates of either GaSb or InAs provides one possible option for achieving this objective.[2,3] ZnTe is a compound semiconductor with a direct energy gap (2.27 eV at room temperature) that covers the short-wavelength range of the solar spectrum. Moreover, with a lattice constant of 6.1037 Å, ZnTe is nearly lattice-matched to GaSb and InAs, as illustrated in Fig. 3.1. The thermal expansion coefficient of ZnTe is also very close to that of GaSb. Thus, ZnTe epilayers might be anticipated to have very low densities of interfacial misfit dislocations when grown on substrates of these materials. Conversely, InP and GaAs are III-V semiconductors that have greater lattice mismatch with ZnTe. However, large-area semi-insulating InP and GaAs wafers of high quality are commercially available, and less expensive in comparison with GaSb wafers, which could become important when considering the possible use of ZnTe epilayers on III-V substrates for device applications. Hence, these latter III-V materials are also potentially of interest as alternative substrates for ZnTe growth. Thick ZnTe epilayers with high quality on these different III-V substrates could serve as virtual substrates for other 6.1-Å compound semiconductors, which would provide the possibility to achieve high quality materials and to reduce the overall material cost at the same time for both optoelectronic and electronic device applications.

The growth of ZnTe epilayers on III-V substrates has been investigated extensively over several decades, as described for example in references.[4-11] This chapter reports a comprehensive study on a set of four, thick ZnTe epilayers that were grown on GaSb, InAs, InP and GaAs (100) substrates under virtually

identical growth conditions using the technique of molecular beam epitaxy (MBE). Microstructural characterization of these four samples was carried out using transmission and high-resolution electron microscopy (HREM). Interfacial misfit dislocations are analyzed using digital image processing to estimate strain relaxation. PL is applied to characterize the optical properties of the ZnTe epilayers. Further material properties of these same samples have also been determined using *in situ* reflection-high-energy electron diffraction (RHEED) and high-resolution X-ray diffraction, as reported elsewhere.[12]

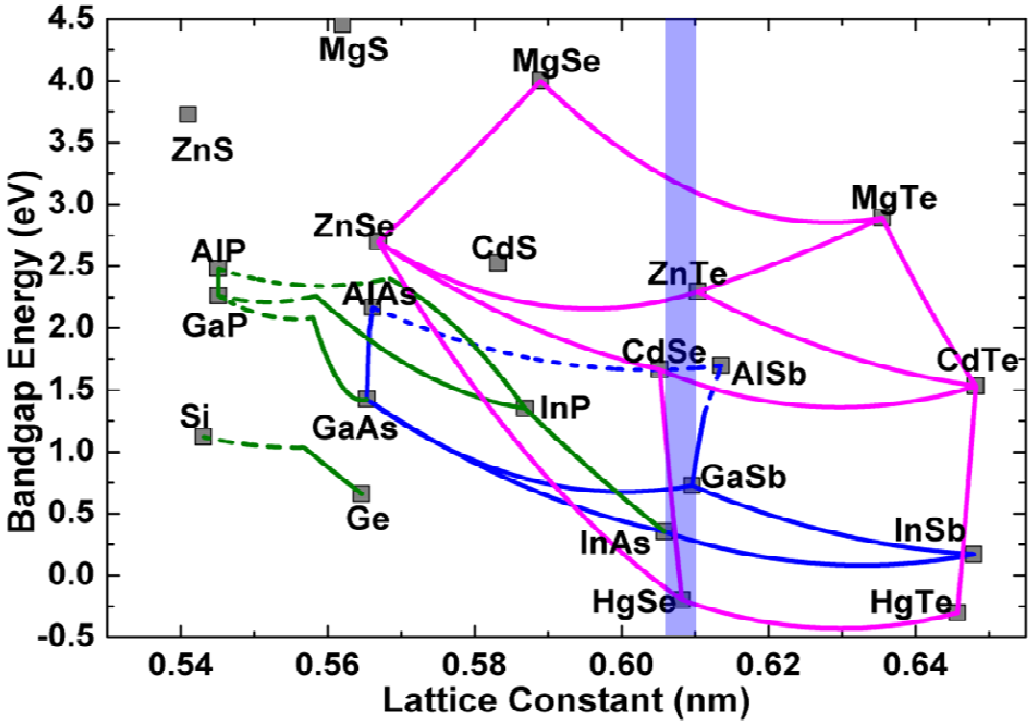

Fig. 3.1. Lattice constants and band gaps for some III-V, II-VI and IV semiconductor materials at room temperature.[2]

3.2 Experimental details

The epitaxial growth was carried out using a Riber 32 MBE system consisting of two separate III-V and II-VI chambers, which were connected via an ultrahigh-vacuum transfer module. Before the ZnTe growth was initiated, the separate GaSb, InAs, InP and GaAs (100) substrates were first deoxidized in the III-V chamber, followed by growth of the corresponding buffer layers (except in the case of InP). After cooling down to room temperature, the samples were transferred under vacuum to the II-VI chamber where Zn irradiation of the substrate surface was performed for ~300 seconds. Thick ZnTe layers, with nominal thicknesses ~ 2.4μm, were then deposited on the buffer layers. During ZnTe growth, the substrate temperature was 330 ˚C and the flux ratios of Zn to Te (close to 1) were adjusted to optimize the growth conditions by monitoring the surface reconstructions using RHEED. Table 3.1 lists some information about the growth of this set of samples.

Table 3.1. Growth information for ZnTe on different III-V substrates samples.

Substrate	**Zn: Te flux ratio**	**Growth rate (nm/s)**
GaSb	1.2:1	0.31
InAs	1.2:1	0.30
InP	1.2:1	0.28
GaAs	1.2:1	0.30

Cross-sectional specimens were prepared for transmission electron microscopy (TEM) observation using mechanical polishing and dimpling followed by argon ion-milling. The mechanical polishing and dimpling reduced the sample thicknesses to 10~12 μm, and small holes in the films were then made by ion-milling at low energy (2.5~3 keV), using a liquid-nitrogen-temperature cooling stage to minimize any thermal or ion-beam damage.[13] Before the sample milling was finished, lower-energy (2 keV) ion beams were briefly used to clean the surface. The TEM characterization studies were mostly carried out using a JEM-4000EX high-resolution electron microscope operated at 400 keV and with a structural resolution of ~1.7Å. All samples were prepared for observation along {011}-type zone-axis projections so that the direction of the electron beam would be perpendicular to the surface normal. Selected-area electron diffraction (SAED) patterns were typically taken from 0.5-micron-diameter regions overlapping the hetero-interfaces. For the characterization of optical properties, temperature-dependent PL measurements were carried out using the 488-nm line of an Argon ion laser for excitation and a high-resolution grating spectrometer equipped with a photomultiplier for detection.

3.3 Results and discussion

Lattice mismatch between tetrahedrally bonded semiconductors has received much attention over many years.[14] The lattice mismatch, f, between the various III-V substrates (a_s) and the ZnTe epilayers (a_l = 6.1037Å at room temperature) is given by the expression

Table 3.2. Relevant substrate parameters for growth of ZnTe. The ideal Lomer dislocation separation are based on the room-temperature lattice parameters.

Substrate	Lattice parameter (Å)	Lattice mismatch (%)	Thermal expansion coefficient (1×10^{-6} K^{-1})	Dislocation separation (Å)
ZnTe	6.1037	-	8.33	-
GaSb	6.0959	-0.13	6.35	3320
InAs	6.0584	-0.74	5.00	579.0
InP	5.8686	-3.85	4.56	107.8
GaAs	5.6533	-7.38	5.75	54.2

$$f = (a_s - a_l) / a_l \quad (1)$$

The values of lattice mismatch for the GaSb, InAs, InP, and GaAs substrates are given in Table 3.2. Other relevant structural parameters for the four substrates and the ZnTe epilayer are also listed.

3.3.1 Microstructural characterization

Cross-sectional electron micrographs of the ZnTe/GaSb sample revealed very high quality ZnTe epilayers with very low density of interfacial defects. As illustrated by the diffraction-contrast image shown in Fig. 3.2 (a), the separation between these defects was typically considerably greater than 100 nm. This morphology was attributed to the very small lattice mismatch (-0.13%) between

the two materials. The ZnTe/GaSb interface was highly coherent overall and very little strain-related contrast was visible away from the interface. Moreover, the precise position of the interface was extremely difficult to pinpoint in HREM images, due to the closely similar average atomic numbers of the two materials. A representative high-magnification image of a region close to the ZnTe/GaSb interface (arrowed) is shown in Fig. 3.2 (b).

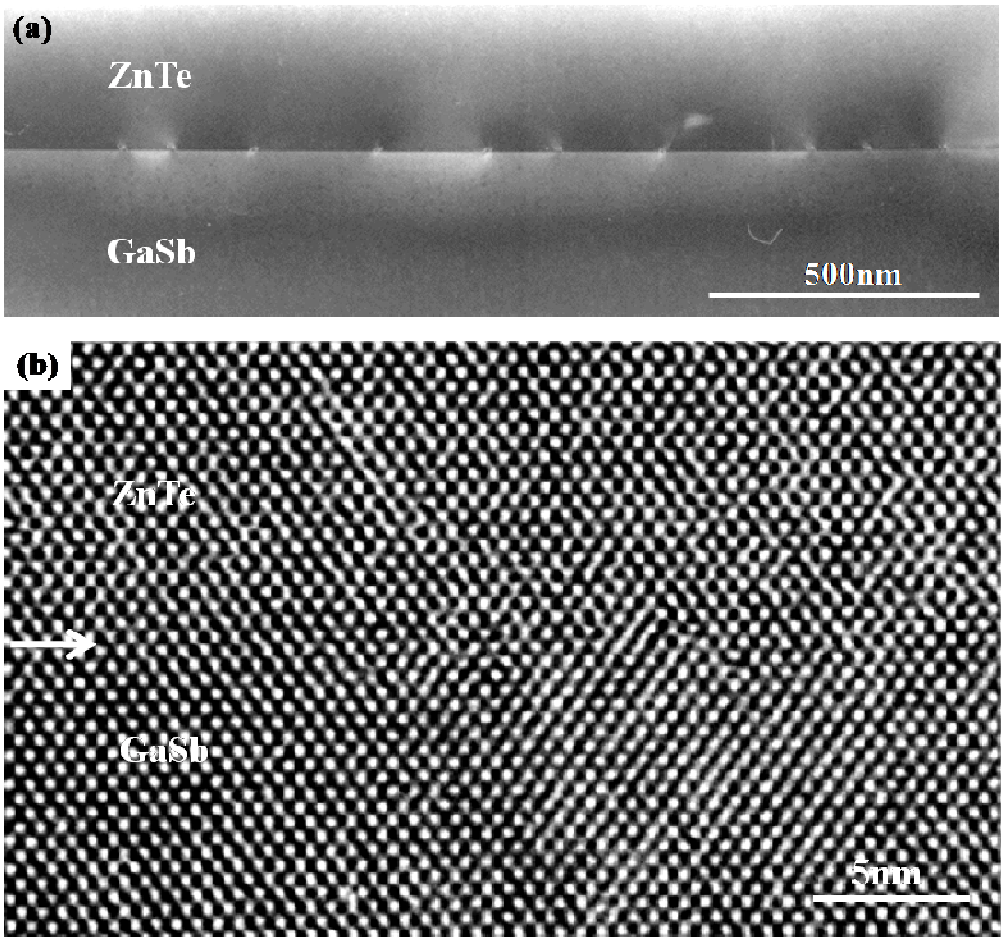

Fig. 3.2. (a) Cross-sectional electron micrograph of ZnTe/GaSb sample showing highly-separated misfit dislocations at the interface; (b) HREM image establishing highly coherent nature of the ZnTe/GaSb interface (arrowed).

Low magnification, diffraction-contrast, images of the ZnTe/InAs sample revealed occasional interfacial misfit dislocations, and some strain-related contrast was also apparent at the ZnTe/InAs interface, presumably as a result of the slightly larger lattice mismatch (-0.74%) between the two materials. It was also noteworthy that the density of defects in the ZnTe epilayer dropped off rapidly with distance away from the interface, as clearly shown by the example in Fig. 3.3 (a). Nevertheless, as should be apparent from the representative high-magnification image in Fig. 3.3 (b), there was again a marked absence of misfit dislocations along the interface (arrowed). Very few defects were visible in the ZnTe epilayers, and the exact position of the interface was again hard to identify in high-resolution electron micrographs except for those locations where interfacial misfit dislocations were present.

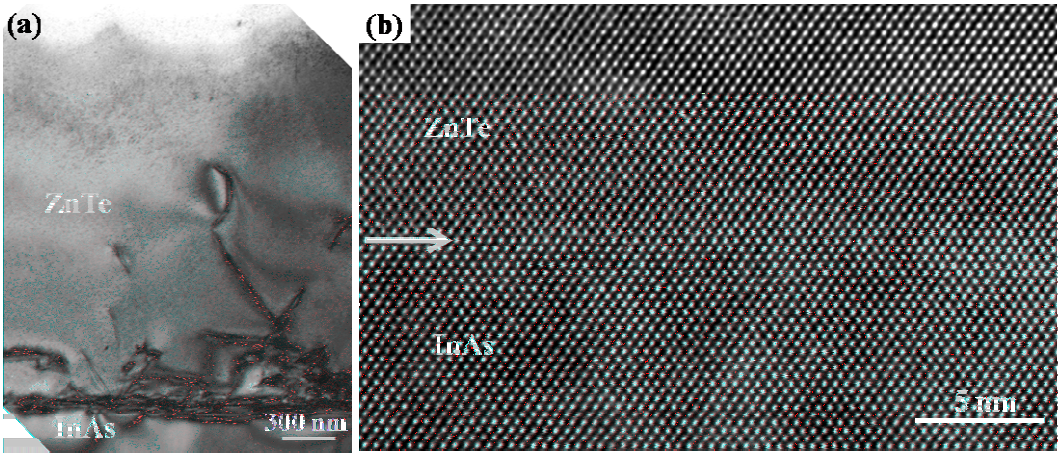

Fig. 3.3. (a) XTEM image of ZnTe/InAs sample showing rapid falloff in defect density upon moving away from the interface region; (b) HREM image showing enlarged view of the ZnTe/InAs interface (arrowed) region without any defects.

In the case of the ZnTe/InP sample, low-magnification images, such as Fig. 3.4 (a), showed high defect densities close to the hetero-interface, whereas regions near the ZnTe top surface appeared to be virtually free of defects. SAED patterns taken from the interface region, such as shown in Fig. 3.4 (b), demonstrated that the lattice constant of the ZnTe epilayer at the interface already differed from that of the substrate. The sharpness of the ZnTe spots in the SAED pattern also confirms the highly-crystalline nature of the ZnTe epilayer. HREM images revealed the presence of interfacial misfit dislocations, as indicated by the arrows in Fig. 3.5 (a), which were not usually spatially well-ordered. The most common types of defects observed at the interface were found after close

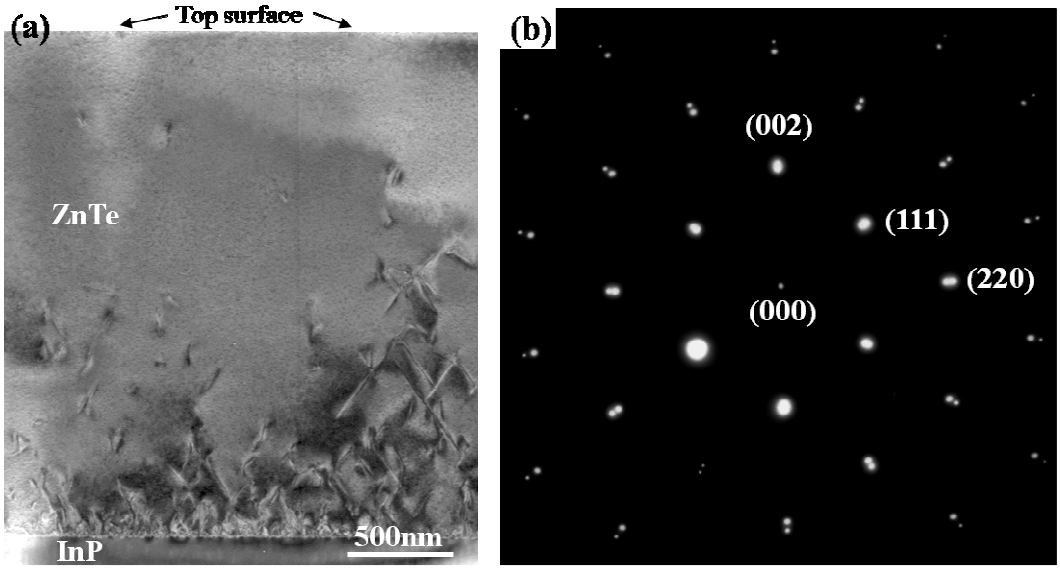

Fig. 3.4. (a) Low-magnification diffraction contrast image of ZnTe/InP heterostructure showing typical cross-section of the entire ZnTe epilayer; (b) SAED pattern from interface region of the ZnTe/InP sample showing well-defined and distinct ZnTe and InP diffraction patterns.

inspection to be perfect Lomer edge dislocations with Burgers vector of $\frac{1}{2}$ a<110> along the interface, and 60° dislocations with Burgers vector of the same length, but inclined with a 45° angle to the interface. These observations agree with previously reported results.[6,15] Figures 3.5 (b) and 3.5 (c) show enlarged images of the ZnTe/InP interface. The Burgers circuit drawn in Fig. 3.5 (b) indicates that this specific interfacial defect is a 60° dislocation, while the Burgers circuit drawn in Fig. 3.5 (c) corresponds to a Lomer edge dislocation.

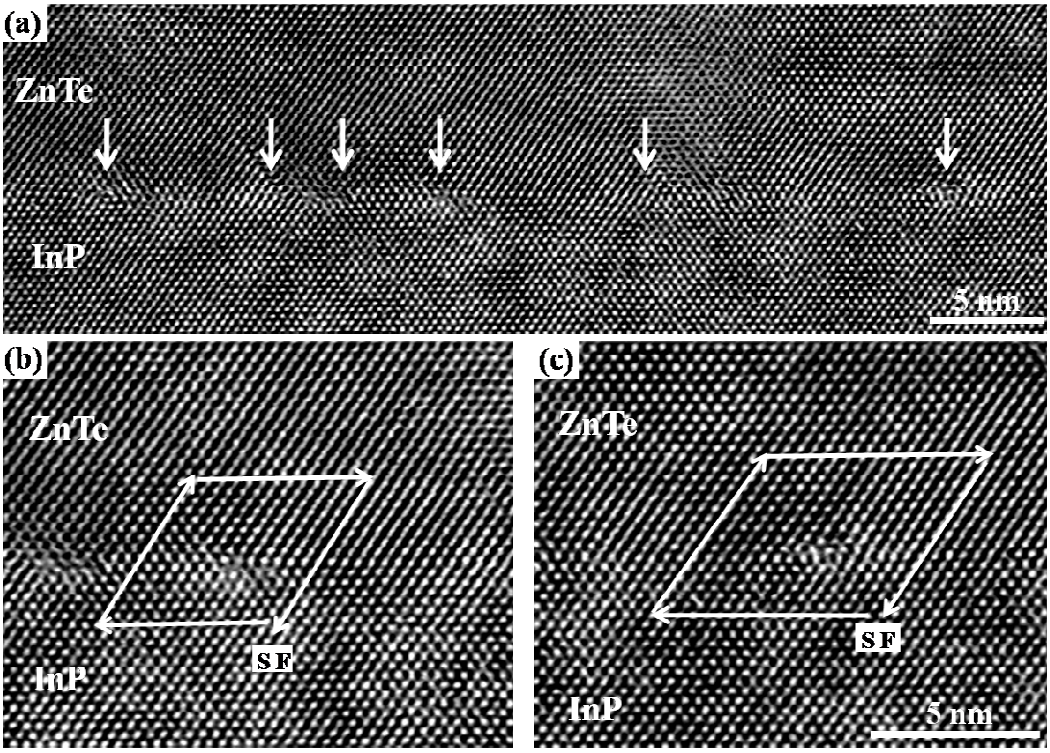

Fig. 3.5. (a) HREM image in {011}-type projection showing the ZnTe/InP interface; (b) (c) Enlarged views of the interface, with Burgers circuit analysis identifying 60° partial dislocation and Lomer edge dislocation. ***S*** and ***F*** stand for ***Start*** and ***Finish***, respectively.

In the case of the ZnTe epilayer grown on the GaAs substrate, a high density of misfit dislocations was again observed at the interface, as visible in the low magnification image shown in Fig. 3.6 (a). These defects can obviously be attributed to the large strain caused by the large ZnTe/GaAs lattice mismatch of ~7.38%. Moreover, further inspection of Fig. 3.6 (a) confirms that the density of dislocations again decreased greatly on moving away from the interface to the top surface, as observed previously for the ZnTe/InP sample. The flatness of the upper surface of the ZnTe epilayer can also be observed. SAED patterns from the interface region, as shown in Fig. 3.6 (b), demonstrate the difference of lattice constants between the ZnTe epilayer and the GaAs substrate, and also confirm the high quality growth of the ZnTe epilayer. HREM images of this sample again

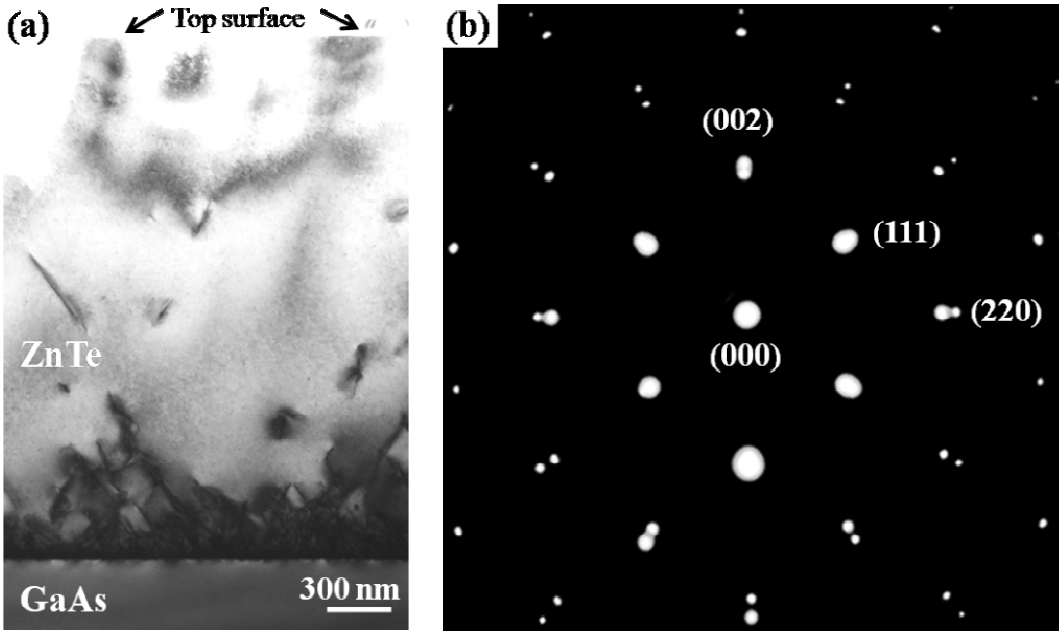

Fig. 3.6. (a) Low magnification image showing the entire ZnTe epilayer grown on GaAs (001) substrate; (b) SAED pattern taken from ZnTe/GaAs interface region.

revealed the presence of both Lomer edge dislocations and 60^{o} dislocations at the interface. Some regions with roughly periodic Lomer edge dislocations at the interface were observed, as shown by the example in Fig. 3.7 (a), while other regions had misfit dislocations that were more randomly spaced. Figure 3.7 (b) shows a magnified image of the ZnTe/GaAs interface with a Burgers circuit drawn around one of the dislocations, which in this case can be clearly identified as a perfect Lomer edge dislocation with a Burgers' vector of $\frac{1}{2}a$<110>.

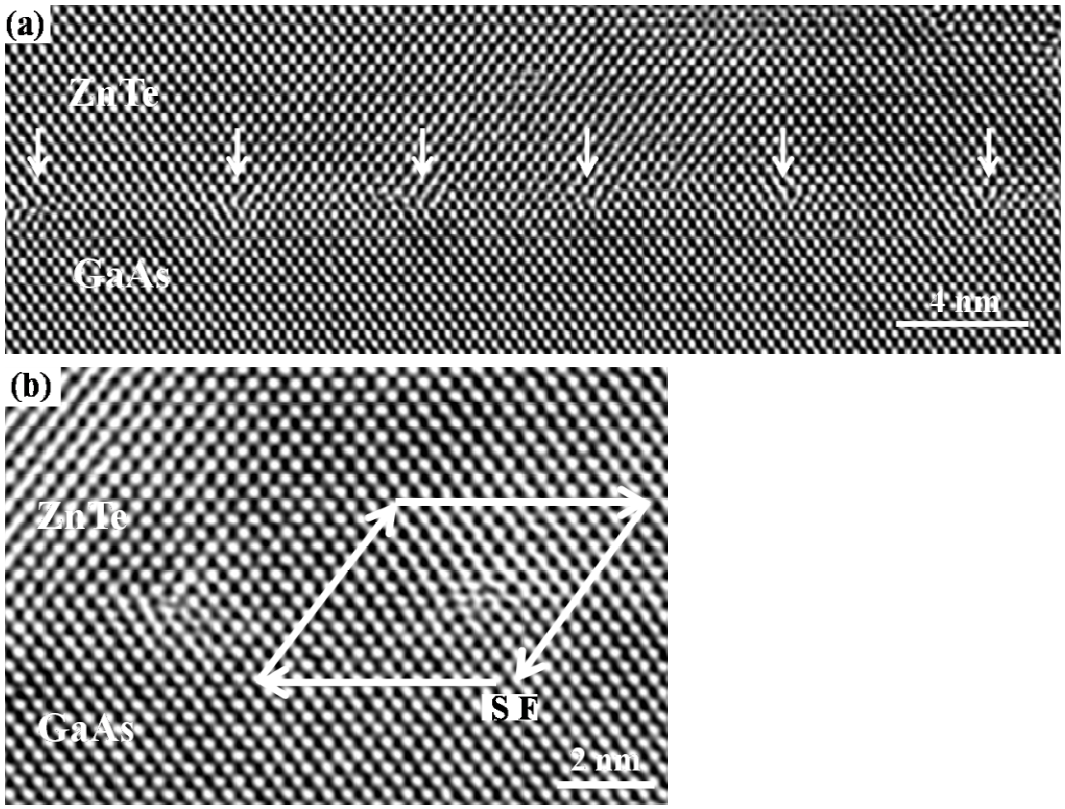

Fig. 3.7. (a) HREM image showing the region of ZnTe/GaAs interface with periodic Lomer edge dislocations. (b) Enlarged view of the interface region, with Burgers circuit analysis identifying Lomer edge dislocation.

3.3.2 Distribution of interfacial misfit dislocations

In order to gain more insight into relaxation of interfacial strain, a quantitative analysis of the distribution of misfit dislocations at the ZnTe/InP and ZnTe/GaAs heterointerfaces was carried out. Lattice images of the ZnTe/InP and ZnTe/GaAs samples were digitized and subjected to fast Fourier transform (FFT) processing. The FFT patterns were then appropriately filtered by selecting only specific {111} diffraction spots for the inverse FFT. These filtered images contained information about the location and type of the interfacial misfit dislocations.[6] A 60^{o} dislocation is identified when only one {111} plane terminates at the interface, whereas a Lomer edge dislocation is found when two corresponding {111} planes terminate at the same position. The procedure is demonstrated in Fig. 3.8 for both a Lomer dislocation and a 60^{o} dislocation. Figure 3.8 (b) shows the FFT pattern of Fig. 3.8 (a) that is part of the digitized lattice image of the ZnTe/GaAs interface. If only the {111} diffraction spots marked by the circles are selected for the inverse FFT, Figure 3.8(c) is obtained; and Figure 3.8 (d) is obtained by selecting only diffraction spots marked by the squares. The left dislocation is a Lomer dislocation because two corresponding {111} planes, indicated by the dashed lines in Fig 3.8 (c) and Fig. 3.8 (d), terminate at the same position. The right dislocation is a 60^{o} dislocation since only one {111} plane terminates at that position, as shown in Fig. 3.8 (d).

Using this identification method, the distribution of interfacial misfit dislocations could be quantified, and the types of defects at the interfaces could also be identified. For the specific region of the ZnTe/InP sample shown in

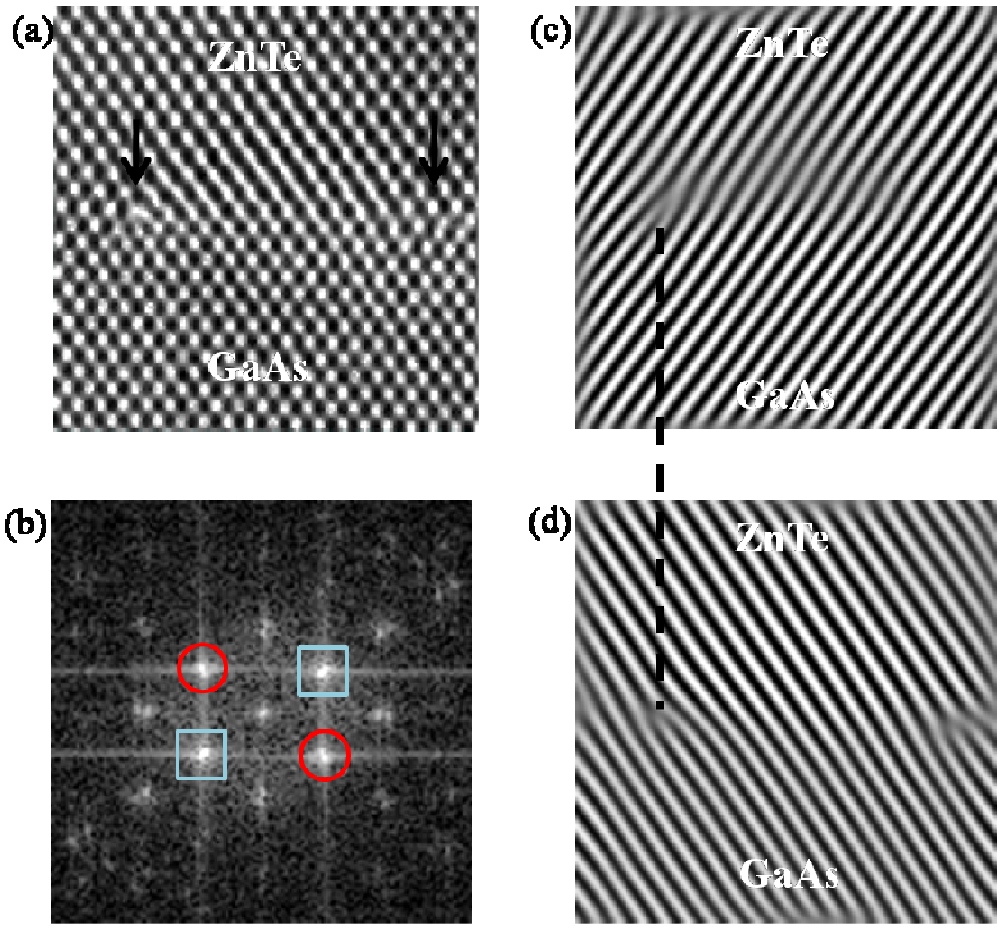

Fig. 3.8. (a) Part of the digitized lattice image of the ZnTe/GaAs interface, with a Lomer dislocation at left and a 60º dislocation at right (both arrowed); (b) FFT pattern of image (a); (c) Inverse FFT image obtained by selecting {111} diffraction spots marked by circles; (d) Inverse FFT image obtained by selecting {111} diffraction spots marked by squares.

Fig. 3.9, the inverse FFT analysis identified four 60^o dislocations and one Lomer edge dislocation at the interface. In the case of the ZnTe/GaAs sample, regions having Lomer edge dislocations, and regions with more randomly spaced misfit dislocations, were identified from the inverse FFT images, in accordance with the TEM observations. Figure 3.10 shows four Lomer edge dislocations and two closely separated 60^o dislocations at the ZnTe/GaAs interface. Since {100} planes are not easy slip planes for materials with zincblende structure, in comparison with glide on {111} planes**,** the 60^o dislocations are created more easily than Lomer dislocations.[16] After analysis of the defects present along 0.34 µm of the ZnTe/InP interface and along 0.36 µm of the ZnTe/GaAs interface, it was discovered that the number of 60^o dislocations was considerably larger than the number of Lomer dislocations in both systems. The ratio of Lomer dislocations to the total number of dislocations for the ZnTe/InP and ZnTe/GaAs samples was determined to be about 13% and 39%, respectively.

The magnitude of the residual interface strain present after relaxation can be estimated from the distribution and the type of misfit dislocations. The lattice mismatch between various substrates and the ZnTe epilayers has been defined in eq. (1), and the biaxial compressive strain field in the ZnTe epilayer is given by:

$$\varepsilon_{\parallel} = (a_{\parallel} - a_0) / a_0 , \qquad (2)$$

where a_0 and $a_{\parallel}$ are the unstrained, and strained, lattice constants, respectively.[6] In the case of a pseudomorphic strained layer, $\varepsilon_{\parallel}$ would be equivalent to f. When an array of misfit dislocations is created, the elastic strain is reduced by

$$\delta = \boldsymbol{b} \cdot \hat{\boldsymbol{e}} \langle 110 \rangle / d , \qquad (3)$$

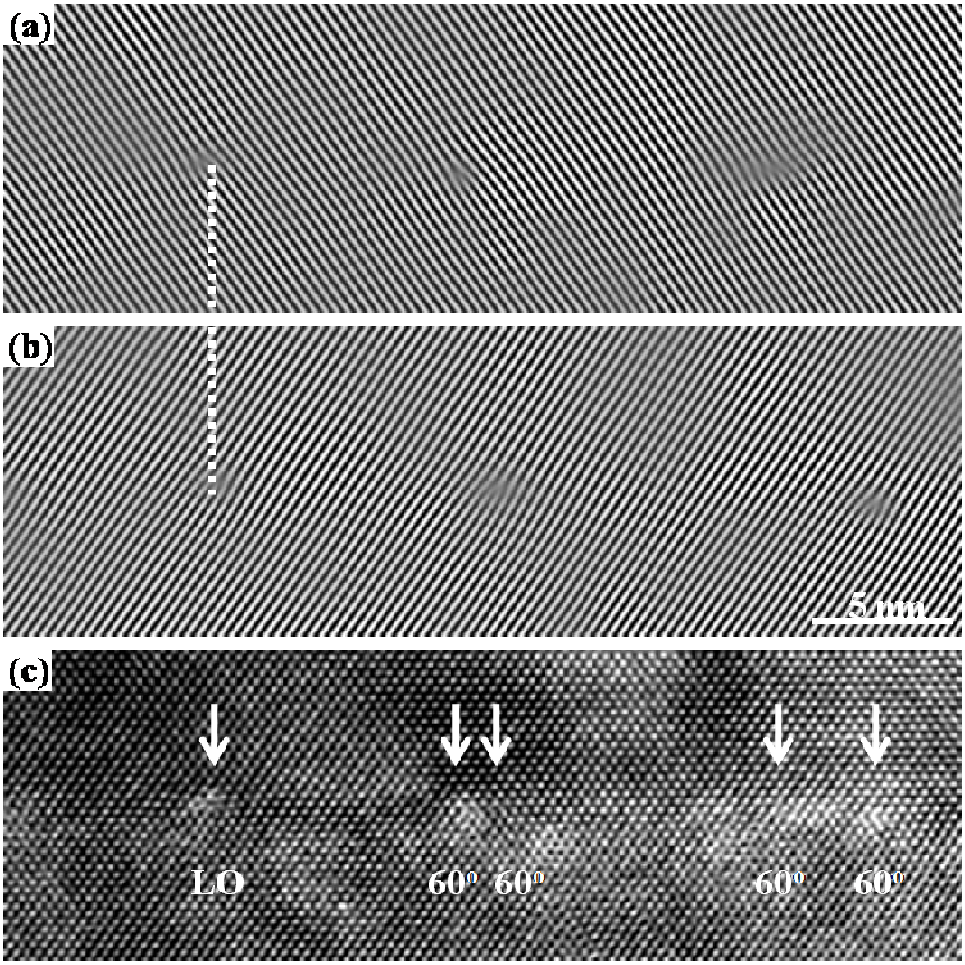

Fig. 3.9. (a) (b) Inverse FFT images for ZnTe/InP sample showing specific {111} crystalline planes; (c) Corresponding high-resolution image identifying dislocation type, where ***LO*** and ***60°*** stand for Lomer edge dislocation and 60° dislocation, respectively.

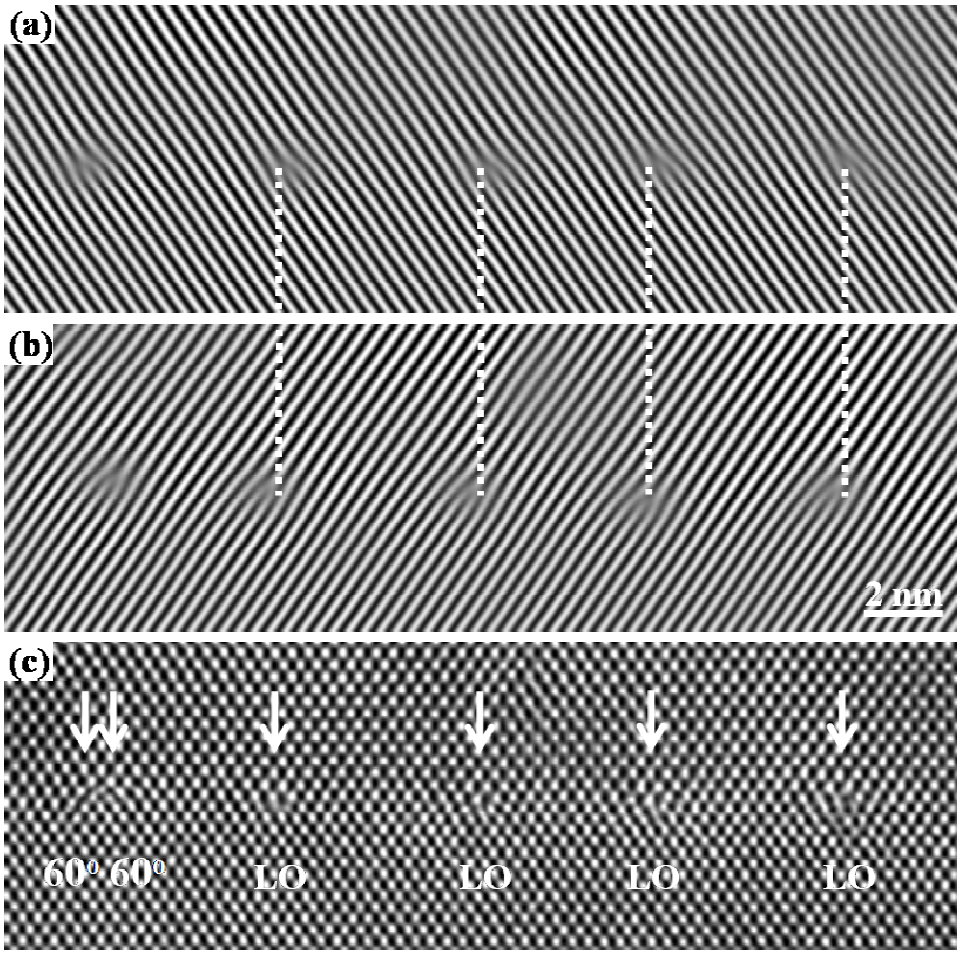

Fig. 3.10. (a) (b) Inverse FFT images for ZnTe/GaAs sample showing specific {111} crystalline planes; (c) Corresponding high-resolution image identifying dislocation type, where ***LO*** and ***60°*** stand for Lomer edge dislocation and 60° dislocation, respectively.

where $\boldsymbol{b}$ is the Burgers vector of the misfit dislocation, $\hat{e}$ <110> is the unit vector along the <110> direction, and d is the average separation between the misfit dislocations.[17,18] The length of the Burgers vector for a perfect Lomer edge dislocation is $\frac{1}{2}\, a_s$ <110>, which is 4.1503 Å for the InP substrate and 3.9981 Å for the GaAs substrate. In the case of a 60° dislocation, the interface component of the Burgers vector has a length of $\frac{1}{2}\,|\boldsymbol{b}|$, which incidentally explains why Lomer dislocations are twice as efficient as 60° dislocations in strain relaxation.[6] The remaining lattice strain can then be defined by

$$\varepsilon_r = \varepsilon_{\parallel} + \delta\,, \tag{4}$$

By regarding a Lomer dislocation as two 60° dislocations with different edge components, the average separation d_{ave} between all 60° dislocations having equal edge components can be obtained from the FFT filtered images. The residual strain at the interface can then be estimated.

The interfaces would theoretically be completely relaxed at average Lomer dislocation separations of 107.8 Å for the ZnTe/InP sample, and 54.2 Å for the ZnTe/GaAs sample. After counting the number of dislocations and completing analysis of the dislocation types along 0.34-µm of the ZnTe/InP interface, and along 0.36-µm of the ZnTe/GaAs interface region, the average separation between dislocations was determined to be 107.6 Å with a standard deviation of 47.8 Å for the ZnTe/InP sample, and 54.8 Å with a standard deviation of 9.2 Å for the ZnTe/GaAs sample. Figure 3.11 shows the distribution of separations of dislocations with equal edge components at the ZnTe/InP interface and at the

ZnTe/GaAs interface. It is significant that the standard deviation for the ZnTe/InP sample is much greater than that for the ZnTe/GaAs sample, which can perhaps be attributed to the fact that the ZnTe/InP sample did not have an InP buffer layer before ZnTe growth.

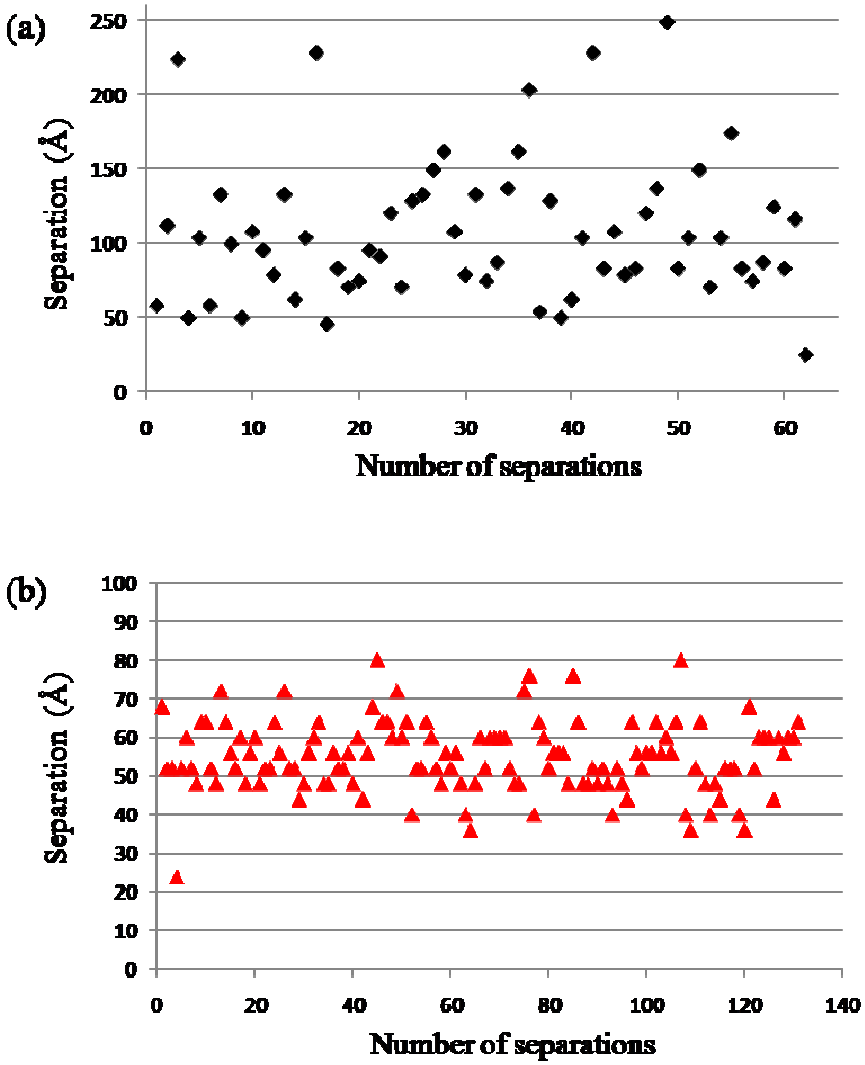

Fig. 3.11. Distribution of separations of dislocations with equal edge components for: (a) ZnTe/InP sample; and (b) ZnTe/GaAs sample.

Based on these numbers, the residual interfacial strain can then be estimated to be about 0.01% for the ZnTe/InP sample and -0.09% for the ZnTe/GaAs sample. Thus, it appears that the interfaces of these two samples can be considered as being fully relaxed, which was confirmed by the lattice constants of ZnTe in the layer plane ($a_{\parallel}$) calculated from high-resolution XRD results.[12] However, it is noteworthy that the high-resolution XRD studies also suggested that some residual tensile strains were present, since the lattice constants along the growth direction ($a_{\perp}$) of all ZnTe epilayers were smaller than that of bulk ZnTe at room temperature. This is presumably caused by the difference in thermal expansion coefficients between the epilayers and the various substrates. ZnTe has a larger thermal expansion coefficient than any of the substrate materials, and thus the thermal shrinkage of the ZnTe epilayers is greater than that of the substrates when cooling down to room temperature after growth.

3.3.3 PL measurements

PL measurements were carried out to study the optical properties of ZnTe grown on the various III-V substrates.[12] Figure 3.12 shows the PL spectra of all samples measured at 300 K. The PL peaks are at 2.26 eV for all samples, and the PL emission from ZnTe epilayer grown on GaSb has the strongest intensity. This could be attributed to the minimal defect density in the epilayer due to the smallest lattice mismatch between ZnTe and GaSb, as confirmed by the TEM results. The sample of ZnTe grown on InAs shows much stronger PL intensity than that of the other two samples: ZnTe/GaAs and ZnTe/InP, which have larger

lattice mismatch. Temperature-dependent PL spectra of ZnTe grown on GaAs (001) substrate are shown in Fig. 3.12 (b). As temperature increases, the PL peak shows red-shift due to decrease in the band-gap energy, and the FWHM of the PL spectrum becomes broader as expected. In addition, a broad PL emission below the band-gap energy was observed at 80K, which is possibly due to defect-related optical transitions.

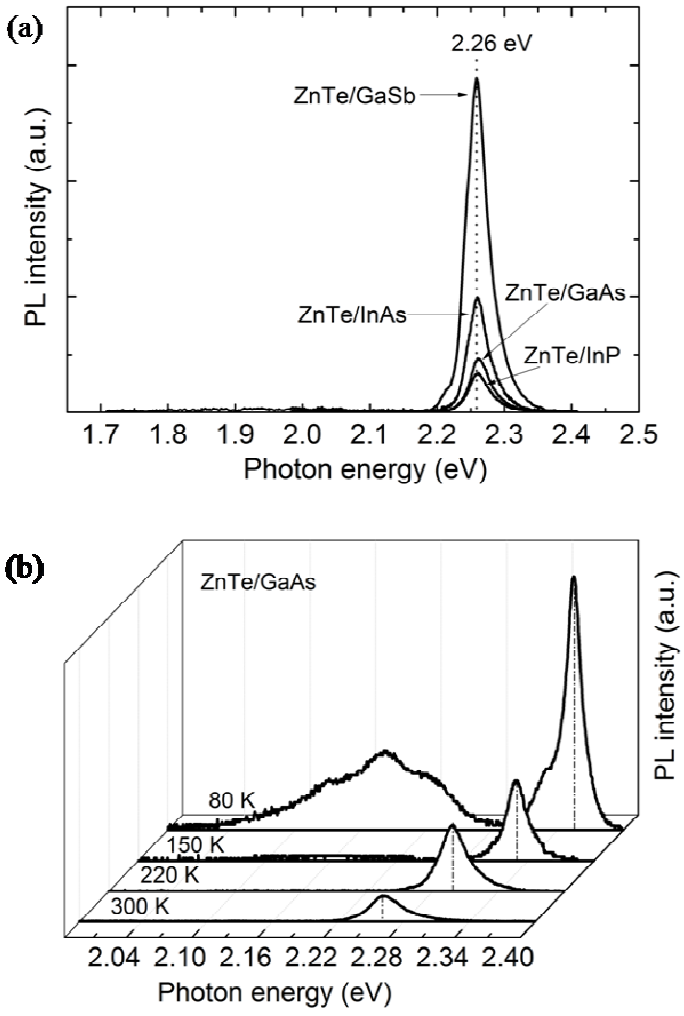

Fig. 3.12. (a) PL spectra of ZnTe epilayer grown on various III-V substrates; (b) Temperature-dependent PL spectra of ZnTe/GaAs sample.[12]

3.4 Conclusion

The structural properties of thick ZnTe epilayers grown by MBE on four different III-V (100) substrates have been investigated using electron microscopy. The densities of growth defects dropped off rapidly with distance from the interfaces in all cases. The ZnTe/GaSb and ZnTe/InAs samples, which have relatively small lattice mismatch, revealed highly coherent interfaces with very low defect density, and the virtual absence of any interfacial misfit dislocations over large distances. Lomer edge dislocations, which are the most efficient mechanism to relax epitaxial strain, were identified at the ZnTe/InP and ZnTe/GaAs interfaces. Using digital image filtering, the distribution of interfacial misfit dislocations was determined: the fraction of perfect Lomer edge dislocations was ~13% for the ZnTe/InP sample and ~39% for the ZnTe/GaAs sample. The residual strain was estimated from the average separation of equivalent {111} planes terminating at the interface, and found to be 0.01% for the ZnTe/InP sample and -0.09% for the ZnTe/GaAs sample. Strong PL spectra for all the ZnTe samples were observed from 80 to 300 K. The PL peak positions of the ZnTe epilayers are at 2.26 eV at room temperature.

REFERENCES

[1]L. Ouyang, J. Fan, S. Wang, X. Lu, Y.-H. Zhang, X. Liu, J. K. Furdyna, and D. J. Smith, J. Cryst. Growth **330**, 30 (2011).

[2]Y.-H. Zhang, S. -Q. Yu, S. R. Johnson, D. Ding, S. -N. Wu, Proceedings of the 33rd IEEE Photovoltaic, Energy Specialist Conference, p. 20, 2008.

[3]S. Wang, S. -N. Wu, D. Ding, X. Liu, X. - B. Zhang, D. J. Smith, S.- Q. Yu, S. R. Johnson, J. K. Furdyna, and Y.- H. Zhang, J. Cryst. Growth **311**, 2116 (2009).

[4]S. Kamuro, C. Hamaguchi, M. Fukushima, and J. Nakai, Solid State Electron **14**, 1183(1971).

[5]Y. Rajakarunanayake, B. H. Cole, J. O. McCaldin, D. H. Chow, J. R. Soderstrom, T. C. McGill and C. M. Jones, Appl. Phys. Lett. **55**, 1217 (1989).

[6]S. Bauer, A. Rosenauer, J. Skorsetz, W. Kuhn, H. P. Wagner, J. Zweck, and W. Gebhardt, J. Cryst. Growth **117**, 297 (1992).

[7]S. Bauer, A. Rosenauer, P. Link, W. Kuhn, J. Zweck and W. Gebhardt, Ultramicroscopy **51**, 221 (1993).

[8]T. W. Kim, D. U. Lee, H. S. Lee, J. Y. Lee, H. L. Park, Appl. Phys. Lett. **78**, 1409 (2001).

[9]B. J. Kim, J. F. Wang, Y. Ishikawa, Y.-G. Park, D. Sindo, S. Abe, K. Masumoto and M. Isshiki, J. Cryst. Growth **235**, 201 (2002).

[10]M. Strassburg, M. Strassburg, O. Schulz, U. W. Pohl, A. Hoffmann, D. Bimberg, A.G. Kontos, Y. S. Raptis, J. Cryst. Growth **248**, 50 (2003).

[11]X. Zhang, S. Wang, D. Ding, X.Liu, J. - H. Tan, J. K. Furdyna, Y. - H. Zhang, and D. J. Smith, J. Electron. Mater. **38**, 1558 (2009).

[12]J. Fan, L. Ouyang, X. Liu, D.Ding, J. K. Furdyna, D. J. Smith, and Y.-H. Zhang, J. Cryst. Growth **323**, 127 (2011).

[13]C. Z. Wang, D. J. Smith, S. Tobin, T. Parodos, J. Zhao, Y. Chang and S. Sivananthan, J. Vac. Sci. Technol. A **24**, 995 (2006).

[14]J. K. Furdyna and J. Kossut, Superlattices and Microstructures **2**, 89 (1986).

[15]P. M. J. Maree, J. C. Barbour, J. F. van der Veen, K. L. Kavanagh, C. W. T. Bulle-Lieuwma and M. P. A. Viegers, J. Appl. Phys. **62**, 4413 (1987).

[16]N. Otsuka, C. Choi, L. A. Kolodziejski, R. L. Gunshor, R.Fischer, C. K. Peng, H. Morkoc, Y. Nakamura and S. Nagakura, J. Vac. Sci. Technol. B **4**, 896 (1986).

[17]J. W. Matthews, J. Vac. Sci. Technol. **12**, 126 (1975).

[18]A. F. Schwartzman and and R. Sinclair, J. Electron. Mater. **20**, 805 (1991).

Chapter 4

STRUCTURAL CHARACTERIZATION OF GaSb EPILAYERS GROWN ON ZnTe VIRTUAL SUBSTRATES WITH A TEMPERATURE RAMP DURING GROWTH

This chapter describes the structural characterization of GaSb epilayers grown on ZnTe virtual substrates by molecular beam epitaxy (MBE) using a temperature ramp during growth. This study was carried out in collaboration with Prof. Y.-H. Zhang and colleagues at Arizona State University, and Prof. J. K. Furdyna and Dr. X. Liu at University of Notre Dame. X-ray diffraction (XRD) and photoluminescence (PL) measurements were performed by Jin Fan at Arizona State University. My contribution to this work has been the microstructural characterization using electron microscopy. Major results of this study have been published elsewhere.[1]

4.1 Introduction

A multijunction solar-cell design based on the monolithic integration of II-VI (MgZnCd) (SeTe) and III-V (AlGaIn)(AsSb) compound semiconductors grown on the so-called 6.1-Å substrates, such as GaSb and ZnTe, has been proposed, providing band-gap energies spanning a broad range of the solar spectrum.[2,3] Due to the high cost and limited size of commercial GaSb and ZnTe substrates, thick ZnTe epilayers grown on conventional III-V substrates, such as GaAs and Si, have been proposed and successfully demonstrated as virtual

substrates.[4-6] The realization of the growth of high-quality GaSb on ZnTe virtual substrates should then enable the monolithic integration of other lattice-matched 6.1-Å semiconductors on large-area and low-cost conventional GaAs and Si substrates for optoelectronic devices. Improved crystalline quality of GaSb grown on GaAs (001) substrates using ZnTe buffer layers has recently been reported,[7,8] such as reduced dislocation density and residual strain in the GaSb film by XRD measurements and Hall mobility measurements, and smooth surface morphology by atomic force microscopy.

In this current study, a temperature ramp during the growth of GaSb on ZnTe has been used in an attempt to further improve material quality. The temperature commonly used for the growth of GaSb (470 ˚C), is considerably higher than that used for growth of ZnTe (320 ˚C). The surface of ZnTe layer is likely to be severely degraded when the growth of GaSb on ZnTe is initiated at such a high temperature. The growth of a thin GaSb transition layer using a temperature ramp before deposition of the remaining GaSb epilayer at the normal growth temperature could possibly overcome this problem. Thus, a set of samples was grown on ZnTe/GaSb (001) substrates under different growth conditions using MBE. High-resolution XRD measurements were performed to determine the structural quality of the GaSb epilayers, and PL was applied to determine the optical properties. Transmission electron microscopy (TEM) was used to study the surface morphology of the GaSb epilayers and to characterize misfit dislocations at the GaSb/ZnTe interfaces.

4.2 Experimental details

The epitaxial growth was carried out using a Riber 32 MBE system consisting of two separate III-V and II-VI chambers, which were connected via an ultrahigh-vacuum transfer module. The ZnTe epilayers were first grown on GaSb (001) substrates, as described in chapter 3. After ZnTe growth in the II-VI chamber, the wafers were transferred to the III-V chamber for the GaSb growth. Growth of a thin GaSb transition layer (~50 nm) under a temperature ramp was then carried out before the remaining GaSb epilayer was deposited at the normal growth temperature of ~ 470 ºC. During growth, the beam equivalent pressure (BEP) ratios of Ga to Sb were adjusted by monitoring the surface reconstructions observed using reflection-high-energy electron diffraction (RHEED). The parameters used for growth of the GaSb layers of these samples are summarized in Table 1, and Fig. 4.1 shows a schematic of the sample structures. As indicated in Fig. 4.1, another thin ZnTe epilayer was grown at 320 ºC on top of the GaSb layer for Sample D, for further investigation of the influence of temperature ramps on the overall material quality.

The cross-sectional and plan-view TEM samples were prepared using mechanical polishing and dimpling followed by Argon ion milling. A liquid-nitrogen-temperature cooling stage and low-energy (2.5 - 3 keV) ion beams were used to minimize any ion milling damage.[9] Electron micrographs were recorded using a JEM-4000EX TEM operated at 400 keV with a structural resolution of ~1.7 Å. The high-resolution XRD ω-2θ scans were performed using a PANalytical X'Pert PRO MRD X-ray diffractometer with multi-crystal

Table 4.1. Summary of growth parameters for the growth of GaSb epilayer on ZnTe virtual substrates.

Sample	Growth rate (μm/hr)	Temperature ramp	Ramping rate (ºC/min)	Ga/Sb BEP ratio
A (110131A)	0.8	380 – 470 ºC	27	1:5
B (110408B)	0.8	360 – 470 ºC	33	1:5
C (110523A)	0.8	320 – 470 ºC	45	1:5
D (110718B)	0.8	360 – 470 ºC	28	1:5

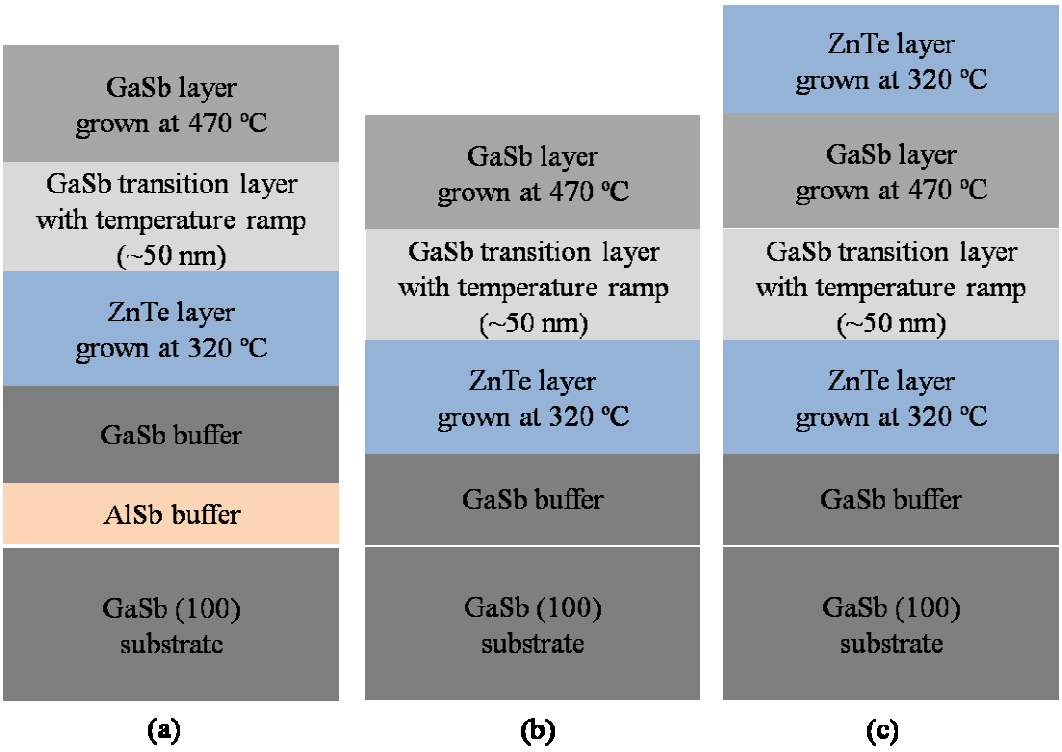

Fig. 4.1. Schematic illustration of the epitaxial layer structure for: (a) Sample A; (b) Samples B and C; and (c) Sample D.

monochromator. The $K_{\alpha 1}$ line of copper (1.54 Å) was used as the incident beam. For characterization of optical properties, PL measurements were carried out using the 780-nm line of a laser diode for excitation. A Fourier transform infrared (FTIR) spectrometer configured with a quartz beam-splitter and liquid-nitrogen-cooled InSb detector was used for detection.

4.3 Results and discussion

4.3.1 XRD measurements

The high-resolution XRD measurements were performed in the vicinity of the (004) diffraction peak of the GaSb substrate. The XRD patterns for Samples A and B, displayed in Fig. 4.2, show clear diffraction peaks from the ZnTe epilayer, the top GaSb epilayer and the GaSb substrate. Simulated ω-2θ curves, also included in Fig. 4.2 below each measurement, show good agreement with the experimental data. It is apparent that the diffraction peak of the top GaSb epilayer is on the right side of the GaSb substrate peak, which indicates that the vertical lattice parameter ($a_{\perp}$) of the GaSb epilayer is smaller than that of the GaSb substrate. The simulation results indicate that the ZnTe epilayer is partially relaxed, and the GaSb epilayer is thus subjected to tensile strain leading to the smaller vertical lattice constant. For Sample B, the simulated ω-2θ curve shows that the diffraction fringes are a combination of Pendellösung thickness fringes from both GaSb and ZnTe epilayers, indicating the high quality of the GaSb and ZnTe single-crystal epitaxial layers with smooth interfaces, uniform thicknesses, and low defect densities.

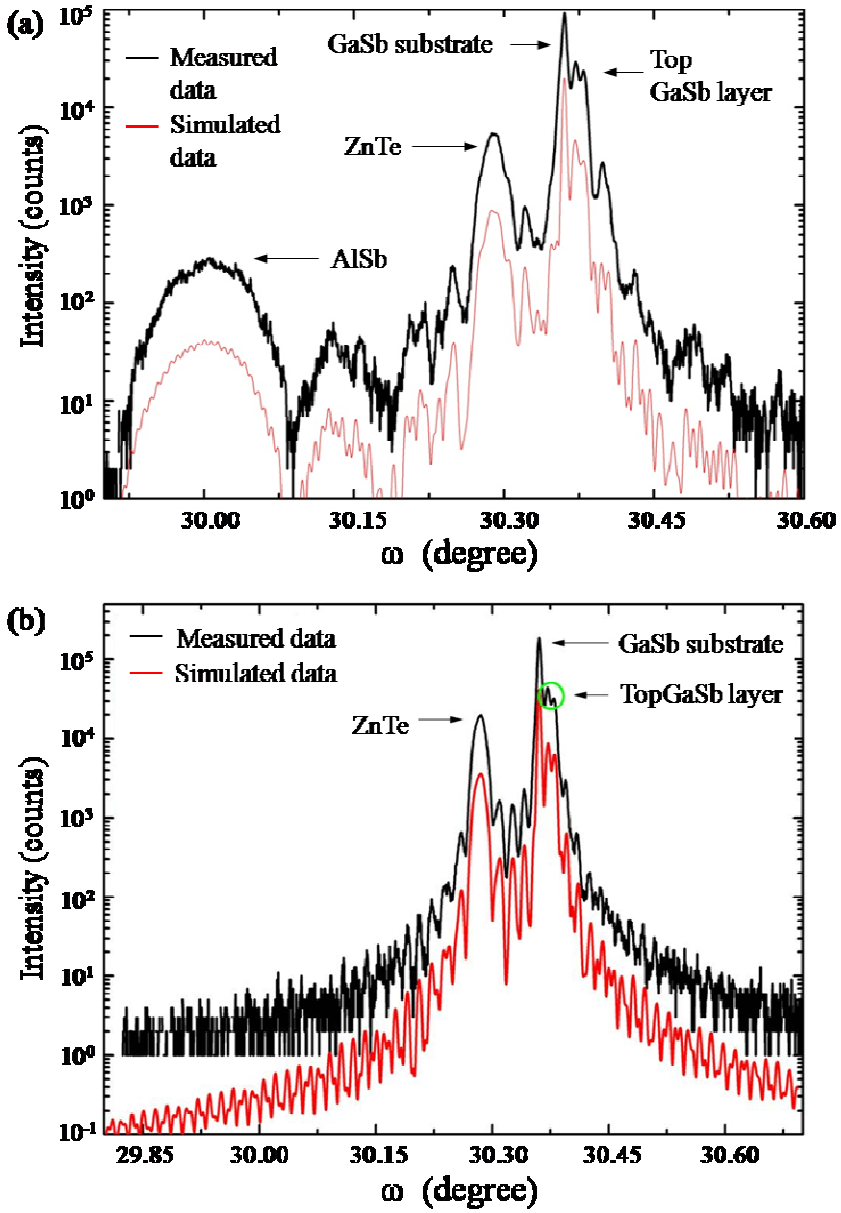

Fig. 4.2. XRD ω-2θ curves measured in the vicinity of the (004) diffraction peak of GaSb substrate for: (a) Sample A and (b) Sample B.[1]

4.3.2 TEM characterization

Cross-sectional TEM has been extensively used to investigate the interface morphology and to identify interfacial misfit dislocations. Low-magnification TEM images of Samples A, B and C, as shown in Fig. 4.3, demonstrate smooth morphology for both ZnTe-on-GaSb and GaSb-on-ZnTe interfaces, and excellent crystallinity for both ZnTe and GaSb epilayers. No misfit dislocations were observed over large lateral distance for all three samples at either the ZnTe/GaSb or the GaSb/ZnTe interfaces, which confirmed the very low defect density in the epilayers. An AlSb buffer layer was grown on the GaSb substrate for Sample A before the GaSb buffer layer was grown, as previously indicated by the XRD pattern in Fig. 4.2 (a). For Samples B and C, the structures are identical, with GaSb buffer layers grown on an GaSb substrate followed by ZnTe and GaSb epilayers. The interface between GaSb buffer layers and the substrate is barely visible. The thicknesses of the GaSb and ZnTe layers were directly measured from the TEM images, and were in close agreement with XRD measurements. For Sample B, the GaSb and ZnTe layers were 380 nm and 300 nm thick, respectively. For Sample C, the GaSb and ZnTe layers were 280 nm and 390 nm thick, respectively.

Plan-view TEM images were also used to determine the defect density in the top GaSb epilayer. As shown in Fig. 4.4, threading dislocations with an estimated defect density of ~ $1x10^7/cm^2$ were observed in the top GaSb layers of Sample C. Figure 4.5 shows Lomer edge dislocations at the ZnTe/GaSb interface. Lomer dislocations were observed previously for ZnTe/GaAs and ZnTe/InP

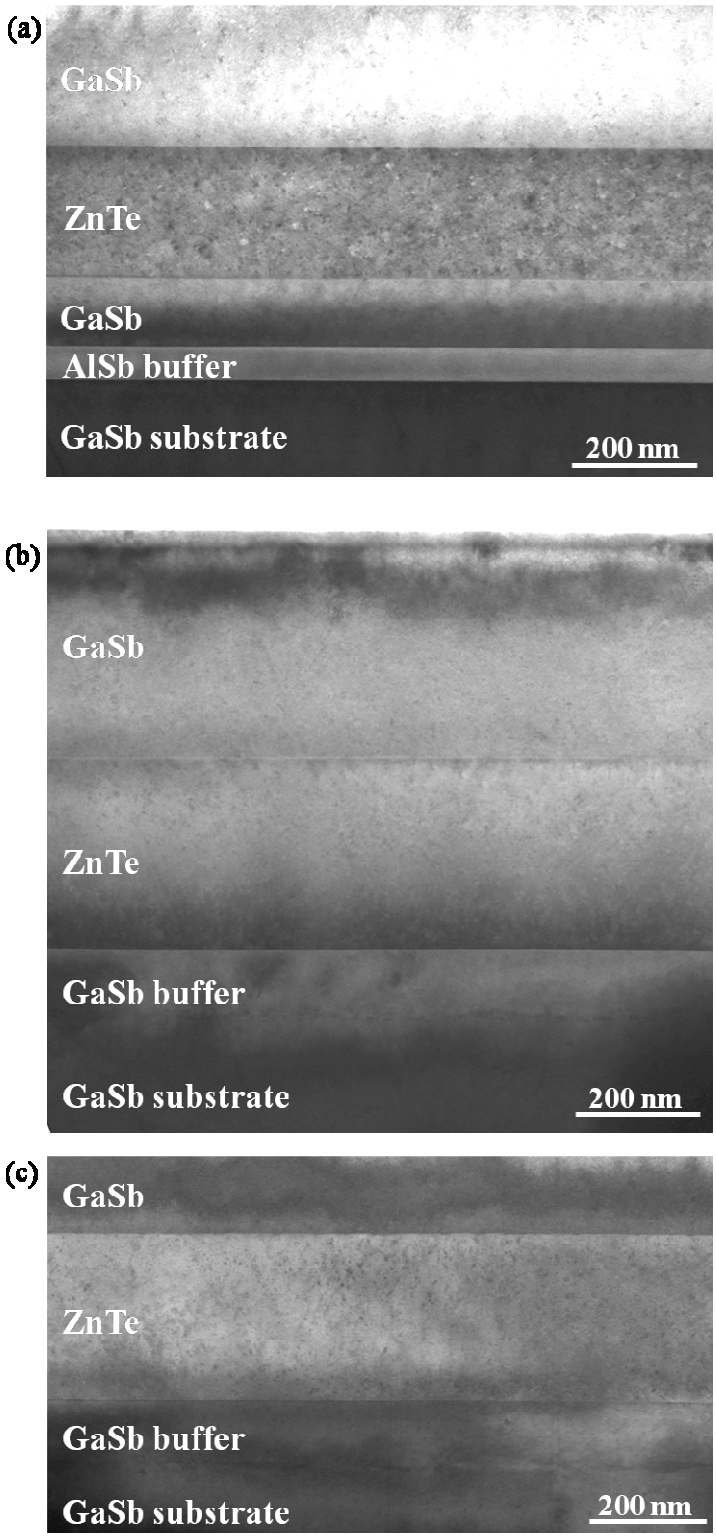

Fig. 4.3. Low-magnification XTEM images showing interfaces for: (a) Sample A; (b) Sample B; and (c) Sample C.

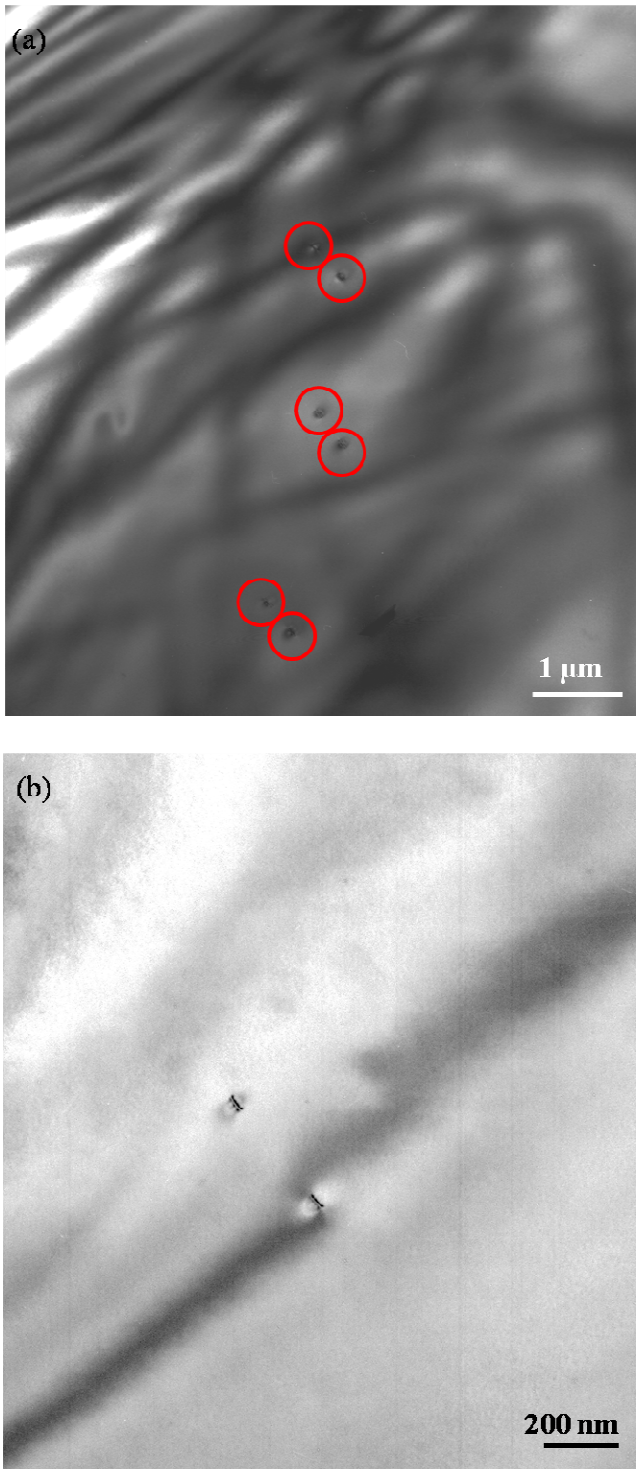

Fig. 4.4. (a) Plan-view TEM image of Sample C showing the presence of threading defects (circled) in the top GaSb layer; (b) Enlarged view of the threading defects.

interfaces, as discussed in chapter 3. The Lomer dislocations at the ZnTe/GaSb interface of Sample C, as shown in Fig. 4.5, are very well separated, which is attributed to the small lattice mismatch (-0.13%) between the two materials, and because the ZnTe layer is just partially relaxed.

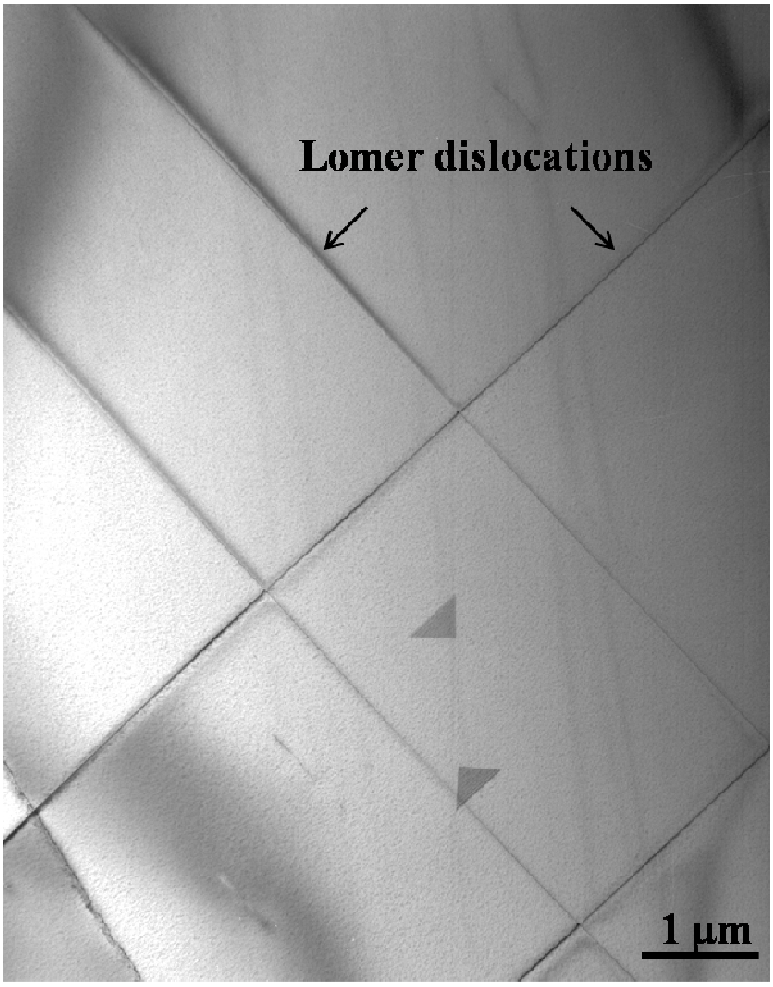

Fig. 4.5. Plan-view TEM image of Sample C showing the presence of well-separated Lomer edge dislocations at the ZnTe/GaSb interface.

In the case of Sample D, low magnification images, such as shown in Fig. 4.6 (a), revealed occasional interfacial misfit dislocations at the interface of the thick ZnTe epilayer (~1.2 µm) grown on the GaSb substrate and at the interface of the GaSb epilayer grown on ZnTe. The thickness of the upper ZnTe layer was measured to be ~140 nm, and it was ~110 nm for the GaSb epilayer. Some strain-related contrast was also apparent at those interfaces. It is clear that there are considerably more dislocations at the ZnTe/GaSb-buffer interface than at the GaSb/ZnTe interface. The average separation between misfit dislocations is on the order of many micrometers at the GaSb/ZnTe interface, while it is about a few hundred nanometers at the ZnTe/GaSb-buffer interface. Compared to Samples A, B and C, where no misfit dislocation were observed over large distances at the ZnTe/GaSb-buffer interfaces, Sample D has a much thicker ZnTe epilayer (~1.2 µm) grown on the GaSb buffer layer. Due to the small lattice mismatch between ZnTe and GaSb (~0.13%), the critical thickness value is expected to be large but below about 0.8 µm.[10] The ZnTe epilayer grown on the GaSb buffer of Sample D is well above this critical thickness, whereas the ZnTe epilayer is well below this critical thickness for Samples A, B and C, which would explain the differences in the appearance of interfacial misfit dislocations. Figure 4.6 (b) shows an enlarged view of the upper ZnTe/GaSb and GaSb/ZnTe interfaces of Sample D. No misfit dislocations are visible at the top ZnTe/GaSb interface, comfirming the excellent crystallinity and the very low defect density expected for this relatively thin (~140 nm) ZnTe epilayer.

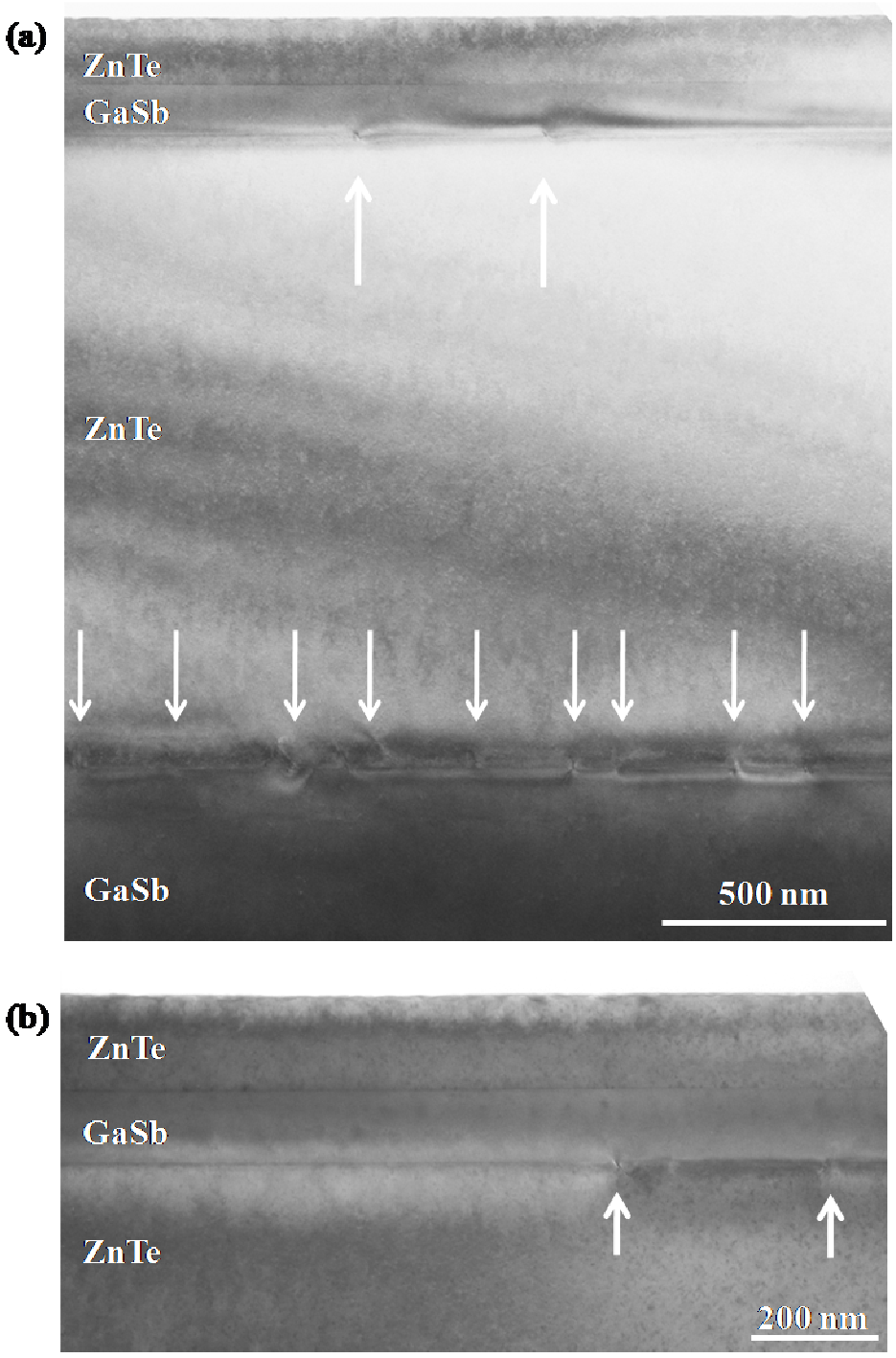

Fig. 4.6. (a) Cross-section electron micrograph showing the interfaces of Sample D; (b) Enlarged view showing misfit dislocations (arrowed) present at the GaSb/ZnTe interface.

4.3.3 PL measurements

The PL measurements were carried out to investigate the optical properties of the GaSb epilayers. The PL spectra of samples A, B and C, which are measured at 13 K, are shown in Fig. 4.7 (a)–(c). Low-temperature PL of GaSb has been well studied by many authors.[11-14] Three main PL lines have been often observed and discussed: i) A PL line with maximum at 796 meV, which is considered as an emission of an exciton bound to a non-specified neutral acceptor;[13] ii) A PL line with maximum at 777 meV, denoted as the "A" line, which is ascribed to recombination at a native acceptor level (A) via Band-Acceptor or Donor-Acceptor Pair transitions;[12] iii) A PL line with maximum around 758 meV, denoted as the "B" line, which is interpreted as a transition from another acceptor level (B).[12]

A broad emission peak is observed for Sample A in the range of 570-780 meV, which is ascribed to optical transitions from acceptors and other growth-related defects. Within this range, emission peaks are visible at around 777 and 758 meV, with intensities as strong as that from the bound exciton. For Sample B, which contains the GaSb transition layer grown under T_{ramp} = 360 – 470 ˚C, the PL spectrum shows a narrow peak from the bound exciton at 793 meV, with full width at half maximum (FWHM) of 15 meV. Similarly, a broad emission is observed between 650 meV and the bound exciton peak, which is attributed to emissions which have the same origins as for Sample A. Moreover, it is noteworthy that this emission is greatly depressed in intensity and energy range (650 -780 meV), which suggests a large decrease in the density of impurities and

defects. For Sample C, the main PL feature is in the range of 570 – 850 meV. The emission from the bound exciton is not well resolved.

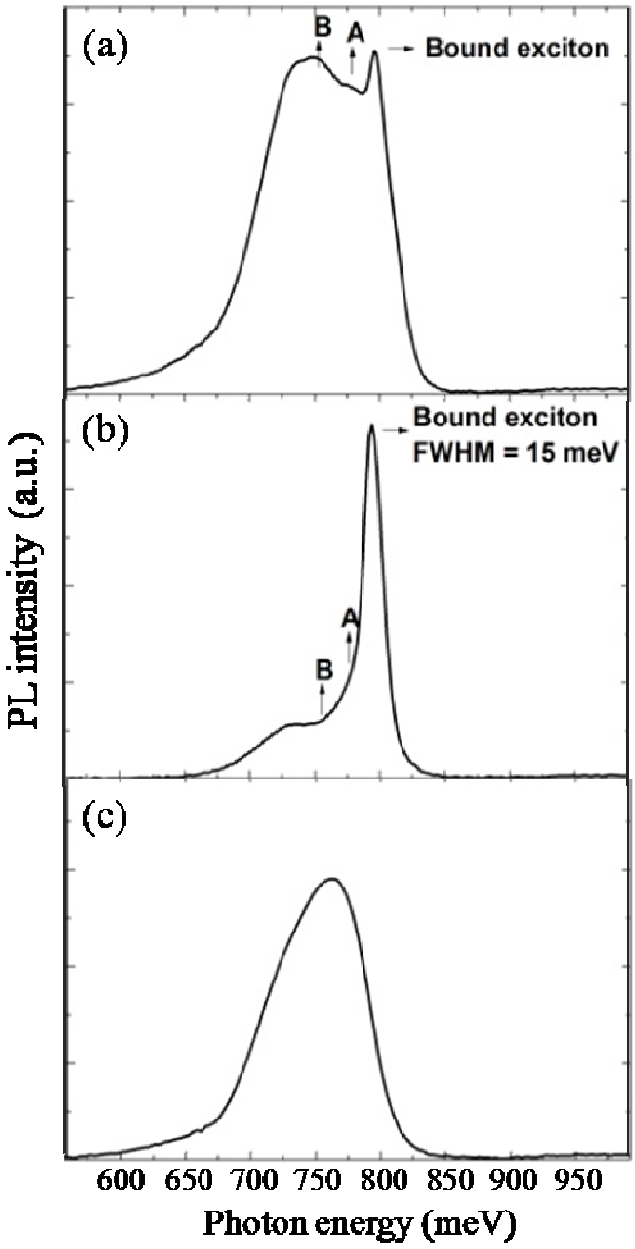

Fig. 4.7. PL spectra measured at 13 K for: (a) Sample A; (b) Sample B; and (c) Sample C.

From careful comparison among Samples A, B and C, it is apparent that different temperature ramps during growth affect optical properties differently. When the starting point of the temperature ramp is close to the ZnTe growth temperature (320 ºC), the GaSb/ZnTe interface is expected to be less damaged while the optical properties of GaSb will be more deteriorated due to defects generated during the low-temperature growth. On the other hand, when the starting point of the temperature range is close to the GaSb growth temperature (480 ºC), the ZnTe surface would be more damaged during the initial GaSb growth so that the optical properties of GaSb are adversely affected due to the interfacial defects. Thus, it can be concluded that using a temperature ramp starting from a reasonable compromise temperature, which is neither too close to the ZnTe growth temperature nor to the GaSb growth temperature, will shield the GaSb/ZnTe interface from damage while bringing the temperature close enough to the normal GaSb growth temperature.

4.4 Summary

The MBE growth of high quality GaSb grown on ZnTe/GaSb (001) virtual substrates with a temperature ramp at the beginning of the GaSb growth has been demonstrated. High-resolution XRD results show clear Pendellösung thickness fringes from both GaSb and ZnTe epilayers, and simulations fit the experimental data very well. Cross-section TEM images show excellent crystallinity and smooth morphology for both ZnTe/GaSb and GaSb/ZnTe interfaces. No misfit dislocations or stacking faults were observed at the interfaces for Sample A, B

and C. Plan-view TEM images of Sample C revealed well-separated Lomer dislocation at the ZnTe/GaSb interface and threading dislocations in the top GaSb layer. The defect density was estimated to be ~1 x10^7/cm^2. The corresponding PL spectra indicated that the proposed GaSb transition layer grown on ZnTe using a temperature ramp improves the overall optical properties.

REFERENCES

[1]J. Fan, L. Ouyang, X. Liu, D. Ding, J. K. Furdyna, D. J. Smith and Y.-H. Zhang, J. Vac. Sci. Technol. B **30**, 02B122 (2012).

[2]Y.-H. Zhang, S.-N. Wu, D. Ding, S.-Q. Yu, and S. R. Johnson, Proceedings of the 33rd IEEE PVSC, p20 (2008).

[3]S. Wang, D. Ding, X. Liu, X.-B. Zhang, D. J. Smith, J. K. Furdyna, and Y.-H. Zhang, J. Cryst. Growth **311,** 2116 (2009).

[4]J. Fan, L. Ouyang, X. Liu, D. Ding, J. K. Furdyna, D. J. Smith, and Y.-H. Zhang, J. Cryst. Growth **323**, 127 (2011).

[5]L. Ouyang, J. Fan, S. Wang, X. Lu, Y.-H. Zhang, X. Liu, J. K. Furdyna, and D. J. Smith, J. Cryst. Growth **330**, 30 (2011).

[6]Y. Chen, G. Brill, D. Benson, P. Wijewarnasuriya, and N. Dhar, "MBE growth of ZnTe and HgCdSe on Si: a new IR material", Paper 8155A-36, SPIE Optics and Photonics, San Diego, CA, USA (2011).

[7]W. Lee, S. Kim, S. Choi, H. Lee, S. Lee, S. Park, T. Yao, J. Song, H. Ko, and J. Chang, J. Cryst. Growth **305**, 40 (2007).

[8]S. Kim, W. Lee, M. Jung, J. Chang, A. K. Nyi, H. Lee, J. Song, D. Oh, S. Park, and T. Yao, Appl. Surf. Sci **256**, 1261 (2009).

[9]C. Z. Wang, D. J. Smith, S. Tobin, T. Parodos, J. Zhao, Y. Chang, and S. Sivananthan, J. Vac. Sci. Technol. A **24**, 995 (2006).

[10]H. Leiderer, G. Jahn, M. Silberbauer, W. Kuhn, H. P. Wagner, W. Limmer, and W. Gebhardt, J. Appl. Phy. **70**, 398 (1991).

[11]C. Benoit a la Guillaume and P. Lavallard, Phys. Rev. B **5**, 4900 (1972).

[12]W. Jakowetz, W. Rühle, K. Breuninger, and M. Pilkuhn, Phys. Status Solidi (a) **12**, 169 (1972).

[13]W. Rühle, W. Jakowetz, C. Wölk, R. Linnebach, and M. Pilkuhn, Phys. Status Solidi (b) **73**, 255 (1976).

[14]M.-C. Wu and C.-C. Chen, J. Appl. Phys. **72,** 4275 (1992).

Chapter 5

STRUCTURAL CHARACTERIZATION OF $InAs/InAs_{1-x}Sb_x$ TYPE-II SUPERLATTICES

In this chapter, the structural characterization of strain-balanced $InAs/InAs_{1-x}Sb_x$ type-II superlattices (T2SLs) is described. This study was carried out in collaboration with Prof. Y.-H. Zhang and colleagues at Arizona State University. The $InAs/InAs_{1-x}Sb_x$ T2SLs grown by metalorganic chemical vapor deposition (MOCVD) were provided by Prof. R. D. Dupuis and colleagues at Georgia Institute of Technology; and $InAs/InAs_{1-x}Sb_x$ T2SLs grown by molecular beam epitaxy (MBE) were provided by Prof. Diana Huffaker and colleagues at University of California, Los Angeles. X-ray diffraction (XRD) measurements were performed by Elizabeth H. Steenbergen at Arizona State University. My contribution to this work has been the microstructural characterization using electron microscopy. Results from this study have been published elsewhere.[1,2]

5.1 Introduction

Type-II superlattices (SLs) have attracted much interest from the semiconductor industry since first being proposed.[3] Antimonide-based type-II SLs have been recognized as possible low-cost alternatives to the HgCdTe materials system for infrared (IR) applications, due to several key advantages including lower tunneling current,[4] greater flexibility in band-gap engineering,[5] and reduced Auger recombination.[6] Extensive investigations of InAs/(In)GaSb type-II SLs

have been carried out, including theoretical calculations of the band structure[4] and minority carrier lifetimes,[7] and significant success has been achieved for device performance in mid-, long- and very-long-wavelength infrared (VLWIR) ranges.[8-11] Strain-balanced InAs/$InAs_{1-x}Sb_x$ SLs have been proposed as another possible alternative to HgCdTe,[12] and have already shown great promise for mid-IR laser and photodetector structures,[13] with photoluminescence emission in the range of 5-10 μm being achieved for SL structures containing Sb concentrations of 14-27%.[14] The absence of gallium in these InAs/$InAs_{1-x}Sb_x$ SLs is expected to simplify the SL interfaces and hence the growth process,[15] and also result in longer carrier lifetimes,[16,17] as recently demonstrated.[18] So far, the growth of antimonide-based T2SL structure and devices have been dominated by MBE.[9,11,15,18] In comparison, the MOCVD technique has very high throughput and could enable lower cost, which is preferable for mass production. Thus, it is worth investigating despite it being more challenging to grow high quality InAs/$InAs_{1-x}Sb_x$ T2SLs by MOCVD.

In the growth of mixed As/Sb alloys by conventional solid-source MBE, the As_2 and Sb_2 beam flux ratio is normally used to control the average group-V composition of the epitaxial material. However, due to large differences in the incorporation coefficients of As_2 and Sb_2, accurate control of composition in the $InAs_{1-x}Sb_x$ alloys becomes challenging. Growth by modulated MBE involves control of As and Sb incorporation by rapidly alternating the As_2 and Sb_2 beam flux, using the timing of shutter operation to control the group-V composition.[19] This growth technique could possibly provide more precise control and

reproducibility of the group-V alloy composition in the $InAs_{1-x}Sb_x$ layers of $InAs/InAs_{1-x}Sb_x$ SLs. Improvements in composition control and crystalline quality of $AlAs_xSb_{1-x}$ and $In(Ga)As_xSb_{1-x}$ alloys grown by modulated MBE have been reported.[13,20-23] Further advantages of modulated MBE are that the technique could provide protection against composition drift and achieve more abrupt interfaces,[24] which are important factors to take into consideration since the transition wavelength and recombination efficiency are expected to be strongly influenced by the compositional abruptness at the interfaces.[25,26]

High quality $InAs/InAs_{1-x}Sb_x$ SLs require sharp and defect-free interfaces between the InAs and $InAs_{1-x}Sb_x$ layers. In this study, structural properties of strain-balanced $InAs/InAs_{1-x}Sb_x$ type-II SLs grown on GaSb (001) substrates by MOCVD and MBE were investigated. Transmission electron microscopy (TEM) was used to investigate the microstructure of $InAs/InAs_{1-x}Sb_x$ SLs with random $InAs_{1-x}Sb_x$ alloy layers grown by MOCVD and conventional MBE, and with ordered $InAs_{1-x}Sb_x$ alloy layers grown by modulated MBE. XRD was used to determine the average composition of the $InAs_{1-x}Sb_x$ alloy layers and the SL periods.

5.2 Experimental details

The MOCVD growth of the investigated $InAs/InAs_{1-x}Sb_x$ T2SLs was carried out carried out using a Thomas Swan MOCVD reactor system equipped with a close-coupled showerhead growth chamber at a pressure of 100 Torr. The epitaxial growth was typically initiated by depositing a 100-nm-thick GaSb buffer

layer at 600 ºC on 2-inch (001) *n*-type GaSb substrates.[15] The growth temperature was then ramped down to 500 ºC for all layers in the InAs/InAsSb T2SL structures, with a typical growth rate of ~0.1 nm/s. Figure 5.1 shows a schematic of the sample structures.

The MBE growth of the investigated InAs/$InAs_{1-x}Sb_x$ T2SLs was carried out in a solid-source MBE system, using modulated and conventional MBE growth techniques. All MBE grown samples nominally consisted of a 0.2-µm-thick GaSb buffer layer grown on an *n*-type GaSb (001) substrate at 500˚C, followed by deposition of 7-nm-thick $InAs_{1-x}Sb_x$ layers alternating with 18-nm-thick InAs layers for 20 periods, at a growth temperature of 435˚C. Finally, a 0.1-µm-thick GaSb capping layer was deposited at 480 ˚C. The modulated and conventional MBE growths are expected to yield ordered and random $InAs_{1-x}Sb_x$ alloy layers, respectively.

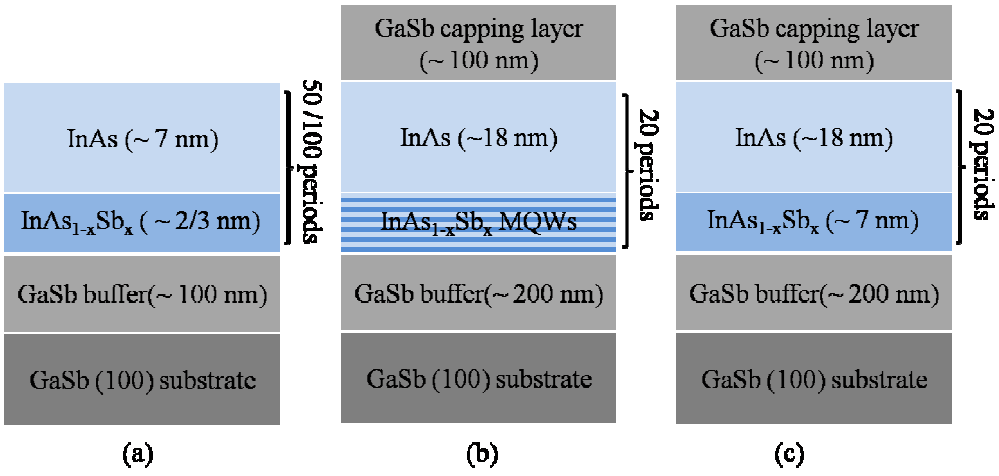

Fig. 5.1. Schematic illustration of the sample structures for: (a) MOCVD grown SLs; (b) modulated MBE grown SLs; and (c) conventional MBE grown SLs.

For the modulated MBE growth, the In shutter was kept open throughout the entire period of growth of the $InAs_{1-x}Sb_x$ layers, while the As and Sb shutters were alternately opened and closed for very short periods. The overall Sb composition would then be controlled by the Sb-shutter duty-cycle: $Sb_{shutter\text{-}time}/(As_{shutter\text{-}time} + Sb_{shutter\text{-}time})$. Each of these ordered $InAs_{1-x}Sb_x$ alloy layers consisted of six-period In(As)Sb/InAs(Sb) multiple quantum well (MQW) layers, as shown in Fig. 5.1(b).

The high-resolution XRD measurements were performed using a PANalytical X'pert Pro MRD. SL periods and the average Sb compositions of the $InAs_{1-x}Sb_x$ alloys were determined by comparing simulations to (004) high-resolution XRD measurements. Cross-sectional specimens were prepared for TEM observation using mechanical polishing and dimpling, followed by argon ion-milling. The mechanical polishing and dimpling typically reduced the sample thicknesses to 10~12 μm, and small holes in the films were then made by ion-milling at low energy (2.5~3 keV), using a liquid-nitrogen-temperature cooling stage to minimize any thermal or ion-beam damage.[27] The TEM characterization studies were mostly carried out using a JEM-4000EX high-resolution electron microscope operated at 400 keV, and JOEL 2010F electron microscope operated at 200 keV. All samples were prepared for observation along {110}-type zone-axis projections so that the direction of the electron beam would be aligned perpendicular to the growth surface normal.

Table 5.1. Summary of InAs/ $InAs_{1-x}Sb_x$ SL samples grown by MOCVD.

Sample	Number of periods	SL period (nm)		X_{Sb}	Calculated Eg at 0 K (meV)
		InAs	InAsSb		
A	100	7.0	3.3	22	224
B	50	7.0	2.3	23	250
C	50	7.0	2.0	37	171

5.3 Results and discussion

5.3.1 Characterization of MOCVD-grown samples

The InAs/$InAs_{1-x}Sb_x$ SLs samples grown by MOCVD are summarized in Table 5.1. The SL periods and the average Sb compositions, as determined by high-resolution XRD measurements, are also listed. The XRD patterns of Samples A and B are shown in Fig. 5.2, and the simulation results below each measurement closely agree with the experimental data. Sample A shows intense satellite peaks with narrow full-width-at-half-maximum (FWHMs) of less than 100 arcsec, indicating the high degree of crystallinity and uniform periodicity of this SL structure. The average relaxation of the SL was 74%, as determined from (224) ω-2θ coupled scans. The satellite peaks of Sample B are broader than those of Sample A, and the relaxation was determined to be ~83% from (224) ω-2θ coupled scans. The XRD patterns of Sample C exhibited 100% relaxation.

Cross-sectional electron micrographs of Sample A, as for example shown in Fig. 5.3, revealed excellent crystallinity and well-defined InAs/$InAs_{0.78}Sb_{0.22}$ SL structure. No defects were observed, which confirmed the very low density of

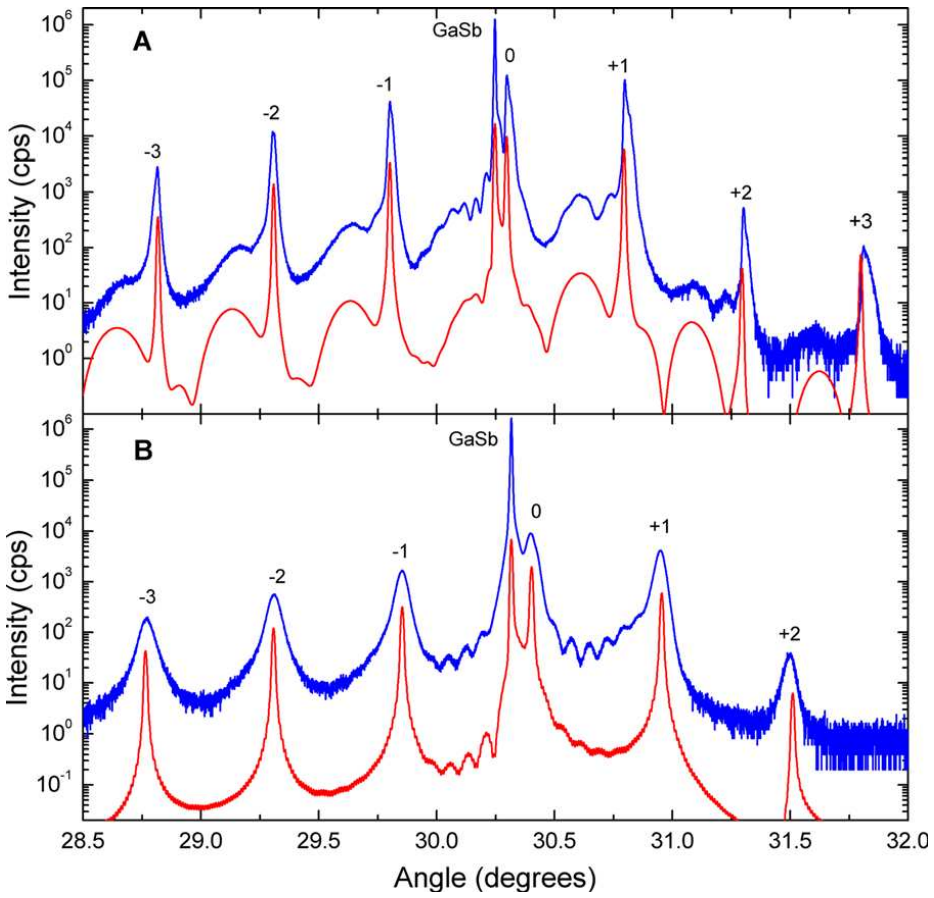

Fig. 5.2. High-resolution (004) XRD patterns and simulations (offset below each measurement) for Samples A and B.[2]

growth defects, in agreement with XRD results. Figure 5.4 shows the entire structures of Samples B and C, including 50 periods of InAs/InAsSb SL layers, GaSb buffer layer and GaSb (001) substrate. In contrast to Samples A, Sample B and C showed the presence of considerable growth defects, especially {111}-type stacking faults. These defects originate at either the substrate/buffer interface or the buffer/SL interface, and propagate well into the SL region. The broadening of the FWHM of the XRD satellite peaks of Samples B and C could presumably arise from these defects.

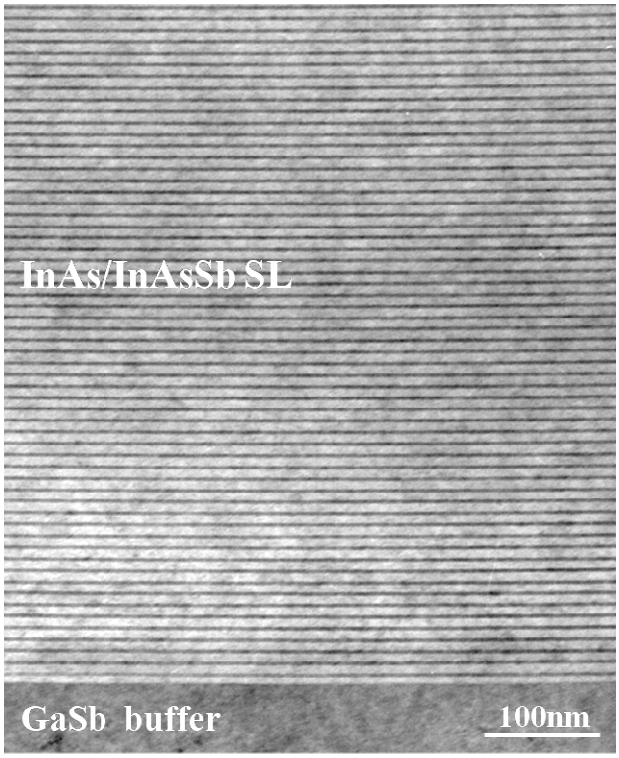

Fig. 5.3. Cross-sectional electron micrograph of Sample A demonstrating the excellent crystallinity of the In InAs/$InAs_{0.78}Sb_{0.22}$ SL.

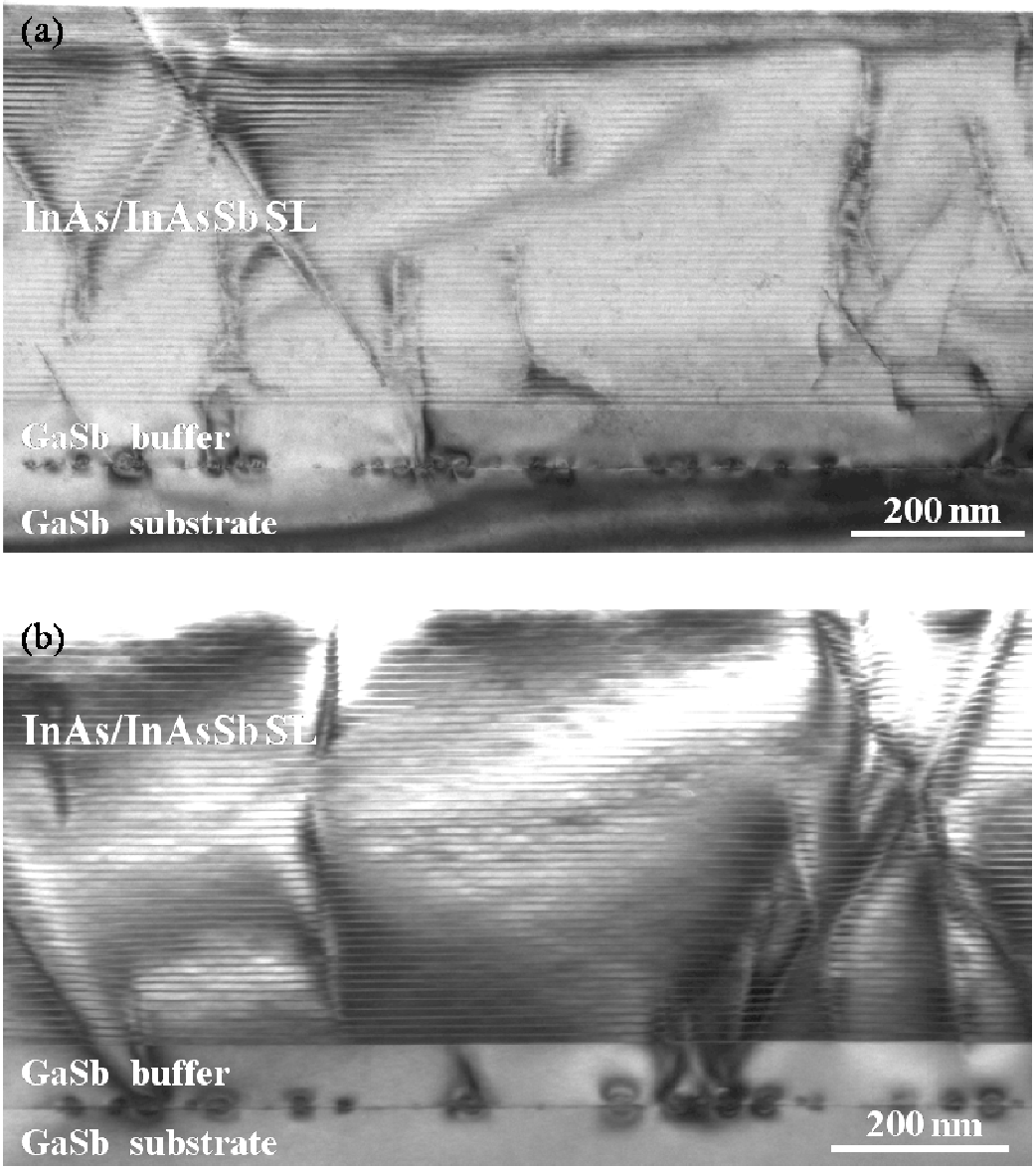

Fig. 5.4. Low magnification TEM images showing the whole InAs/InAsSb SL structure with a large density of defects for: (a) Sample B; and (b) Sample C.

5.3.2 Characterization of MBE grown samples

The InAs/$InAs_{1-x}Sb_x$ SLs samples grown by MBE, which include two ordered alloy SLs and two random alloy SLs, are summarized in Table 5.2. The SL periods and the average Sb compositions of the two random $InAs_{1-x}Sb_x$ alloy samples, as determined by high-resolution XRD measurements are also listed. The XRD patterns of Samples D and E are shown in Fig. 5.5, together with the corresponding simulations offset below each experimental profile. The most intense SL peak for Sample D no longer corresponds to the zero-order peak because of the large SL period. The XRD of the thick individual $InAs_{1-x}Sb_x$ and InAs layers show the envelope modulation of the SL peaks on either side of the substrate peak, causing some satellite peaks to be more intense than the zero-order SL peak. From the separation of the substrate peak from the zero-order SL peak, the average SL strain in the growth direction is determined to be 0.18% for Sample D. In comparison, Sample E has broader peaks than Sample D, suggesting the presence of increased defect density, which was later confirmed in the TEM microstructure studies.

Cross-sectional TEM images of Sample D, as for example shown in Fig. 5.6 (a), revealed excellent crystallinity and a very low density of growth defects, and indicated an SL periodicity of 245 Å, which was in close agreement with the results of the XRD simulation. Higher magnification images of the SL showed sharp interfaces between the individual $InAs_{1-x}Sb_x$ and InAs layers, and interfacial misfit dislocations were not observed. Moreover, the ordered-alloy structure, consisting of six-period In(As)Sb/InAs(Sb) MQW layers, is clearly visible and

Table 5.2. Summary of InAs/ $InAs_{1-x}Sb_x$ SL samples grown by MBE.

Sample	Growth technique	$T_{Sb\text{-}shutter}$ (second)	Sb shutter Duty-cycle	Flux Ratio Sb/(Sb+As)	SL period (nm)	X_{Sb}
D	Modulated	3	35%	-	24.5	-
E	Modulated	4	47%	-	24.1	-
F	Conventional	-	-	0.35	24.6	0.28
G	Conventional	-	-	0.37	24.6	0.29

well defined within each $InAs_{1-x}Sb_x$ layer, as shown in Fig. 5.6(b). High-angle annular dark-field (HAADF) scanning transmission electron microscopy (STEM) was also used to investigate the SL structures. Figure 5.7 displays Z-contrast images for Sample D. The InAsSb layers are brighter than InAs layers, as shown in Fig. 5.7 (a), since Sb has greater atomic mass than As. The six-period In(As)Sb/InAs(Sb) MQW structure within each InAsSb layer was confirmed, with the brighter layers corresponding to the In(As)Sb layers, as shown in Fig. 5.7 (b).

In the case of Sample E, which is another SL sample grown by modulated MBE when the growth conditions were not yet fully optimized, low magnification images revealed a more defective SL system. As shown in Fig. 5.8 (a), the substrate/buffer interface is clearly visible, and it is not flat, although this lack of flatness does not apparently cause any defects in the SL layers. However, the ordered-alloy structure was only well defined within the first $InAs_{1-x}Sb_x$ layer and progressively disappeared in the later $InAs_{1-x}Sb_x$ layers, as shown in Fig. 5.8 (b). Defective regions were visible within the SL structure that propagated upwards

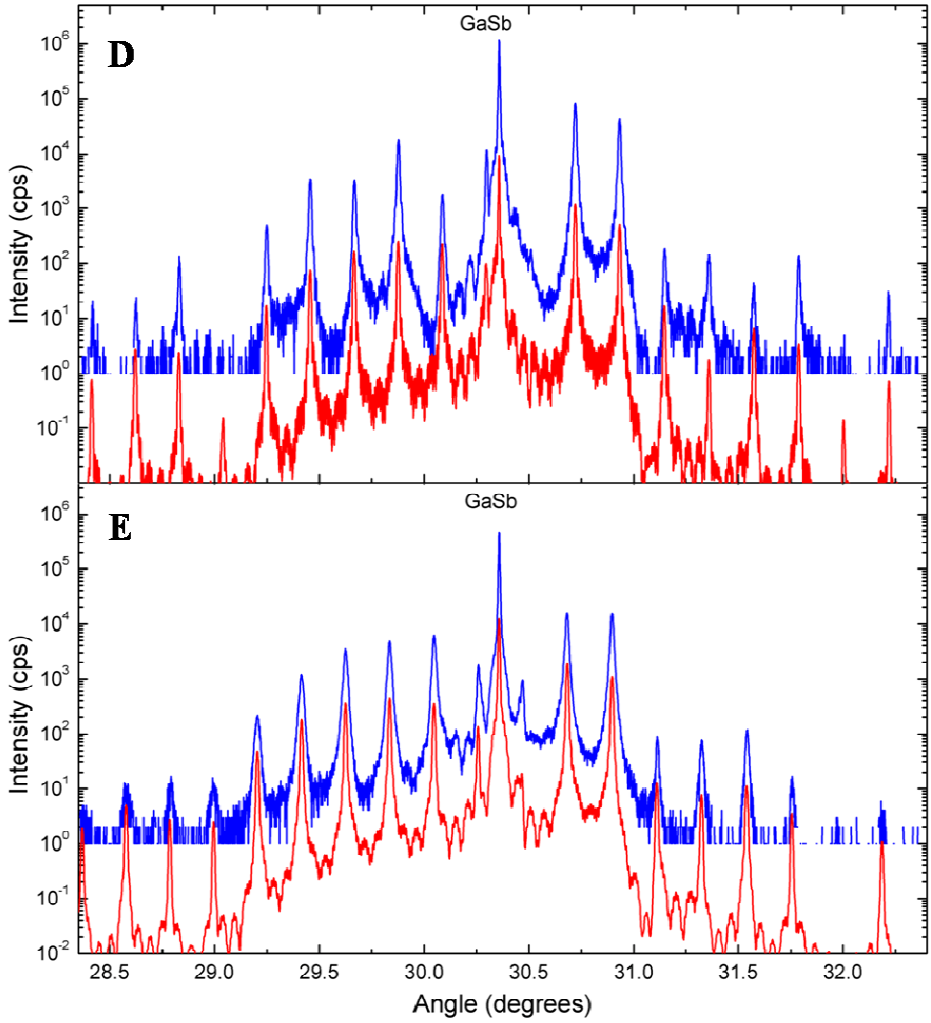

Fig. 5.5. High-resolution XRD (004) ω-2θ profiles and corresponding simulations (offset below each measurement) for Samples D and E.

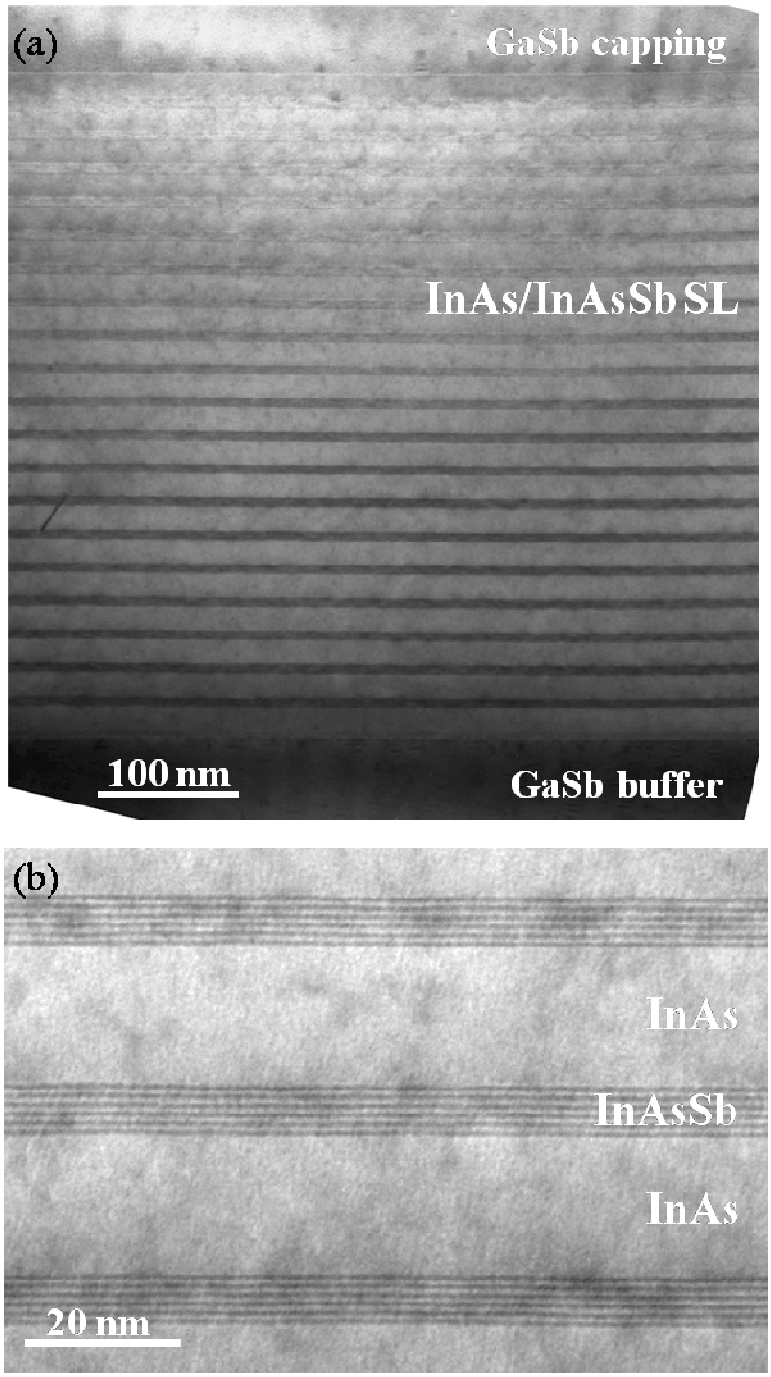

Fig. 5.6. (a) Cross-sectional electron micrograph showing entire SL structure of Sample D, confirming very low defect density; (b) Higher-magnification image clearly showing well-ordered In(As)Sb/InAs(Sb) MQW structure within the individual $InAs_{1-x}Sb_x$ layers of Sample D.

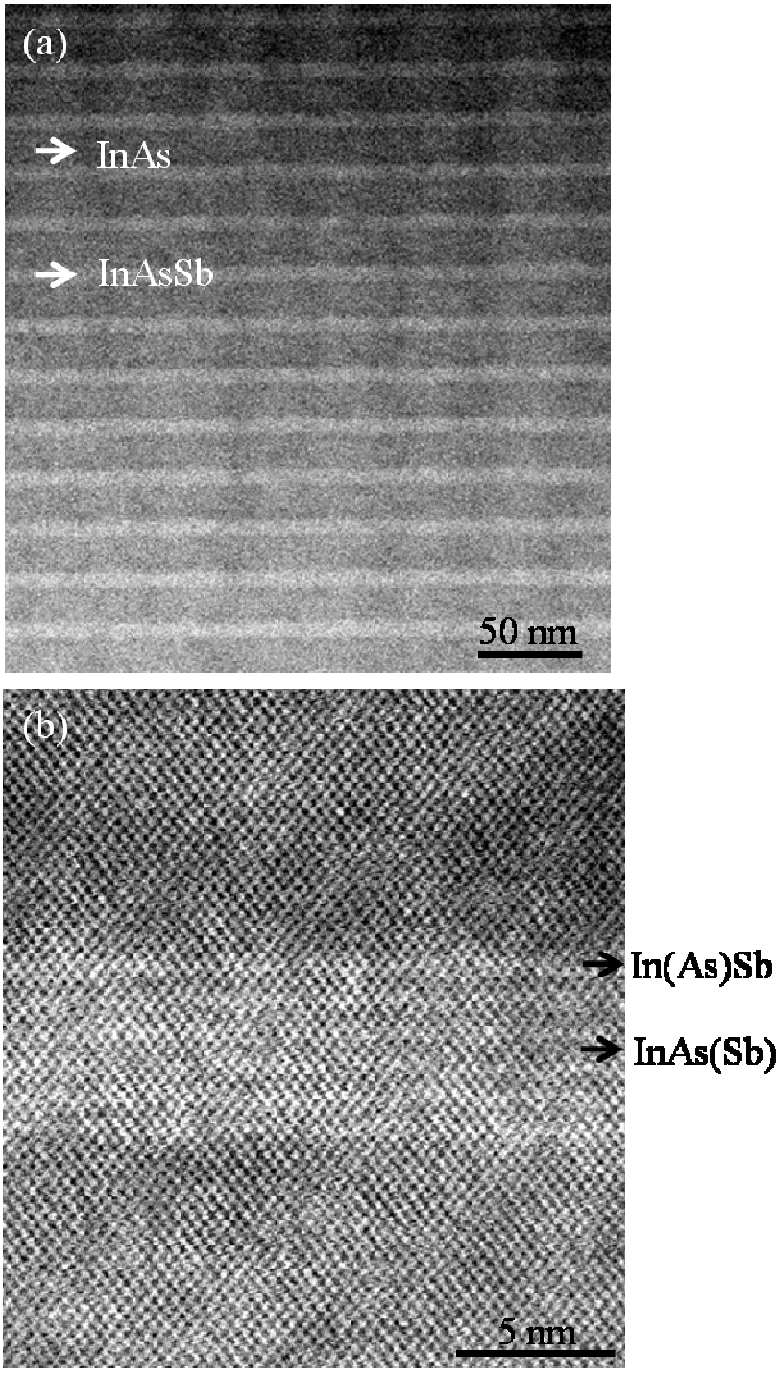

Fig. 5.7. Z-contrast images for Sample D acquired using HAADF-STEM.

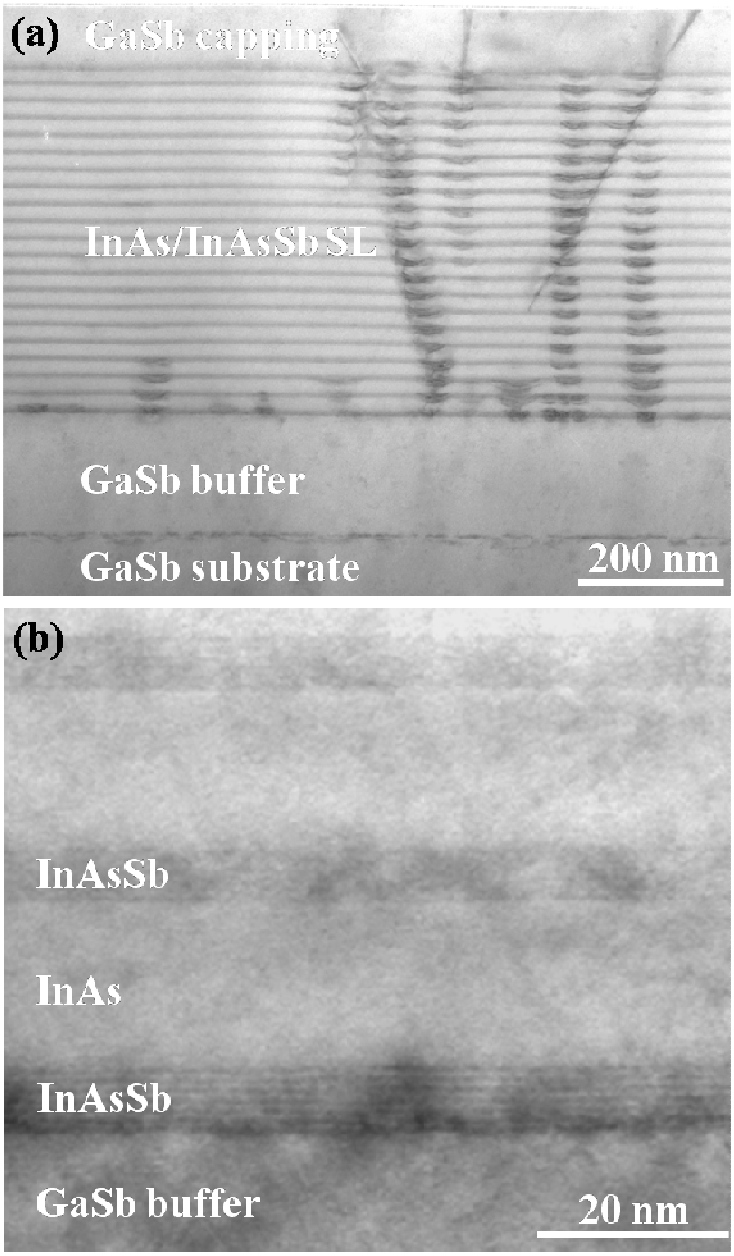

Fig. 5.8 (a) Low magnification TEM image of Sample E showing typical defective region; (b) Higher-magnification image showing the presence of the In(As)Sb/InAs(Sb) MQW structure apparently only within the first $InAs_{1-x}Sb_x$ layer.

similar to the behavior of self-aligned quantum dots in lattice-mismatched systems, but opposite to the conventional dome-like appearance. Most of these defects originated from the first SL layer, and are possibly due to the longer Sb shutter time used for this sample compared to Sample D. In addition, some extensive {111}-type stacking faults were observed propagating upwards through several SL periods to the top of the SL layer. The disappearance of the well-defined ordered-alloy structure within subsequent $InAs_{1-x}Sb_x$ layers is possibly due to intermixing of As and Sb atoms induced by the strain associated with the propagating defects.

Low magnification images of Sample F, which was a random alloy SL that was again not grown under fully optimized conditions, revealed the entire structure including the GaSb (001) substrate and buffer layer, 20-period SL layers, and the GaSb capping layer, as shown in Fig. 5.9. Growth defects, such as {111}-type stacking faults, are clearly visible. Most of these defects originated at the substrate/buffer interface, but some originated in the middle of the buffer layer, and many were present within the SL layers.

In the case of Sample G, cross-section electron micrographs typically showed no evidence of any defects across the entire field of view and demonstrated that excellent crystalline quality of the $InAs/InAs_{0.71}Sb_{0.29}$ SL could be achieved. The entire structure showing 20 well-defined SL periods is visible in Fig. 5.10. The substrate/buffer interface was again observed not to be flat, but no defects in the buffer layer have been caused by this lack of flatness. (It is worth noting here that such homoepitaxial interfaces are not always visible in the TEM

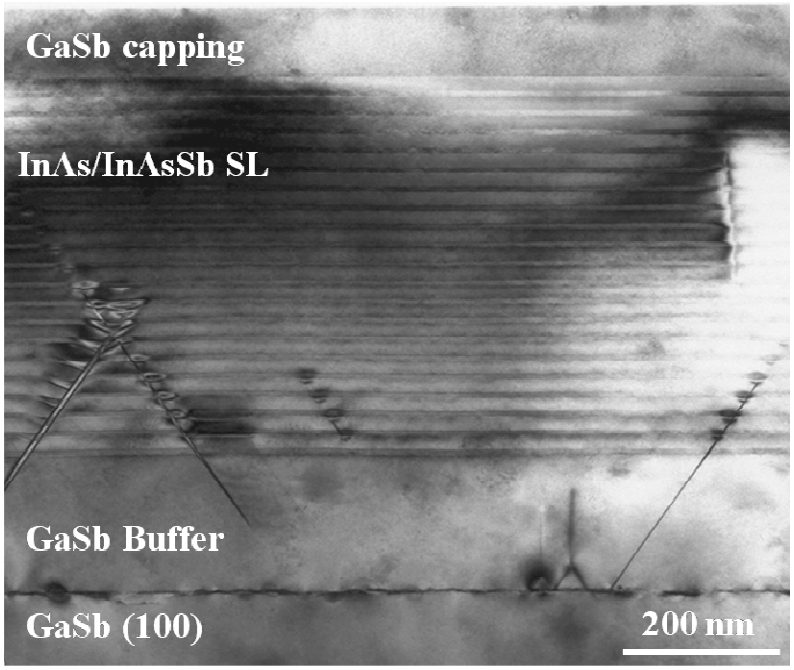

Fig. 5.9. Low magnification image of Sample F showing the entire structure.

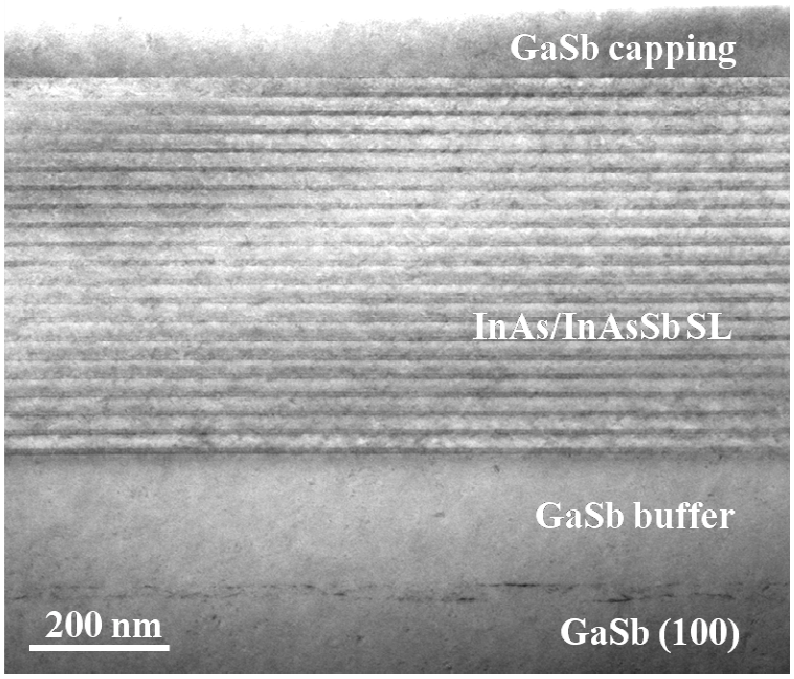

Fig. 5.10. Cross-sectional electron micrograph of Sample G demonstrating the well-defined and defect-free InAs/$InAs_{0.71}Sb_{0.29}$ SL region.

images of samples grown under optimal conditions when there is complete desorption of the surface oxide layer present on the GaSb substrate surface.) High-resolution lattice images of Sample G, such as Fig. 5.11 (a), clearly show the individual InAsSb and InAs layers. As confirmed by the Fourier-filtered image of the indicated area shown in Fig. 5.11 (b), it is also apparent that the interfaces of the $InAs_{0.71}Sb_{0.29}$ layers grown on InAs are more abrupt than those of InAs layers grown on $InAs_{0.71}Sb_{0.29}$. Figure 5.11 (c) is a line profile averaging across both InAs-on-InAsSb and InAsSb-on-InAs interfaces, as indicated by the blue dashed area boxed on Fig. 5.11 (b). It is clear that the intensity drops rapidly at the InAsSb-on-InAs interface, while the intensity increases much more slowly at the InAs-on-InAsSb interface. This interface asymmetry in the SL layers is most likely related to Sb segregation, whereby some unintentional Sb is initially incorporated into the InAs layers during growth, as reported previously.[20, 28]

5.4 Summary

The structural properties of strain-balanced InAs/$InAs_{1-x}Sb_x$ SLs grown on GaSb (001) substrates by MOCVD and MBE, have been studied using XRD and TEM. Excellent structural quality of the InAs/$InAs_{1-x}Sb_x$ SLs grown by MOCVD has been demonstrated by TEM. Well-defined ordered–alloy In(As)Sb/InAs(Sb) MQW layers within individual $InAs_{1-x}Sb_x$ layers, were observed for samples grown by modulated MBE. However, the ordering disappeared when defects propagating through the SL layers appeared during growth. For samples grown by conventional MBE, high-resolution images revealed that interfaces for $InAs_{1-x}Sb_x$

grown on InAs layers were sharper than for InAs grown on $InAs_{1-x}Sb_x$ layers, most likely due to some Sb surfactant segregation effect which warrants further investigation. Overall, the microstructural results are highly promising for the future growth of InAs/$InAs_{1-x}Sb_x$ SLs designed for operation at specific wavelengths.

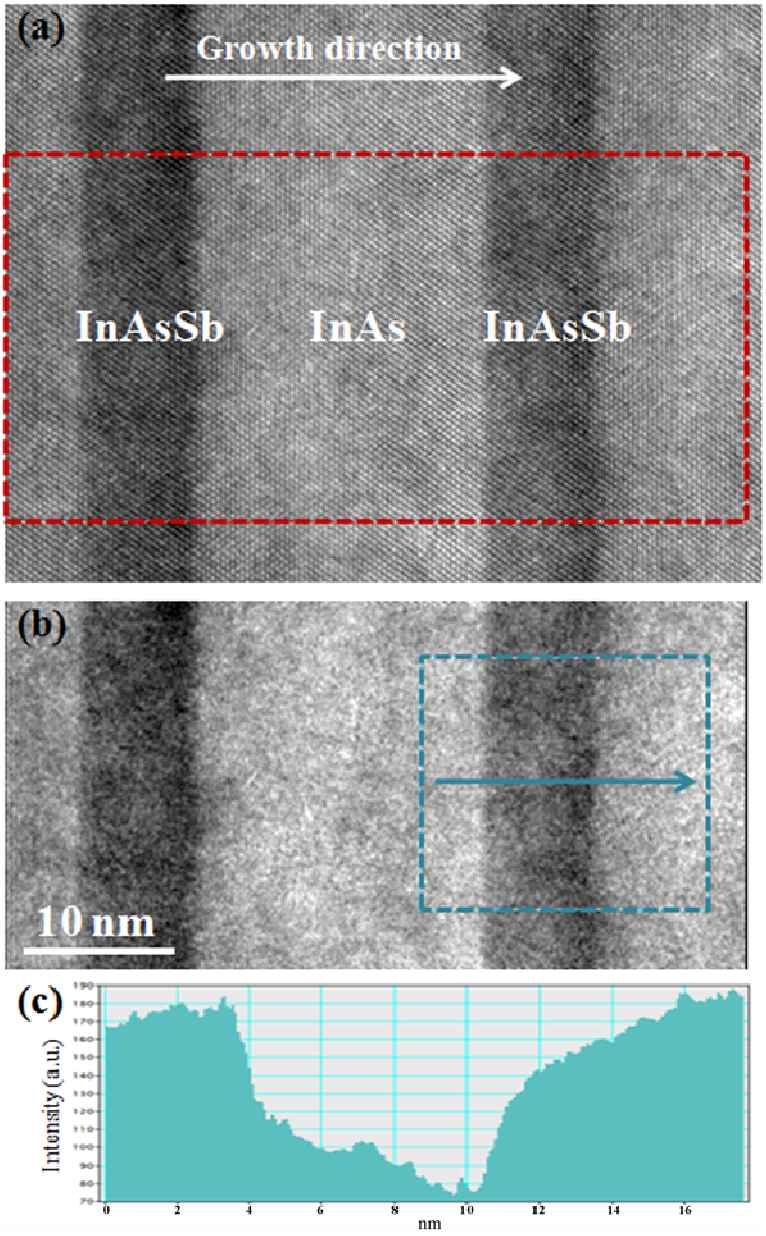

Fig. 5.11. (a) High-resolution lattice image showing individual InAs and $InAs_{0.71}Sb_{0.29}$ layers for sample G; (b) Filtered image revealing different interface abruptness between layers, which is attributed to segregation of the Sb surfactant during growth; (c) Line profile average across both InAs-on-InAsSb and InAsSb-on-InAs interfaces, as indicated by blue dashed area boxed above, showing the differences in interface abruptness.

REFERENCES

[1]L. Ouyang, E.H. Steenbergen, Y.-H. Zhang, K. Nunna, D.L. Huffaker and D. J. Smith, J. Vac. Sci. Technol. B **30**, 02B106 (2012).

[2]E.H. Steenbergen, Y. Huang, J.-H. Ryou, L.Ouyang, J.-J. Li, D.J. Smith, R.D. Dupuis and Y.-H. Zhang, Appl. Phys. Lett. 99, 091111 (2011).

[3]G. A. Sai-Halasz, R. Tsu, and L. Esaki, Appl. Phys. Lett. **30**, 651 (1977).

[4]D. L. Smith, T. C. McGill, and J. N. Schulman, Appl. Phys. Lett. **43**, 180 (1983).

[5]D. L. Smith, and C. Mailhiot, J. Appl. Phys. **62**, 2545 (1987).

[6]D. N. Talwar, and J. P. Loehr, Phys. Rev. B **49**, 10345 (1994).

[7]C. H. Grein, P. M. Young, and H. Ehrenreich, Appl. Phys. Lett. **61**, 2905 (1992).

[8]D. H. Chow, R. H. Miles, T. C. Hasenberg, A. R. Kost, Y.-H. Zhang, H. L. Dunlap, and L. West, Appl. Phys. Lett. **67**, 3700 (1995).

[9]J. L. Johnson, L. A. Samoska, A. C. Gossard, J. L. Merz, M. D. Jack, G. R. Chapman, B. A. Baumgratz, K. Kosai, and S. M. Johnson, J. Appl. Phys. **80**, 1116 (1996).

[10]H. Mohseni, M. Razeghi, G. J. Brown, and Y. S. Park, Appl. Phys. Lett. **78**, 2107 (2001).

[11]A. Hood, D. Hoffman, B.-M. Nguyen, P.-Y. Delaunay, E. Michel, and M. Razeghi, Appl. Phys. Lett. **89**, 093506 (2006).

[12]G. C. Osbourn, J. Vac. Sci. Technol. B **2**, 176 (1984).

[13]Y.-H. Zhang, Appl. Phys. Lett. **66**, 118 (1995).

[14]D. Lackner, O. J. Pitts, M. Steger, A. Yang, M. L. W. Thewalt, and S. P. Watkins, Appl. Phys. Lett. **95**, 081906 (2009).

[15]Y. Huang, J.-H. Ryou, R. D. Dupuis, V. R. D'Costa, E. H. Steenbergen, J. Fan, Y.-H. Zhang, A. Petschke, M. Mandl, and S.-L. Chuang, J. Cryst. Growth **314**, 92 (2011).

[16]W. Walukiewicz, Mater. Res. Soc. Symp. Proc. **148,** 137 (1989).

[17]C. H. Grein, M. E. Flatte, and H. Ehrenreich, Proc. Third Int. Symp. on LWIR Detectors and Arrays: Physics and Applications III, p. 211 (1995).

[18]E. H. Steenbergen, B. C. Connelly, G. D. Metcalfe, H. Shen, M. Wraback, D. Lubyshev, Y. Qiu, J. M. Fastenau, A. W. K. Liu, S. Elhamri, O. O. Cellek, and Y.-H. Zhang, Appl. Phys. Lett. **99**, 251110 (2011).

[19]Y.-H. Zhang, J. Cryst. Growth **150,** 838 (1995).

[20]Y.-H. Zhang, and D. H. Chow, Appl. Phys. Lett. **65**, 3239 (1994).

[21]A. Y. Lew, E. T. Yu, and Y.-H. Zhang, J. Vac. Sci. Technol. B **14**, 2940 (1996).

[22]Y.-H. Zhang, A. Lew, E. Yu, and Y. Chen, J. Cryst. Growth **175**, 833 (1997).

[23]E. Hall, H. Kroemer, and L. A. Coldren, J. Cryst. Growth **203**, 447 (1999).

[24]R. Kaspi, and G. P. Donati, J. Cryst. Growth **251**, 515 (2003).

[25]K. Muraki, S. Fukatsu, Y. Shiraki, and R. Ito, Appl. Phys. Lett. **61**, 557 (1992).

[26]P. M. Young, and H. Ehrenreich, Appl. Phys. Lett. **61**, 1069 (1992).

[27]C. Z. Wang, D. J. Smith, S. Tobin, T. Parodos, J. Zhao, Y. Chang, and S. Sivananthan, J. Vac. Sci. Technol. A **24**, 995 (2006).

[28]J. Steinshnider, J. Harper, M. Weimer, C.-H. Lin, S. S. Pei, and D. H. Chow, Phy. Rev. Lett. **85**, 4562 (2000).

Chapter 6

SUMMARY AND FUTURE WORK

6.1 Summary

The research described in this dissertation has involved microstructural characterization of II-VI and III-V compound semiconductor heterostructures and superlattices (SLs) using transmission electron microcopy (TEM).

The microstructure of thick ZnTe epilayers (~2.4 μm) grown by molecular beam epitaxy (MBE) under virtually identical conditions on GaSb, InAs, InP and GaAs (100) substrates was compared using TEM.[1] High-resolution electron micrographs revealed a highly coherent interface for the ZnTe/GaSb sample, and showed extensive areas with well-separated interfacial misfit dislocations for the ZnTe/InAs sample. Lomer edge dislocations with Burgers' vector of $a\langle 110\rangle$, as well as 60^{o} dislocations, were commonly observed at the interfaces of the ZnTe/InP and ZnTe/GaAs samples. Digital image processing was used to analyze the spatial distribution of misfit dislocations at the interfaces, and the amount of residual strain was estimated to be 0.01% for the ZnTe/InP sample and -0.09% for the ZnTe/GaAs sample. Strong PL spectra for all the ZnTe samples were observed from 80 to 300 K. The PL peak positions of the ZnTe epilayers were at 2.26 eV at room temperature.

The MBE growth of high quality GaSb grown on ZnTe/GaSb (001) virtual substrates with a temperature ramp at the beginning of the GaSb growth has been investigated.[2] High-resolution XRD results show clear Pendellösung thickness

fringes from both GaSb and ZnTe epilayers, and simulations fit the experimental data very well. Cross-section TEM images show excellent crystallinity and smooth morphology for both ZnTe/GaSb and GaSb/ZnTe interfaces. Plan-view TEM image revealed the presence of Lomer dislocations at the ZnTe/GaSb interface and threading dislocations in the top GaSb layer. The defect density was estimated to be ~1 $x10^7/cm^2$. The PL spectra show that using the proposed GaSb transition layer grown on ZnTe with a temperature ramp improved the overall optical properties.

The structural properties of strain-balanced InAs/$InAs_{1-x}Sb_x$ SLs grown on GaSb (001) substrates by MOCVD and MBE, have been studied using XRD and TEM.[3,4] Excellent structural quality of the InAs/$InAs_{1-x}Sb_x$ SLs grown by MOCVD has been demonstrated. Well-defined ordered–alloy structure, with six periods of In(As)Sb/InAs(Sb) multiple quantum well layers, within individual $InAs_{1-x}Sb_x$ layers, were observed for samples grown by modulated MBE. However, the ordering disappeared when defects propagating through the SL layers appeared during growth. For samples grown by conventional MBE, high-resolution images revealed that interfaces for $InAs_{1-x}Sb_x$ grown on InAs layers were sharper than for InAs grown on $InAs_{1-x}Sb_x$ layers, most likely due to some Sb surfactant segregation effect which warrants further investigation. Overall, the microstructural results seem highly promising for the future growth of InAs/$InAs_{1-x}Sb_x$ SLs designed for operation at specific wavelengths.

6.2 Future Work

6.2.1 Minimization of ion-milling damage

Ion-milling damage during TEM sample preparation has been a serious ongoing issue for TEM observations of II-VI and some III-V materials, such as CdTe, ZnTe, InAs and InSb. Structural damage induced by argon-ion milling was observed in many of the TEM images reported in this dissertation, even when the sample was milled at very low energy and held properly at liquid nitrogen temperature. A consistent and reliable chemical etching method needs to be developed to eliminate the damaged surface layers of the sample after ion milling, such as using methanol solutions of either dilute bromine or dilute iodine, and citric acid.[5,6]

6.2.2 Atomic arrangements around the core of dislocations

In chapter 3, the microstructure of ZnTe epilayers grown on various III-V substrates were studied using TEM. Lomer edge dislocations and 60^{o} dislocations were commonly observed at the interfaces of ZnTe grown on GaAs and InP substrates using high resolution electron microscopy. The atomic arrangements around the core of Lomer edge dislocations and 60^{o} dislocations are an interesting topic to study in the future. The ability of high-angle annular dark-field (HAADF) imaging, also called Z-contrast imaging, to provide information at the atomic scale has been greatly improved through the recent development of aberration-corrected scanning transmission electron microscopy (STEM) instruments.[7,8] The annular-bright-field (ABF) configuration, which takes advantage of the large

convergence angle of the incident beam, provides an approach to directly image light element columns.[9,10] Individual atoms of Ga, As, In, P, Zn and Te should be resolved from HAADF or ABF images acquired using aberration-corrected STEM. Hence, the atomic arrangements around the core of dislocations could be obtained.

6.2.3 Interfacial intermixing in InAs/InAsSb T2SLs

In chapter 5, the atomic-scale structural properties of InAs/$InAs_{1-x}Sb_x$ SLs have been investigated. The interface of $InAs_{1-x}Sb_x$ deposited on InAs was revealed to be sharper than the interface of InAs deposited on $InAs_{1-x}Sb_x$ using high-resolution electron microscopy. The asymmetry in interface roughness of the SL layers may have a direct impact on the electronic and optical properties of the InAs/InAsSb T2SL-based devices. Thus, a systematic study should be made of the interface roughness of samples with fixed thickness but different Sb composition, and samples with fixed Sb composition but changes in thickness.

To determine the composition profile across both InAsSb-on-InAs and InAs-on-InAsSb interfaces of the InAs/InAsSb T2SLs, TEM-based 002 dark-field (DF) imaging provides a reliable and straightforward method. This techinique relies on the contrast variation analysis of the two-beam DF image obtained with the diffraction vector **g**=002, which is highly sensitive to the chemical composition of semiconductors with zincblende structure.[11-13] The method has been demonstrated in the study of In segregation of InGaAs/GaAs quantum well structures,[8] and the determination of composition profile of InAs/GaSb SLs.[9] The

resolution of this technique of approximately 0.5 nm is limited by the size of the objective aperture used for cutting off electrons with larger scattering angles.

Atomic-resolution HAADF images acquired using STEM provides another method to study interface sharpness. With aberration-corrected STEM, individual atomic planes can be easily resolved. A recently developed image processing technique for HAADF images, called column-ratio mapping, uses the change in the ratio of group III and V column intensities in each dumbbell along <110> direction to study the local compositional variation across the interface.[14] This technique involves the conversion of a standard HAADF image into a map that displays the column ratio value, which is measured in the absence of the background signal, and thus makes it possible to observe the distribution of dumbbell shapes and hence the local compositional variation. The method has been demonstrated on the determination of interface width for the AlAs/GaAs material system, where the interface of AlAs-on-GaAs is found to be generally rougher than that of GaAs-on-AlAs, as shown in Fig. 6.1.[15]

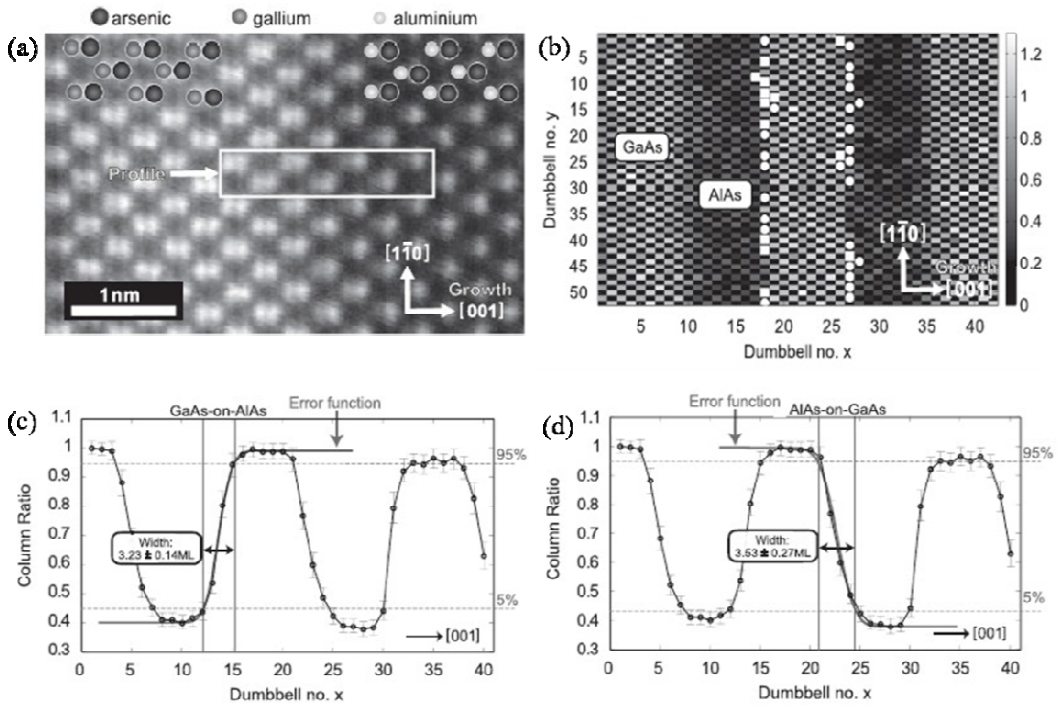

Fig. 6.1. (a) HAADF image of an isolated AlAs-on-GaAs interface at a specimen thickness of ~50 nm; (b) Example of a column ratio of the AlAs/GaAs SL at a specimen thickness of ~30 nm; (c)(d) Column ratio profiles averaged over the entire column ratio map in (b). The interface width was measured to be 3.23 ± 0.21 ML for GaAs grown on AlAs, and 3.53 ± 0.27 ML for AlAs grown on GaAs.[15]

REFERENCES

[1]L. Ouyang, J. Fan, S. Wang, X. Lu, Y.-H. Zhang, X. Liu, J. K. Furdyna, and D. J. Smith, J. Cryst. Growth **330**, 30 (2011).

[2]J. Fan, L. Ouyang, X. Liu, D. Ding, J. K. Furdyna, D. J. Smith and Y.-H. Zhang, J. Vac. Sci. Technol. B **30**, 02B122 (2012).

[3]L. Ouyang, E.H. Steenbergen, Y.-H. Zhang, K. Nunna, D.L. Huffaker and D. J. Smith, J. Vac. Sci. Technol. B **30**, 02B106 (2012).

[4]E.H. Steenbergen, Y. Huang, J.-H. Ryou, L.Ouyang, J.-J. Li, D.J. Smith, R.D. Dupuis and Y.-H. Zhang, Appl. Phys. Lett. **99**, 091111 (2011).

[5] V.G. Ivanits'Ka, P. Moravec, J. Franc, V. M. Tomashik, Z. F. Tomashik, K. Masek, P. S. Chukhnenko, P. Hoschi, and J. Ulrych, J. Electron. Mater. **36**, 8(2007).

[6]G. C. DeSalvo, R. Kaspi, and C. A. Bozada, J. Electrochem. Soc., **141**, 12 (1994).

[7]M. Haider, H. Rose, S. Uhlemann, E. Schwan, B. Kabius, and K. Urban, Ultramicroscopy **75**, 53 (1998).

[8]O. L. Krivanek, P. D. Nellist, N. Dellby, M. F. Murfitt, and Z. Szilagyi, Ultramicroscopy **96**, 229 (2003).

[9]E. Okunishi, I. Ishikawa, H. Sawada, F. Hosokawa, M. Hori, and Y. Kondo, Microsc. Microanal. **15**, 164 (2009).

[10]S. D. Findlay, S. Azuma, N. Shibata, E. Okunishi, and Y. Ikuhara, Ultramicroscopy **111**, 285 (2010).

[11]E. G. Bithell, and W. M. Stobbs, Phil. Mag. A **60**, 39 (1989).

[12]J. P. McCaffery, Z. R. Wasilewski, M. D. Robertson, and J. M. Corbett, Phil. Mag. A **75**, 803 (1997).

[13]E. Luna, B. Satpati, J. B. Rodriguez, A. N. Baranov, E. Tournie, and A. Trampert, Appl. Phys. Lett. **96**, 021904 (2010).

[14]P. D. Robb, and A. J. Craven, Ultramicroscopy **109**, 61 (2008).

[15]P. D. Robb, M. Finnie, Paolo Longo, and A. J. Craven, Ultramicroscopy **114**, 11 (2012).

APPENDIX A

REFERENCES

Zh. I. Alferov, *et al*, Inventor's Certificate No. 181737 (in Russian).

Zh. I. Alferov, *et al.*, Fiz. Tekn. Poluprovodn. 1, 1579 (1967).

Zh. I. Alferov, Semiconductors 32, 1 (1998).

J. Als-Nielsen, *et al.*, Elements of Modern X-ray Physics, John Wiley & Sons (2001).

R. L. Anderson, Solid-State Electron. 5, 341 (1962).

J. R. Arthur, J. Appl. Phys. 39, 4032 (1968).

J. R. Arthur, Surface Science 500, 189 (2002).

S. Bandara, *et al.*, Infrared Phys. Technol. 54, 263 (2011).

S. Bauer, *et al.*, J. Cryst. Growth 117, 297 (1992).

S. Bauer, *et al.*, Ultramicroscopy 51, 221 (1993).

E. Becquerel, Comptes Rendus 9, 561 (1839).

C. Benoit a la Guillaume, *et al.*, Phys. Rev. B 5, 4900 (1972).

E. G. Bithell, *et al.*, Phil. Mag. A 60, 39 (1989).

D. K. Bowen, *et al.*, High Resolution X-ray Diffractometry and Topography, Taylor & Francis (1998).

D. Chapin, *et al.*, J. Appl. Phys. 25, 676 (1954).

Y. Chen, *et al.*, SPIE Optics and Photonics, Paper 8155A-36 (2011)

A.Y. Cho, Surf. Sci. 17, 494 (1969).

D. H. Chow, *et al.*, Appl. Phys. Lett. 67, 3700 (1995).

A. V. Crewe, *et al.*, J. Mol. Biol. 48, 375 (1970).

B. D. Cullity, *et al.*, Elements of X-Ray Diffraction, 3rd Edition, Prentice Hall (1990).

P. D. Dapkus, Ann. Rev. Mater. Sci. 12, 243 (1982).

G. C. DeSalvo, *et al.*, Ultramicroscopy 75, 53 (1998).

R. D. Dupuis, *et al.*, Appl. Phys. Lett. 34, 335 (1979).

L. Esaki, *et al.*, IBM J. Res. Develop. 14, 61 (1970).

L. Esaki, IEEE J. Quantum Electron. 22, 1611 (1986).

J. Fan, *et al.*, J. Cryst. Growth 323, 127 (2011).

J. Fan, *et al.*, J. Vac. Sci. Technol. B 30, 02B122 (2012)

J. C. C. Fan, *et al.*, Proc. IEEE, Photovoltaic Specialists Conference, p692 (1982).

S. D. Findlay, *et al.*, Ultramicroscopy 111, 285 (2010).

F. C. Frank, *et al.*, Proc. Roy. Soc. A 189, 2005 (1949).

K. Fujiwara, Semiconductor Superlattices: Growth and Electronic Properties, Chapter 1, World Scientific (1995).

J. K. Furdyna, *et al.*, Superlattices and Microstructures 2, 89 (1986).

L. A. Giannuzzi, *et al.*, Micron 30, 197 (1999).

J. L. Gray, Handbook of Photovoltaic Science and Engineering, Chapter 3, John Wiley & Sons (2003).

C. H. Grein, *et al.*, in Proc. International Symposium on LWIR Detectors and Arrays: Physics and Applications III, p. 211 (1995).

C. H. Grein, *et al.*, Appl. Phys. Lett. 61, 2905 (1992).

A. I. Gubanov, Zh. Tekh. Fiz. 20, 1287 (1950).

A. I. Gubanov, Zh. Tekh. Fiz. 21, 304 (1951).

E. Hall, *et al.*, J. Cryst. Growth 203, 447 (1999).

P. Hartel, *et al.*, Ultramicroscopy 63, 93 (1996).

S. S. Hegedus, *et al* Handbook of Photovoltaic Science and Engineering, Chapter 1, John Wiley & Sons (2003).

A. Hood, *et al.*, Appl. Phys. Lett. 89, 093506 (2006).

Y. Huang, *et al.*, J. Cryst. Growth 314, 92 (2011).

V. G. Ivanits'Ka, *et al.*, J. Electron. Mater. 36, 8(2007).

W. Jakowetz, *et al.*, Phys. Status Solidi (a) 12, 169 (1972).

L. Jing, *et al.*, Solar Energy Materials & Solar Cells 90, 1773 (2006).

J. L. Johnson, *et al.*, J. Appl. Phys. 80, 1116 (1996).

S. Kamuro *et al.*, Solid State Electron 14, 1183(1971).

R. Kaspi, *et al.*, J. Cryst. Growth 251, 515 (2003).

B. J. Kim, *et al.*, J. Cryst. Growth 235, 201 (2002).

T. W. Kim, *et al.*, Appl. Phys. Lett. 78, 1409 (2001).

S. Kim, *et al.*, Appl. Surf. Sci 256, 1261 (2009).

R .R. King, *et al.*, Appl. Phys. Lett. 90, 183516 (2007).

C. Kittel, Introduction to Solid State Physics, John Wiley& Sons, Inc., New Jersey (2005).

O. L. Krivanek, *et al.*, Ultramicroscopy 96, 229 (2003).

H. Kroemer, Proc. IRE 45, 1535 (1957).

H. Kroemer, Proc. IEEE 51, 1782 (1963).

D. Lackner, *et al.*, Appl. Phys. Lett. 95, 081906 (2009).

W. Lee, *et al.*, J. Cryst. Growth 305, 40 (2007).

H. Leiderer, *et al.*, J. Appl. Phy. 70, 1 (1991).

A. Y. Lew, *et al.*, J. Vac. Sci. Technol. B 14, 2940 (1996).

Y. B. Li, *et al.*, Phys. Rev. B 55, 4589 (1997).

E. Luna, *et al.*, Appl. Phys. Lett. 96, 021904 (2010).

C. Mailhiot, Semiconductor Quantum Wells and Superlattices for Long-Wavelength Infrared Detectors, Charpt 4, Artech House (1993).

C . Maihiot, *et al.*, J. Vac. Sci. Technol. B 5, 1269 (1987).

M. O. Manasreh, *et al.*, Semiconductor Quantum Wells and Superlattices for Long-Wavelength Infrared Detectors, Charpt 1, Artech House(1993).

P. M. J. Maree, *et al.*, J. Appl. Phys. 62, 4413 (1987).

J. W. Matthews, J. Vac. Sci. Technol. 12, 126 (1975).

J. P. McCaffery, *et al.*, Phil. Mag. A 75, 803 (1997).

M. G. Mil'vidskii, Semiconductor Heterostructures, Chapter 5, MIR Publishers (1989).

A. G. Milnes, *et al.*, Heterojunctions and Metal-Semiconductor Junctions, Academic Press (1972).

H. Mohseni, *et al.*, Appl. Phys. Lett. 78, 2107 (2001).

K. Muraki, *et al.*, Appl. Phys. Lett. 61, 557 (1992).

D. A. Neamen, Semiconductor Physics and Devices: Basic Principles, 3rd edition, McGraw-Hill (2003).

P. D. Nellist, Scanning Transmission Electron Microscopy: Imaging and Analysis, Chapter 2, Springer (2011).

E. Okunishi, *et al.*, Microsc. Microanal. 15, 164 (2009).

J. M. Olson, *et al.*, Appl. Phys. Lett. 55, 1208 (1989).

E. P. O'Reilly, Semicond. Sci. Technol. 4, 121 (1989).

G. C. Osbourn, J. Vac. Sci. Technol. B 2, 176 (1984).

G. C. Osbourn, Semicond. Sci. Technol. 5, S5 (1990).

N. Otsuka, *et al.*, J. Vac. Sci. Technol. B 4, 896 (1986).

L. Ouyang, *et al.*, J. Cryst. Growth 330, 30 (2011).

L. Ouyang, *et al.*, J. Vac. Sci. Technol. B 30, 02B106 (2012).

L. Peraldo Bicelli, Surface Technology 26, 93 (1985).

F. Pierret, Semiconductor Device Fundamentals, Addison-Wesley (1996).

Y. Rajakarunanayake, *et al.,* Appl. Phys. Lett. 55, 1217 (1989).

P. D. Robb, *et al.,* Ultramicroscopy 109, 61 (2008).

P. D. Robb, *et al.*, Ultramicroscopy 114, 11 (2012).

W. Rühle, *et al.*, Phys. Status Solidi (b) 73, 255 (1976).

H. S. Rupprecht, *et al.,* Appl. Phys. Lett. 11, 81 (1967).

G. A. Sai-Halasz, *et al.,* Appl. Phys. Lett. 30, 651 (1977).

H. Sakaki, *et al.*, Solid State Commun. 26, 589 (1978).

A. F. Schwartzman, *et al.*, J. Electron. Mater. 20, 805 (1991).

W. Shockley, U.S. Patent 2,569,347 (1951).

D. L. Smith, *et al.*, Appl. Phys. Lett. 43, 180 (1983).

D. L. Smith, *et al.*, J. Appl. Phys. 62, 2545 (1987).

D. J. Smith, Rep. Prog. Phys. 60, 1513 (1997).

E.H. Steenbergen, *et al.*, Appl. Phys. Lett. 99, 071111 (2011).

E. H. Steenbergen, *et al.*, Appl. Phys. Lett. 99, 251110 (2011).

E. H. Steenbergen, *et al.*, J. Vac. Sci. Technol. B 30, 02B107 (2012).

J. Steinshnider, *et al.*, Phys. Rev. Lett. 85, 4562 (2000)

M. Strassburg, *et al.*, J. Cryst. Growth 248, 50 (2003).

S. M. Sze, *et al.*, Physics of Semiconductor devices, 3rd edition, John Wiley& Sons (2007).

D. N. Talwar, *et al.*, Phys. Rev. B 49, 10345 (1994).

I. Vurgaftman, *et al.*, Opt. Eng. 50, 061007 (2011).

W. Walukiewicz, Mat. Res. Soc. Symp. Proc.148, 137 (1989).

C. Z. Wang, *et al.*, J. Vac. Sci. Technol. A 24, 995 (2006).

S. Wang, *et al.*, J. Cryst. Growth 311, 2116 (2009).

B. E. Warren, X-Ray Diffraction, Dover Publications (1990).

D. B. Williams, *et al.*, Transmission Electron Microscopy, Springer (1996).

J. M. Woodball, *et al.*, Appl. Phys. Lett. 30, 492 (1977).

M.-C. Wu, *et al.*, J. Appl. Phys. 72, 4275 (1992).

P. M. Young, *et al.*, Appl. Phys. Lett. 61, 1069 (1992).

X. Zhang, *et al.*, J. Electron. Mater. 38, 1558 (2009).

Y.-H. Zhang, *et al.*, Appl. Phys. Lett. 65, 3239 (1994).

Y.-H. Zhang, J. Cryst. Growth 150, 838 (1995).

Y.-H. Zhang, Appl. Phys. Lett. 66, 118 (1995).

Y.-H. Zhang, *et al.*, J. Cryst. Growth 175, 833 (1997).

Y.-H. Zhang, *et al.*, Proceedings of the 33rd IEEE PVSC, p.20 (2008).

APPENDIX B

TABLE OF ACRONYMS

ABF	Annular-bright-field
CB	Conduction band
EELS	Electron-energy loss spectroscopy
EDX	Energy-dispersive X-ray spectroscopy
FFT	Fast Fourier transform
FIB	Focused ion beam
FWHM	Full width at half maximum
HAADF	High-angle annular-dark-field
HREM	High-resolution electron microscopy
HH	Heave-hole
LH	Light-hole
IR	Infrared
LW	Long-wavelength
MBE	Molecular beam epitaxy
MOCVD	Metalorganic chemical vapor deposition
PIPS	Precision ion polishing system
PL	Photoluminescence
RHEED	Reflection-high-energy electron diffraction
T2	Type-II
TEM	Transmission electron microscopy
SAED	Selected-area electron diffraction
SL	Superlattice

SRH	Shockley-Read-Hall
STEM	Scanning transmission electron microscopy
UHV	Ultrahigh-vacuum
VB	Valence band
XRD	X-ray diffraction